Targeting primary ciliogenesis in atypical teratoid/rhabdoid tumors

Inaugural-Dissertation

zur Erlangung des Doktorgrades
der Mathematisch-Naturwissenschaftlichen Fakultät
der Heinrich-Heine-Universität Düsseldorf

vorgelegt von

Lena Blümel
aus Greven

Düsseldorf, Mai 2020

aus der Klinik für Kinder-Onkologie, -Hämatologie und Klinische Immunologie des Universitätsklinikums Düsseldorf

Gedruckt mit der Genehmigung der
Mathematisch-Naturwissenschaftlichen Fakultät der
Heinrich-Heine-Universität Düsseldorf

Berichterstatter:

1. Prof. Dr. Guido Reifenberger

2. Prof. Dr. Thomas Kurz

Tag der mündlichen Prüfung: 18.09.2020

Table of contents

Summary

Atypical teratoid/rhabdoid tumor (AT/RT) is a rare but highly malignant brain tumor that preferentially develops in infants during the first years of life. Genetic hallmark of AT/RT is mutations in *SWI/SNF related matrix associated actin dependent regulator of chromatin subfamily b member 1 (SMARCB1)* or, less frequently, in *SMARCA4*. Prognosis for patients with AT/RT remains poor with median survival around 17 months, despite intensive multimodal therapies consisting of surgical resection, cranio-spinal radiation and high-dose chemotherapy. Recently, comprehensive genomic studies revealed three distinct molecular subgroups of AT/RT (AT/RT-TYR, AT/RT-MYC and AT/RT-SHH). Since primary cilia have already been shown to play a crucial role in the initiation and progression of other tumor entities, this thesis aimed to characterize the distribution of primary cilia across AT/RT subgroups and to target primary ciliogenesis in these tumors. Immunofluorescence was performed to detect primary cilia in AT/RT patient samples and cell lines. The functional role of primary cilia was investigated *in vitro* by knockdown of *kinesin family member 3A (KIF3A)* and treatment with Ciliobrevin D. The relevance of primary ciliogenesis in AT/RT biology was further elucidated *in vivo* using a *Drosophila* model of *SMARCB1* deficiency and an orthotopic xenograft mouse model of AT/RT. Primary cilia were detected in all AT/RT patient samples and cell lines investigated in this thesis. Notably, a significant subgroup-specific difference in the proportion of primary cilia-positive cells was observed. Specifically, AT/RT-TYR tumors demonstrated the highest percentage of ciliated cells, while AT/RT-MYC and AT/RT-SHH tumors showed a variable degree and the lowest proportion of cells with primary cilia, respectively. Knockdown of *KIF3A* and treatment with Ciliobrevin D significantly reduced proliferation and clonogenicity of AT/RT cells *in vitro*. Additionally, apoptosis was significantly increased via the upregulation of signal transducer and activator of transcription (STAT1) and death receptor 5 (DR5) signaling, as detected by proteogenomic profiling. In a *Drosophila* model of *SMARCB1* deficiency, concomitant knockdown of several cilia-associated genes resulted in a substantial shift of the lethal phenotype with >20% of flies reaching adulthood. Furthermore, a significantly prolonged survival was demonstrated in an orthotopic xenograft mouse model of AT/RT following *KIF3A* knockdown. Finally,

drug screening of a clinical compound library revealed increased vulnerability of AT/RT cells towards enhancer of zeste homolog 2 (EZH2) inhibition following *KIF3A* knockdown. In conclusion, the results summarized in this thesis implicate primary cilia as a key feature of AT/RT biology, especially of the AT/RT-TYR subgroup, and indicate potential clinical relevance of targeting ciliogenesis as a novel therapeutic approach for these highly malignant embryonal brain tumors.

Zusammenfassung

Der atypische teratoide/rhabdoide Tumor (AT/RT) ist der häufigste bösartige Hirntumor im Säuglingsalter. Aus genetischer Sicht sind AT/RTs durch Mutationen in *SMARCB1 (SWI/SNF related matrix associated actin dependent regulator of chromatin subfamily b member 1)* oder seltener in *SMARCA4* gekennzeichnet. Das mediane Überleben beträgt nur 17 Monate, obwohl diese jungen Patienten mit multimodalen Therapiestrategien bestehend aus chirurgischer Resektion, kraniospinaler Bestrahlung und Hochdosis-Chemotherapie behandelt werden. Erst kürzlich konnten mittels umfassender genomweiter Studien drei molekulare AT/RT Subgruppen (AT/RT-TYR, AT/RT-MYC und AT/RT-SHH) identifiziert werden. Da bereits gezeigt wurde, dass primäre Zilien eine zentrale Rolle bei der Entstehung und Progression von anderen Tumorentitäten spielen, zielte diese Studie darauf ab die Verteilung von primären Zilien zwischen den unterschiedlichen AT/RT Subgruppen zu charakterisieren und primäre Ziliogenese in diesen Tumoren anzugreifen. Es wurde ein Immunfluoreszenzprotokoll etabliert, welches die Detektion von primären Zilien in AT/RT Patientenproben und Zelllinien ermöglicht. Die funktionale Rolle der primären Zilien wurde *in vitro* durch die Herunterregulierung von *KIF3A (kinesin family member 3A)* und die Behandlung mit Ciliobrevin D untersucht. Die weitere Aufklärung der Bedeutung der primären Ziliogenese in der Biologie von AT/RT erfolgte *in vivo* mit Hilfe eines *Drosophila* Modells der *SMARCB1* Inaktivierung sowie eines orthotopen AT/RT Xenograft Mausmodells. In allen AT/RT Patientenproben und Zelllinien, die in dieser Studie untersucht wurden, konnten primäre Zilien nachgewiesen werden. Durch die Quantifizierung der ziliierten Zellen wurde ein signifikanter Subgruppen-spezifischer Unterschied deutlich, wobei AT/RT-TYR Tumoren im Vergleich zu den anderen Subgruppen den höchsten Anteil an ziliierten Zellen aufwiesen, während AT/RT-MYC und AT/RT-SHH Tumoren einen variablen Anteil und im Vergleich zu den anderen Subgruppen den niedrigsten Anteil an Zellen mit primären Zilien zeigten. Die Herunterregulierung von *KIF3A* und die Behandlung mit Ciliobrevin D führte in AT/RT Zellen zu einer signifikanten Verringerung der Proliferation und Klonogenizität. Zudem konnte durch proteogenomweite Analysen ein signifikant erhöhter Anteil an apoptotischen Zellen nachgewiesen werden, der durch

die Hochregulierung der STAT1 (*signal transducer and activator of transcription 1)* und DR5 (*death receptor 5*) Signaltransduktion induziert wurde. In einem *Drosophila* Modell der *SMARCB1* Inaktivierung führte die gleichzeitige Herunterregulierung von mehreren Zilien-assoziierten Genen zu einer erheblichen Verschiebung des tödlichen Phänotyps, wobei >20% der Fliegen das adulte Stadium erreichten. Darüber hinaus wurde in einem orthotopen AT/RT Xenograft Mausmodell eine signifikant verlängerte Überlebenszeit nach der Herunterregulierung von *KIF3A* nachgewiesen. Schließlich ergab das Wirkstoffscreening einer intern etablierten klinischen Wirkstoffbibliothek in AT/RT Zellen eine erhöhte Sensitivität gegenüber der Inhibierung von EZH2 (*enhancer of zeste homolog 2*) nach der Herunterregulierung von *KIF3A*. Zusammenfassend lässt sich sagen, dass die in dieser Studie erzielten Ergebnisse darauf schließen lassen, dass primäre Zilien eine essentielle Rolle in der Biologie von AT/RT (insbesondere von der AT/RT-TYR Subgruppe) spielen und demzufolge als möglicher Angriffspunkt für einen neuen Therapieansatz für diese bösartigen embryonalen Hirntumoren dienen können.

1 Introduction

1.1 Brain tumors

Many types of malignant cancers present an insidious threat to life. Amongst these, the uncontrolled growth of a malignant tumor inside the brain is one of the deadliest challenges that can encounter the human body[1]. The complexity of brain tumors is reflected by the wide spectrum of entities that is summarized in the current World Health Organization (WHO) Classification of Tumors of the Central Nervous System, which defines more than 100 distinct tumor types and subtypes of the central nervous system (CNS)[2]. These tumors are clinically and biologically highly diverse and comprise a broad spectrum from benign tumors that can often be cured by surgery alone to highly aggressive tumors that respond poorly to any available therapy[3]. For the past century, the classification of brain tumors has been based primarily on histological features detectable by light microscopy of tumor tissues stained by hematoxylin and eosin or some other special histological staining methods. With the advent of immunohistochemical methods, conventional histology was complemented by immunohistochemical expression analyses of lineage-associated markers and proliferation-associated proteins[2]. Today, however, also molecular parameters are incorporated into the classification of brain tumors, since targeted genetic analyses as well as high-throughput molecular profiling have shed light on the genetic basis of tumorigenesis, uncovering gene mutations, copy number aberrations, genomic rearrangements and deregulated transcriptomes specific to distinct brain tumor types[2,4]. In addition, microarray-based high-throughput analysis of DNA methylation patterns has been convincingly shown to be a highly robust and reproducible method to classify CNS tumors. In 2018, Capper and colleagues developed a comprehensive machine-learning approach that allows for a DNA methylation-based CNS tumor classification, thereby offering a histology-independent novel diagnostic approach to the WHO classification system for improved diagnostic categorization of tumors and facilitated therapeutic decision-making in clinical practice[3]. Brain tumors are graded from WHO grade I to IV, depending on their likelihood to behave, with WHO grade I

tumors growing slowly and demonstrating the lowest risk to recur after treatment and WHO grade IV tumors growing quickly and showing frequent resistance to therapy and rapid relapse[2].

Each year, about 500 children younger than 18 years of age are newly diagnosed with a brain tumor in Germany, according to the most recent data from the German Childhood Cancer Registry[5]. Although this incidence rate is rather low compared to other childhood cancers, brain tumors are the most common solid tumors in children and, in recent years, have also replaced leukemia as the leading cause of cancer-related death[6]. The most common type of pediatric brain tumor is pilocytic astrocytoma, followed by medulloblastoma. While pilocytic astrocytoma corresponds to WHO grade I and, thus, is typically associated with a favorable prognosis, medulloblastoma corresponds to WHO grad IV and, therefore, accounts for the most common malignant type of pediatric brain tumor, the prognosis of which is strongly dependent on the molecular tumor subgroup (wingless (WNT), sonic hedgehog (SHH), Group 3 and Group 4)[7,8]. WNT medulloblastoma, for instance, is associated with a favorable prognosis under current therapy, while Group 3 medulloblastoma, which is frequently characterized by overexpression or amplification of *MYC*, is often associated with a poor prognosis[8,9]. Another type of highly malignant brain tumor in children is atypical teratoid/rhabdoid tumor (AT/RT). Although this tumor is, in general, far less common compared to medulloblastoma, AT/RT is the most common malignant brain tumor arising in infants before the age of three years[10].

1.2 Atypical teratoid/rhabdoid tumor (AT/RT)

1.2.1 Incidence

The exact incidence of atypical teratoid/rhabdoid tumor (AT/RT) is difficult to determine, since this tumor entity has only been recognized first in 1996[11]. However, retrospective review disclosed that AT/RTs comprise approximately 1-2% of all pediatric brain tumors and account for up to 20% of brain tumors in patients younger than three

years of age[12]. Although AT/RT is typically a tumor of infancy and childhood, this tumor has also been described in adults, either arising as a primary tumor, as a secondary tumor from a low-grade tumor or after radiotherapy in childhood[13–18]. Overall, a slight male predominance has been reported, with a 1.3:1 male to female ratio[12]. In the majority of cases, AT/RTs occur among Caucasians (59.1%), followed by Hispanics (22.1%), African-Americans (9.9%) and Asian/Pacific Islanders (8.8%)[19].

1.2.2 Clinical presentation

According to the WHO classification of CNS tumors, AT/RTs correspond to WHO grade IV tumors[2]. The morphology of these tumors is diverse with primitive neuroectodermal, mesenchymal and epithelial features. Rhabdoid cells are considered as the hallmark of all rhabdoid tumors, including AT/RT, but are the predominant cell type only present in the minority of cases. Prior to the establishment and introduction of *SWI/SNF related matrix associated actin dependent regulator of chromatin subfamily b member 1 (SMARCB1)* mutation or deletion as a molecular marker, AT/RTs were frequently misdiagnosed when the characteristic rhabdoid cells were only sparsely present. This was due to their similarity to other embryonal brain tumors, specifically medulloblastoma and other rare types of embryonal CNS tumors[2,11,20]. AT/RTs can occur throughout the CNS, in infratentorial and supratentorial brain regions, but the most common primary site for AT/RTs is the cerebellum[21,22].

1.2.2.1 Symptoms and diagnostic evaluation

Since AT/RTs are fast-growing, patients typically have a fairly short history of progressive symptoms, measured over a period of days to weeks (National Cancer Institute, Childhood Central Nervous System Atypical Teratoid/Rhabdoid Tumor Treatment (PDQ®)-Health Professional Version). The symptoms and signs are variable and depend on the age of the patient as well as on the location and the size of the tumor. In infants, for instance, rather non-specific signs include lethargy, vomiting and failure to thrive.

More specific symptoms include head tilt and cranial nerve palsy, most commonly sixth and seventh nerve paresis. Headache and hemiplegia occur primarily in children older than three years of age[2].

For diagnostic evaluation, patients with suspected AT/RT receive magnetic resonance imaging (MRI) of the brain and the spine. They also receive lumbar puncture in order to inspect the cerebrospinal fluid (CSF) for signs of tumor cells (National Cancer Institute, Childhood Central Nervous System Atypical Teratoid/Rhabdoid Tumor Treatment (PDQ®)-Health Professional Version). Since AT/RT cannot be reliably distinguished from other brain tumors on the basis of clinical history or radiographic evaluation alone, also surgery is necessary to obtain tissue and confirm the diagnosis with genetic loss of *SMARCB1* or *SWI/SNF related matrix associated actin dependent regulator of chromatin subfamily a member 4 (SMARCA4)* and/or negative immunohistochemistry of their respective gene products SNF5/BAF47/INI1 or BRG1[23–25].

1.2.2.2 Treatment and prognosis

Overall, the prognosis for patients with AT/RT is poor with median survival around 17 months[10]. Since retrospective data often consider rather small and heterogeneously treated patients, much remains unknown about the prognostic role of specific patient features or treatments. In most of the cases, only age, tumor location and metastatic status at the time of diagnosis have been implicated. Age of three years or older, for instance, has been correlated with a better prognosis compared to age younger than three years, probably because irradiation therapy is avoided or deferred and incidence of metastasis is increased for the very young patients[26–28]. One of the major prognostic factors, though, is thought to be extent of surgery, with gross-total resection being correlated with improved outcome compared to subtotal resection, near total resection or partial resection[26].

Given the fact that AT/RTs are extremely rare, large-scale clinical trials are lacking and defining optimal treatment strategies has been challenging, so that a multimodal

approach consisting of maximal surgical resection, high-dose chemotherapy with autologous stem cell transplantation and cranio-spinal irradiation remains the current standard of care[10,12]. What kind of treatment a patient receives and how well a patient responds to treatment, however, is dependent on the age at the time of diagnosis, the size and extent of the tumor, the amount of mass that can be removed safely, as well as the presence or absence of metastatic disease.

Multiple therapeutic approaches have been attempted to increase survival for patients with AT/RT. Unfortunately, just limited success has been achieved so far. Instead, survival benefits remain debated due to contradictory findings that have been reported across studies. Although controversial study results have been disclosed, irradiation appears to be an important component of AT/RT therapy, especially when used as part of the initial therapy[29,30]. However, this approach is often avoided or deferred, especially for the treatment of very young patients, since irradiation is associated with severe neurocognitive toxicity[31]. Instead, these patients might benefit from intrathecal chemotherapy, consisting of either various combinations or single agents, including methotrexate, hydrocortisone and cytarabine, although the contribution of this approach to outcomes remains unclear[26]. There is no consensus on the most active chemotherapeutic agents for AT/RTs. While conventional chemotherapy has been shown to be largely non-effective, intensive alkylator-based chemotherapies, regimes with high-dose methotrexate and therapies that include high-dose chemotherapy with stem cell rescue have been shown to be more effective and may allow for reduced irradiation, at least for the treatment of older patients, without compromising survival[10,27].

Despite intensification of the therapeutic approaches, up to 50% of patients with AT/RT have early disease progression[32]. Thus, novel targets for therapeutic intervention are desperately needed. Given the fact that AT/RT typically carry few genetic alterations except for *SMARCB1* or *SMARCA4* mutation (see 1.2.3.1), it has been suggested that epigenetic changes contribute to disease progression, hence, targeting epigenetic regulatory mechanisms has been considered as an interesting therapy approach. Indeed, previous studies have reported an anti-proliferative effect for enhancer of zeste

homolog 2 (EZH2) inhibitors, bromo/bromo- and extra-terminal (BET) domain inhibitors and histone deacetylase (HDAC) inhibitors in *SMARCB1*-deficient tumors, leading to EZH2 inhibitor tazemetostat being currently under clinical evaluation[33–38]. Besides, cell cycle regulators have been suggested to present promising therapeutic targets. For instance, several studies have shown that cyclin D1 (CCND1) is essential for the growth of rhabdoid tumors, resulting in the clinical evaluation of the cyclin-dependent kinase 4/6 (CDK4/6) inhibitor ribociclib[39,40]. Genome-wide analyses have shown that also aurora kinase A (AURKA) has a role in the growth of rhabdoid tumors, leading to the clinical evaluation of the AURKA inhibitor alisertib[41,42]. Additionally, multi tyrosine kinase inhibitors are thought to be attractive targets for therapeutic intervention, including imatinib, sorafenib, sunitinib, nilotinib and dasatinib, however, these compounds are still under preclinical evaluation[38,43,44]. Other preclinical studies highlight growth and lineage specific pathways for AT/RT therapy. Specifically, roles for insulin-like growth factor (IGF), Notch and bone morphogenic protein (BMP) signaling pathways have been supported[38,45].

1.2.3 Genetics and molecular subgroups of AT/RT

1.2.3.1 Genetics of AT/RT

In principle, cancer is considered a genetic disease and numerous mutations are thought to be essential to drive tumor growth. Indeed, most cancer genomes have typically hundreds to thousands of point mutations and contain amplifications and deletions. However, not all cancers are necessarily that complex, since some highly aggressive cancers have been shown to be rather genetically stable cancers, including AT/RTs[46–49].

The only genetic abnormality observed in AT/RTs and, thus, the genetic hallmark of these tumors is inactivating mutation or loss of *SMARCB1* on chromosome 22 or, less frequently, of *SMARCA4* on chromosome 19[25,50,51]. SMARCB1 is a core component of the evolutionary conserved family of ATP-dependent SWI/SNF chromatin remodeling complexes, each composed of 9-12 protein subunits[52]. In addition to SMARCB1, there

are several core components that are present in most or even all complexes, including SWI/SNF related matrix associated actin dependent regulator of chromatin subfamily c member 1 (SMARCC1), SWI/SNF related matrix associated actin dependent regulator of chromatin subfamily c member 2 (SMARCC2) and one of the mutually exclusive ATPases SMARCA4 and SWI/SNF related matrix associated actin dependent regulator of chromatin subfamily c member 2 (SMARCA2) that use energy derived from ATP hydrolysis to mobilize nucleosomes. Additionally, there are lineage-restricted protein subunits that vary by cell type and are likely crucial to the specific function of the corresponding complex[53,54]. SWI/SNF complexes have been shown to have key roles in gene transcription. They regulate nucleosome positioning at promoters and, thus, regulate binding of transcription factors. They also regulate modification of enhancers that, in contrast to promoters, are not only accessible for transcription factors but also bind general factors, such as the mediator complex, the cohesion complex and various co-activators[54–57]. In addition, SWI/SNF complexes antagonize with polycomb repressive complex 2 (PRC2). PRC2 catalyzes trimethylation of histone 3 lysine 27 (H3K27me3) via EZH2 that leads to transcriptional repression of the affected target gene. SWI/SNF complexes oppose this repressive mark and favor an active H3K4me3 modified promoter[58]. As part of a rhabdoid predisposition syndrome (RTPS), *SMARCB1* (RTPS1, OMIM 609322) alterations, or less commonly, *SMARCA4* (RTPS2, OMIM 613325) alterations, are already present in the germline[59]. In case of RTPS1, such genetic alterations include point and frameshift mutations, intragenic deletions or duplications as well as larger deletions, including regions proximal and distal to *SMARCB1*. All these *SMARCB1* alterations can also arise sporadically[50,51]. In human malignancies, SWI/SNF complexes are the most commonly mutated chromatin remodelers. To date, it is estimated that approximately 20% of human cancers carry mutations in genes encoding subunits of SWI/SNF chromatin remodeling complexes[60].

1.2.3.2 Molecular subgroups of AT/RT

Despite sharing loss of SMARCB1 function (or loss of SMARCA4 function in the few *SMARCB1* wildtype cases) as the common tumorigenic event, AT/RTs have been shown to be a heterogeneous disease comprising three molecular subgroups, termed AT/RT-TYR, AT/RT-SHH and AT/RT-MYC (Figure 1). This scientific breakthrough has been achieved independently by two research groups conducting comprehensive analyses of DNA methylation and gene expression profiles of large tumor cohorts[38,61].

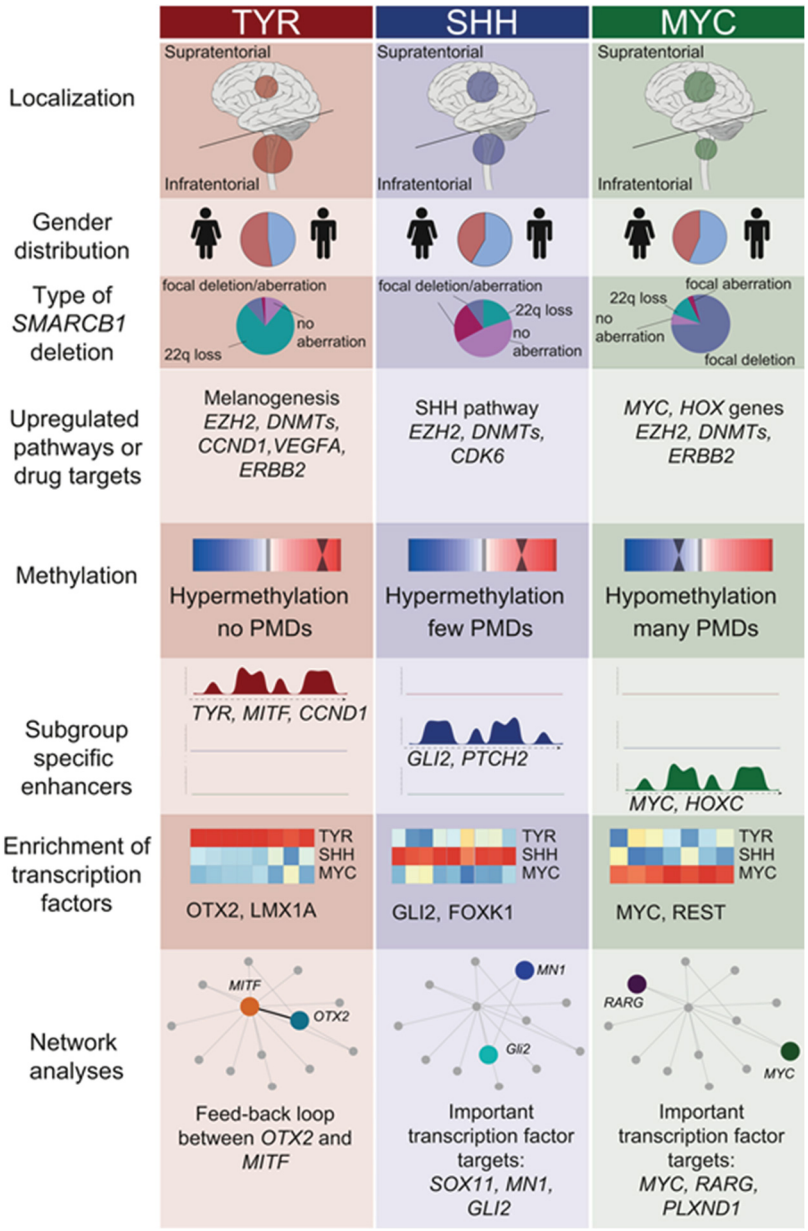

Figure 1: Overview of the three molecular subgroups of AT/RT with their different demographic and (epi-)genetic characteristics. Adapted from Johann and Erkek et al.[61].

The TYR subgroup of AT/RT is termed after the gene *TYR* (encoding the enzyme tyrosinase) that along with some other melanosomal markers, including *melanocyte inducing transcription factor (MITF)* and *dopachrome tautomerase (DCT)*, is highly expressed in almost every case in this subgroup. In addition, many genes involved in ciliogenesis are overexpressed. The AT/RT-SHH subgroup is characterized by aberrantly active SHH signaling, explaining its designation. Another characteristic of this subgroup is aberrantly active Notch signaling. The MYC subgroup of AT/RT, apparently, is named after the gene *MYC* that is highly expressed in this subgroup, just as *homeobox transcript antisense RNA (HOTAIR)* and many other HOX cluster genes. Potential subgroup-specific drug targets include vascular endothelial growth factor A (VEGFA) for AT/RT-TYR tumors, CDK6 for AT/RT-SHH tumors and epidermal growth factor receptor 2 (ERBB2) for AT/RT-TYR and AT/RT-MYC tumors, while drug targets for all AT/RTs include PRC2/EZH2, AURKA and HDAC1/2[61].

The AT/RT subgroups show different preferential locations in the brain, suggesting different cells of origin. While AT/RT-TYR tumors mostly occur in the infratentorial compartment, AT/RT-MYC tumors are more common in supratentorial regions. AT/RT-SHH tumors, though, present both infratentorially and supratentorially. In addition, age at diagnosis is also different between the subgroups. While AT/RT-TYR tumors are prominently present in very young children (age 0-1), patients with AT/RT-MYC tumors tend to be older and most of the AT/RT-SHH tumors present before the age of four. Gender distribution, however, does not show any significant differences between the subgroups[61].

Whole-genome sequencing (WGS) also revealed different types of inactivating *SMARCB1* mutations between the subgroups. Tumors of the TYR group, for instance, mainly harbored large deletions on chromosome 22q, affecting *SMARCB1* and surrounding genes. These large deletions were far less common in the two other subgroups. Instead, tumors of the SHH and the MYC subgroup rather showed no chromosome 22 copy aberrations, particularly in tumors of the SHH subgroup, focal gains or focal deletions, particularly in tumors of the MYC subgroup[61].

At the epigenetic level, whole-genome bisulfite sequencing (WGBS) demonstrated genome-wide hypermethylation for TYR and SHH tumors, with the highest differences in methylation in promoter regions, while methylation levels of MYC tumors were more comparable to normal cerebellum and other pediatric brain tumor entities. In part, this can be explained by the distribution of partially methylated domains (PMDs, domains of disordered methylation) between the subgroups, being almost completely absent in AT/RT-TYR tumors, variably distributed in AT/RT-SHH tumors and most prevalent in AT/RT-MYC tumors[61].

Genome-wide ChIP-seq data for H3-K27A and bromodomain-containing protein 4 (BRD4), a chromatin reader and a transcriptional co-activator, both required for enhancer activity, finally revealed that the transcriptional diversity between the subgroups is caused by active (super)enhancers that are specific for each subgroup[61]. Targets of differential enhancers include several AT/RT subgroup-specific signature genes like *TYR*, *MITF*, *GLIS family zinc finger 3 (GLIS3)*, *insulin-like growth factor binding protein 7 (IGFBP7)*, *CCND1* and *orthodenticle homeobox 2 (OTX2)* for the TYR subgroup, *glioma-associated oncogene 2 (GLI2)*, *BOC*, *NOTCH1*, *midnolin (MIDN)* and *forkhead box k1 (FOXK1)* for the SHH subgroup and *high mobility group at-hook 2 (HMGA2)* and *HOXC9* for the MYC subgroup. Additionally, specific transcription factors whose binding motifs are significantly enriched in subgroup-specific enhancers of the respective subgroup have been identified (*OTX2* and *LIM homeobox transcription factor 1 alpha (LMX1A)* for AT/RT-TYR tumors, *GLI2* for AT/RT-SHH tumors and *CCAAT enhancer binding protein beta (CEBPB)*, *retinoic acid receptor gamma (RARG)* and *MYC* for AT/RT-MYC tumors)[61].

1.3 Motile and non-motile (primary) cilia

1.3.1 Structure and function

First described in 1675 by Antony van Leeuwenhoek as incredibly thin little feet, or little legs, that move nimbly, cilia are the oldest known cellular organelles[62]. The term cilium (from Latin, meaning eyelash), though, was introduced only 100 years later by Otho

Fridericus Müller[63]. Originally, cilia were defined by their motility, existing solitary or multiple on a single eukaryotic cell, and for many decades this was their only assigned function. During the latter half of the 19th century, however, another type of solitary cilium was observed that was non-motile. Today, motility is still used as the criterium to distinguish between the two types of cilia, motile and non-motile (primary) cilia[64].

In general, the cilium is composed of a microtubule-based core structure, the axoneme, that is formed from a centriolar anchor, known as the basal body (Figure 2)[64].

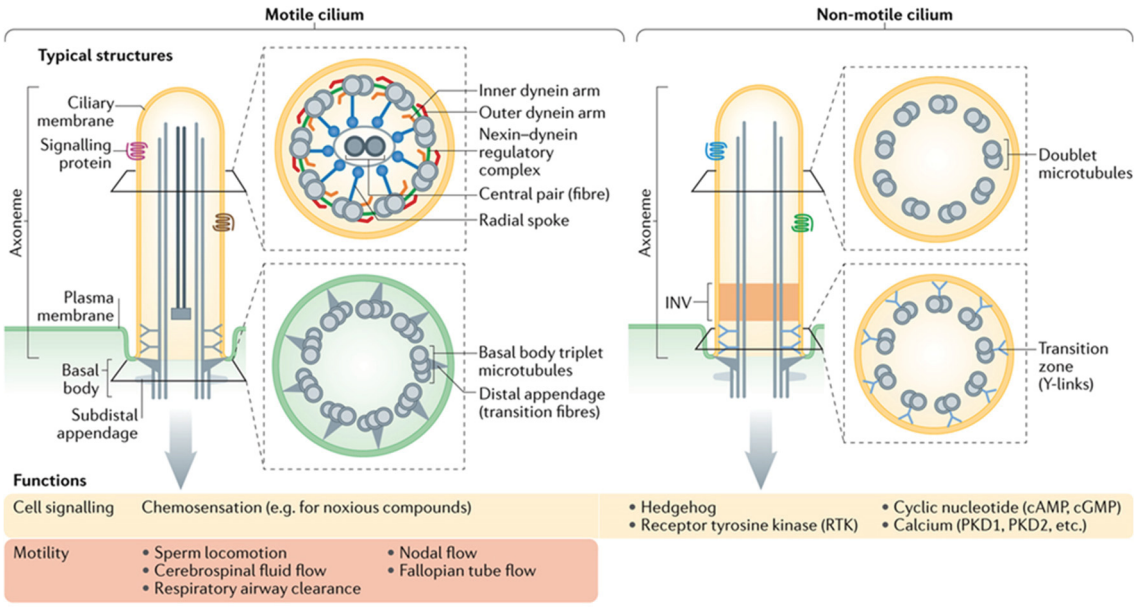

Figure 2: Structure and function of motile and non-motile (primary) cilia. Both motile and non-motile cilia extend from a centriolar anchor, the basal body, and are composed of a microtubule-based core structure, the axoneme. The basal body consists of triplet microtubules and subdistal and distal appendages (also known as transition fibres) that tether the basal body to the base of the ciliary membrane. The axoneme is composed of doublet microtubules. Basal body and axoneme are linked via the transition zone that features Y-shaped structures. Additional structures only found in motile cilia include a central pair of microtubules, axonemal dyneins, nexin links and radial spokes that are required for ciliary motility. Summarized are also key functions in cell signalling and motility. Adapted from Reiter and Leroux[64].

The axoneme consists of nine peripheral microtubule doublets, each doublet composing one complete microtubule (the A tubule) and one incomplete microtubule (the B tubule), and is surrounded by the ciliary membrane that is continuous with the plasma membrane. Additional structures only found in motile cilia include a central pair of microtubules, axonemal dyneins, consisting of inner and outer dynein arms, nexin links

and radial spokes that are required for ciliary motility. The basal body comprises nine microtubule triplets and transition fibers composed of subdistal appendages and strut-like structures that connect the basal body to the base of the ciliary membrane. The axoneme and the basal body are linked via the transition zone that features Y-shaped structures and is thought to act as a diffusion barrier, regulating entry and exit of ciliary proteins into and out of the cilium, thus, regulating ciliogenesis[65–67].

Formation and resorption of cilia are strictly organized multi-step processes that are synchronized to the cell cycle, with the formation of cilia starting at the G0G1 phase of the cell cycle[68]. First, the mother centriole converts to the basal body and attaches to the plasma membrane through its transition fibers that transform from centriolar appendages and are critical for positioning and orientation of the basal body. Next, the transition zone forms that resides distal to the basal body and functions as a gate controlling the transfer of ciliary proteins into and out of the cilium. Finally, construction and maintenance of the axoneme is enabled by the intraflagellar transport (IFT) machinery that is responsible for the bidirectional transport of multiprotein complexes along the axoneme. Ciliary resorption subsequently begins upon cell cycle re-entry and ends with the release of the basal body, thus, with the release of centrioles that later on function as microtubule-organizing centers or spindle poles during mitosis[65,69,70].

Depending on the direction of movement, ciliary proteins are transported along the axoneme by two different types of IFT motors. Movement of cargo to the ciliary tip (anterograde IFT), for instance, is catalyzed by kinesin-2, while return of cargo to the cell body (retrograde IFT) is catalyzed by cytoplasmic dynein 2[71–73]. Besides IFT motors, IFT relies on IFT proteins that form IFT complexes that transport the ciliary cargo. Two different types of IFT complexes have been identified. While IFT complex B contributes to the anterograde IFT of cargo and is necessary for the construction and maintenance of the primary cilium, IFT complex A is required for the retrograde IFT and, thus, is responsible for the return of cargo to the cell body[74–76].

1.4 Primary cilia in health and disease

The major function of primary cilia is cell signaling, leading to their designation as the cell's antenna[66]. Indeed, signaling through the primary cilium coordinates key processes during development and tissue homeostasis[77,78]. In the brain, for instance, primary cilia play essential roles at various stages of neurogenesis, from early patterning, through the proliferation and differentiation of neural stem and progenitor cells, to the maturation of neurons[79]. Although primary cilia are present on almost every cell in the human body, they have been regarded as rudimentary organelles for decades, and understanding their function has only recently begun through the identification of a group of rather rare genetic diseases, collectively known as ciliopathies[80]. The number of reported ciliopathies is increasing, as is the number of established and candidate ciliopathy-associated genes. One of the most interesting aspects of ciliopathies, though, is the diversity of organ involvement and clinical symptoms, spanning a wide spectrum of severity from relatively mild to lethal, that can even present from different mutations in the same gene[64].

Some ciliopathies, including polycystic kidney disease, are largely confined to the kidneys, liver and pancreas, possibly due to tissue-specific expression of the mutated gene products that localize to the primary cilium[81]. Other ciliopathies, in contrast, including Bardet-Biedl syndrome, Meckel-Gruber syndrome and Joubert syndrome are caused by compromised protein function in multiple tissues, leading to complex multi-organ developmental phenotypes, including cystic kidneys, CNS developmental defects and polydactyly[82–84].

Collectively, these findings highlight the importance of primary cilia for the development and homeostasis of a broad range of tissues.

1.5 Primary cilia in cancer

By now, primary cilia are known to be crucial regulators of cell signaling, so that it is not surprising that a dysfunction of primary cilia is frequently associated with pathologies[85].

Originally, primary cilia were found to be involved in a variety of diseases, commonly referred to as ciliopathies, but growing evidence suggests that primary cilia also play a pivotal role in different types of cancers, including brain cancers, skin cancers and epithelial cancers, whereat the way how primary cilia regulate tumorigenesis seems to differ between tumor types and within tumor subtypes[86].

The best-studied pathway linked to cilia, though, is the SHH pathway that plays an important role in developmental processes, including the establishment of the left-right body axis and the regulation of neural tube closure and patterning, and is also involved in cellular processes, including differentiation, proliferation and survival (Figure 3)[87].

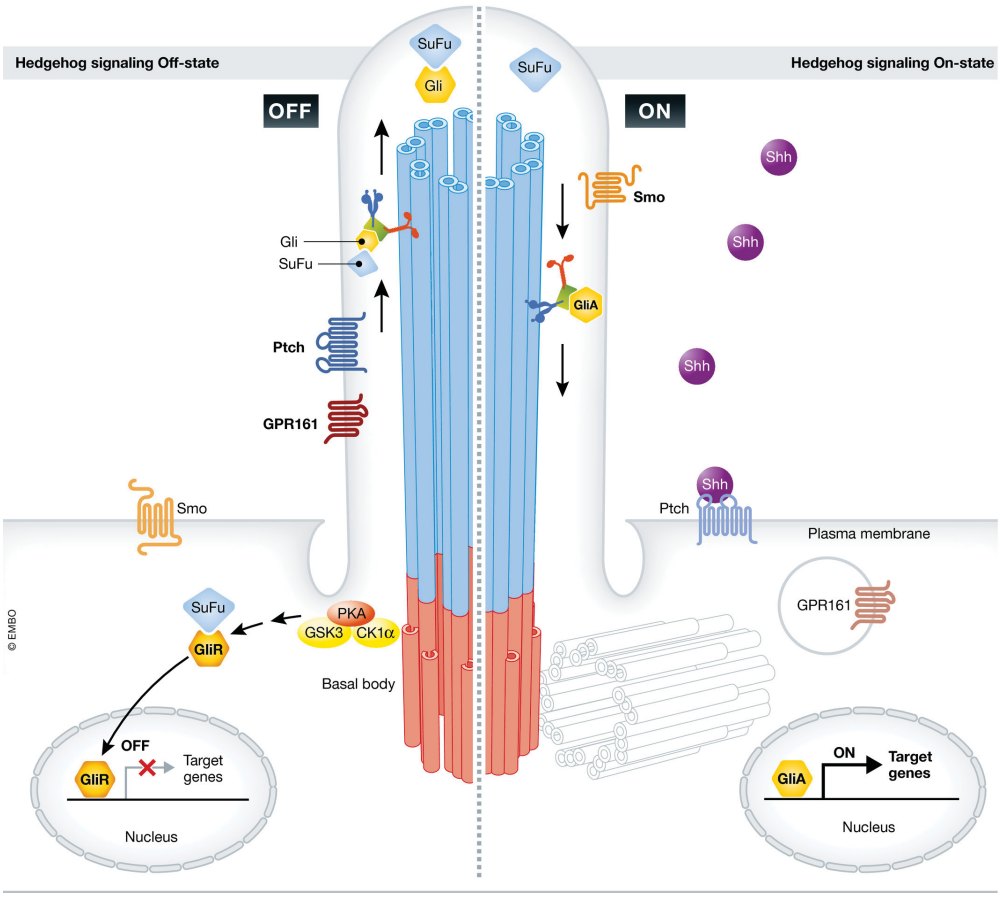

Figure 3: Primary cilia and sonic hedgehog (SHH) signaling. In the off-state of the pathway (when SHH ligand is absent), patched 1 (PTCH1) and G-protein coupled receptor 161 (GPR161) are present on the ciliary membrane, thereby repressing smoothened (SMO), and suppressor of fused (SUFU) forms a complex with GLI activators at the ciliary tip. Upon phosphorylation at the basal body by protein kinase A (PKA), glycogen synthase kinase 3 (GSK3) and casein kinase 1α (CK1α), GLI repressors translocate to the nucleus and inhibit the transcription of SHH target genes. In contrast, in the on-state of the pathway (when SHH ligand is present), PTCH1 is displaced from the primary cilium, thereby allowing ciliary accumulation and activation of SMO, and GLI activators translocate to the nucleus and induce the transcription of SHH target genes. Adapted from Eguether and Hahne[86].

First described by Huangfu and colleagues in 2003, numerous studies investigating the link between SHH signaling and cilia followed with the striking result that all key components of the SHH pathway are enriched in the cilium[88–92]. The regulation of this pathway is extremely sophisticated. Briefly, when SHH ligand is absent (thus, in the off-state of the pathway), patched 1 (PTCH1) localizes to the primary cilium, thereby repressing smoothened (SMO), and GLI repressors translocate to the nucleus and inhibit the transcription of SHH target genes. In contrast, when SHH ligand is present (thus, in the on-state of the pathway), PTCH1 is displaced from the primary cilium, thereby allowing ciliary accumulation and activation of SMO, and GLI activators translocate to the nucleus and induce the transcription of SHH target genes. Overall, three GLI proteins are thought to exist in a microtubule-associated complex together with suppressor of fused (SUFU). Pathway activity is regulated through posttranslational modification of GLI proteins, with GLI1 and GLI2 primarily acting as transcriptional activators, while GLI3 has both activator and repressor functions[93].

Another key regulator of development is WNT signaling, with the role of primary cilia in WNT signaling remaining controversial[87]. Several studies have shown that defects in primary cilia aberrantly activate WNT signaling, while other studies have shown that primary cilia are not required for WNT signaling[92,94–96]. In short, when WNT ligand is absent, beta-catenin is phosphorylated by the beta-catenin destruction complex, resulting in its proteasomal degradation. In contrast, when WNT ligand is present, WNT signaling is activated by binding of WNT ligand to frizzled receptors. Following, disheveled (DVL) mediates destabilization of the beta-catenin destruction complex, leading to stabilization and localization of beta-catenin to the nucleus for transcriptional activation of WNT target genes[97].

In addition, components of the Notch pathway have been shown to localize to the primary cilium or its basal body[87]. The way Notch signaling is regulated by the primary cilium, though, appears to be cell type and context specific[98–100]. Briefly, a Notch transmembrane receptor interacts with a Notch transmembrane ligand on a contacting cell, thereby initiating proteolytic cleavage of the receptor. Following, the intracellular

domain of the Notch receptor is released, translocates to the nucleus and initiates the transcription of Notch target genes[101].

Primary cilia are also reported to regulate receptor tyrosine kinases (RTKs). The best-studied RTKs are platelet-derived growth factor receptor (PDGFR) and transforming growth factor-beta (TGF-beta) receptor, but also other growth factor receptors have been identified to be regulated by primary cilia, including fibroblast growth factor receptor (FGFR), epidermal growth factor receptor (EGFR) and insulin-like growth factor receptor (IGFR)[87]. Ligand-binding to the respective receptor induces phosphorylation of its cytoplasmic tyrosine kinase domain. Phosphorylation, thereupon, allows recruitment of adaptor proteins, resulting in the activation of different signaling pathways, including the mitogen-activated protein kinase (MAPK) pathway and the phosphoinositide-3-kinase (PI3K)/AKT serine/threonine kinase (AKT)/mechanistic target of rapamycin kinase (mTOR) pathway[102]. PDGFR is present in two isoforms, PDGFR-alpha and PDGFR-beta. Indeed, PDGF-alpha receptors, but not PDGF-beta receptors, have been shown to localize to primary cilia in fibroblasts[103]. TGF-beta receptors have been shown to localize to primary cilia in fibroblasts as well, and also localization of TGF-beta receptors to endocytic vesicles at the ciliary base has been reported[104].

Indeed, amongst others, aberrant activation of the above-mentioned signaling pathways has been implicated in the development of different types of cancers and has also been associated with primary cilia (Figure 4).

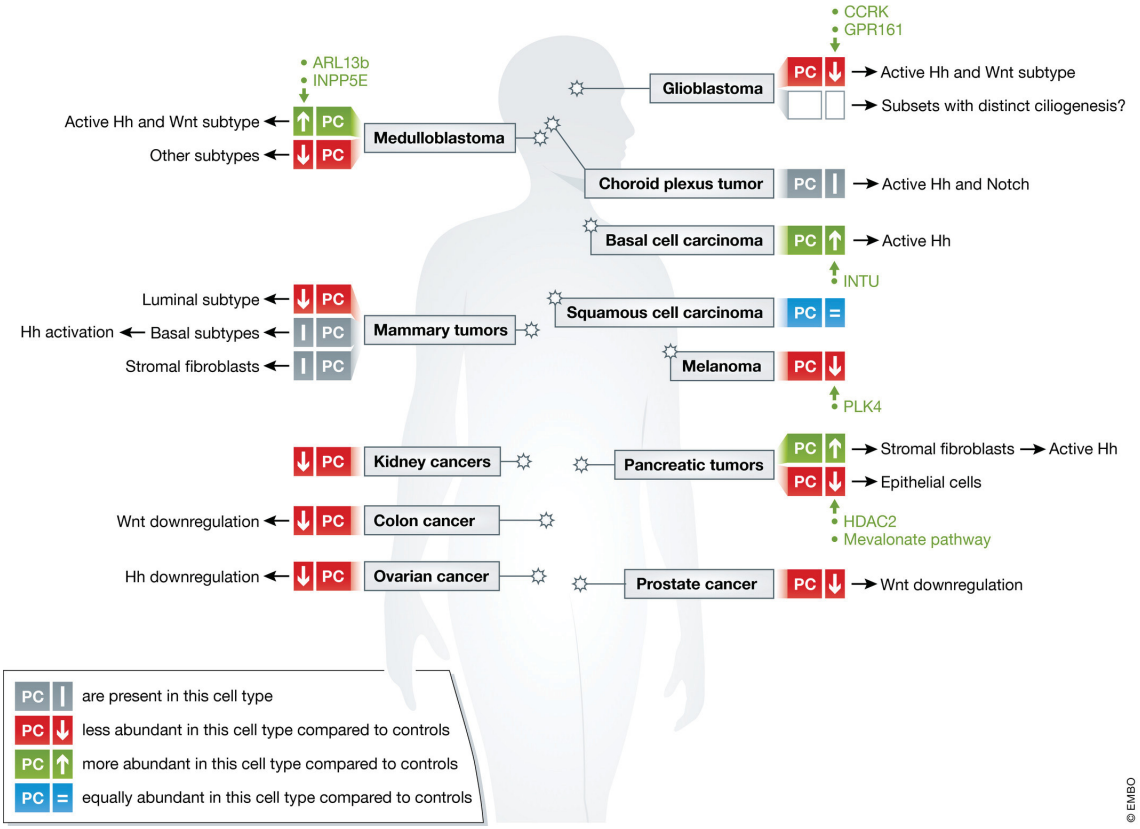

Figure 4: Primary cilia and its reported functions in different types of cancer. Adapted from Eguether and Hahne[86].

In SHH-driven medulloblastoma, for instance, a dual and opposing role for primary cilia has been suggested, depending on the initiating oncogenic event[105]. This has been also shown for SHH-driven basal cell carcinoma (BCC)[106]. In both cases, primary cilia have been proposed to act as mediators of tumorigenesis when the cells were dependent on upstream activation of the SHH pathway and as suppressors of tumorigenesis when the cells were dependent on downstream activation of the SHH pathway. Indeed, several cilia-associated tumor regulators have been recently identified for SHH-driven medulloblastoma (the inositol phosphatase INPP5E, the GTPase ARL13B and the G-protein-coupled receptor GPR161) and for SHH-driven BCC (the planar cell polarity protein INTU)[107,108]. In addition, primary cilia have been detected in small subpopulations of glioblastoma biopsies and glioblastoma primary cells, and their presence has been shown to correlate with the expression of Ki-67 (a marker for actively dividing cells) and ZEB1 (a transcription factor linked to tumor initiation, invasion and chemoresistance), supporting a role for primary cilia in glioblastoma initiation and

propagation[109]. On the contrary, other studies have reported that loss of primary cilia is a common feature of glioblastoma that contributes to the malignant phenotype of this devastating disease[110,111]. Two suggested cilia-associated tumor regulators for glioblastoma are cell cycle related kinase (CCRK) and lysophosphatidic acid receptor 1 (LPAR1)[112,113]. Another brain tumor entity associated with primary cilia is choroid plexus (CP) tumor, a rare type of pediatric brain tumor. While normal CP epithelium has been shown to comprise only multi-ciliated cells, CP tumors display only one primary cilium. Referring to this, a model has been suggested that supports the idea that in CP tumors aberrantly activated Notch signaling regulates SHH signaling by controlling ciliary localization of key components of its transduction machinery[101,114]. Primary cilia appear to also have a role in the development of melanoma. While melanocytic nevi have been shown to prominently comprise primary cilia, an almost complete loss of this organelle has been described in further advanced stages, including melanoma *in situ*, invasive melanoma and metastatic melanoma[115]. It has been suggested that EZH2 drives the suppression of ciliary genes that results in the disassembly of primary cilia and, in turn, to aberrantly activated WNT signaling[116]. Next to brain and skin cancers, the role of primary cilia has been also investigated in epithelial cancers, including breast, pancreatic, renal, ovarian, gastrointestinal and prostate cancers. In breast cancers, for instance, hardly any primary cilia have been detected, but if present, they have been found to be required for the maintenance of tumor-initiating cells[117–119]. In pancreatic cancers, only stromal fibroblasts, but not epithelial cells, have been shown to display primary cilia, suggesting a model that formation of primary cilia in stromal fibroblasts is triggered by SHH that is secreted by the pancreatic epithelium[120]. Although the number of primary cilia has been reported to decrease during tumor progression, their presence has been correlated with an increased number of lymph node metastasis and, thus, with poor overall survival[121,122]. Suggested cilia-associated tumor regulators for pancreatic cancers include HDAC2 and AURKA[123]. Loss of primary cilia has been also reported for clear cell renal cell carcinomas (ccRCC), the most frequent type of kidney cancer. Specifically, a role for beta-catenin in regulating AURKA and formation of primary cilia in the setting of von Hippel-Lindau (VHL) deficiency, the hallmark of ccRCC, has been suggested[124,125]. The frequency of primary cilia has been shown to be also decreased in

neoplastic ovarian surface epithelium (OSE) compared to normal OSE. It has been suggested that this, in part, also results from the overexpression of AURKA, leading to aberrant SHH and PDGF signaling[126]. A decreased number of primary cilia has been also reported for gastrointestinal cancers. Interestingly, higher frequency of primary cilia has been shown to correlate with longer overall survival. Additionally, a correlation of primary cilia with programmed cell death protein 1 (PD1) and CD8+ tumor infiltrating lymphocytes (TILs) has been noted[127,128]. Loss of primary cilia in prostate cancer appears to result in increased WNT signaling[129]. A role for primary cilia has been also reported for rhabdomyosarcoma and chondrosarcoma[130,131].

Taking all this evidence together, it can be noted that primary cilia, through their absence or dysfunction, contribute to the development of different types of cancers by modulating established cancer signaling pathways, including SHH, WNT, Notch and RTK signaling pathways. Even though the importance of primary cilia in cancer is clearly emerging, further studies are required to fully understand the association between primary cilia and tumorigenesis.

2 Aim of the thesis

For decades, primary cilia have been regarded as rudimentary organelles. Today, however, it is known that primary cilia are crucial regulators of cell signaling and contribute to the development of different types of cancers. So far, the association between primary cilia and cancer is not fully understood, since the way primary cilia regulate tumorigenesis seems to differ between tumor types and within tumor subtypes. Given the fact that the importance of primary cilia in cancer is clearly emerging and that the overexpression of genes involved in ciliogenesis has been recently described also for AT/RTs (specifically for the AT/RT-TYR subgroup), the aim of this thesis was to elucidate the functional role of primary cilia in AT/RT biology by characterizing their distribution across AT/RT subgroups and by targeting primary ciliogenesis in these tumors with dismal prognosis according to the following strategy:

1. Detection and quantification of primary cilia in AT/RT patient samples and cell lines.
2. Disruption of primary ciliogenesis *in vitro* using two different approaches (transient and stable knockdown of *KIF3A* and treatment with Ciliobrevin D) and analysis of the functional consequences.
3. Identification of the mechanism using proteogenomic profiling.
4. Analysis of the relevance of primary ciliogenesis in AT/RT biology *in vivo* using two different approaches (a *Drosophila* model of *SMARCB1* deficiency and an orthotopic xenograft mouse model of AT/RT).
5. Analysis of the vulnerability towards an in-house established clinical compound library following disruption of primary ciliogenesis.

3 Materials and methods

3.1 Materials

3.1.1 AT/RT patient samples

In this thesis, anonymized tumor tissue sections of 13 AT/RT patients were examined. These were kindly provided by Prof. Dr. Martin Hasselblatt from the Institute of Neuropathology at the University Hospital in Münster, Germany. For AT/RT subgroup classification, 450k methylation array profiling was performed at the German Cancer Research Center in Heidelberg, Germany, using the Infinium HumanMethylation450 BeadChip from Illumina, San Diego, USA, as described previously[61]. Samples had been obtained in the context of the European Rhabdoid Tumor Registry EU-RHAB. EU-RHAB has received ethical committee approval (Ethics committee of the University Hospital Münster, 2009-532-f-S) and all parents gave informed consent for scientific use of the archival samples. To protect the patients´ privacy, all personal data were anonymized.

3.1.2 Cell lines

3.1.2.1 AT/RT cell lines

In this thesis, two AT/RT cell lines (BT-12 and CHLA-266) were examined. Both cell lines were kindly provided by the Children's Oncology Group (COG) Cell Culture and Xenograft Repository, Lubbock, USA.

3.1.2.2 HEK293T cells

HEK293T cells were obtained from the American Type Culture Collection (ATCC), Manassas, USA, and were used for the production of lentiviral particles.

3.1.3 Media and supplements

All media and supplements used in this thesis are listed in Table 1.

Table 1: Media and supplements

Name	Company	Reference #
Dimethylsulfoxide (DMSO)	AppliChem, Darmstadt, Germany	A3672
Dulbecco's modified eagle's medium (DMEM, 1x), high glucose, GlutaMAX™ Supplement, pyruvate	Gibco, Darmstadt, Germany	31966021
Fetal bovine serum (FBS), heat-inactivated	Sigma-Aldrich, Taufkirchen, Germany	F9665
Iscove's modified dulbecco's medium (IMDM, 1x)	Gibco, Darmstadt, Germany	12440053
Insulin-Transferrin-Selenium (ITS) (100x)	Gibco, Darmstadt, Germany	41400045
Opti-MEM™	Gibco, Darmstadt, Germany	31985062
Phosphate buffered saline (PBS)	Sigma-Aldrich, Taufkirchen, Germany	D8537
Puromycin	InvivoGen, San Diego, USA	ant-pr-1

3.1.4 Buffers

All buffers used in this thesis are listed in Table 2.

Table 2: Buffers

Name	Composition
Blocking Solution	5% Bovine Serum Albumin (BSA) dissolved in TBS-T
Citrate Antigen Retrieval Solution (10x)	100 mM Citrate (pH 6.0) dissolved in ddH_2O
IDTE buffer	10 mM Tris; 0.1 mM EDTA (pH 8.0)
M-MLV RT 5x Buffer	Promega, Madison, USA (Reference #M531A)
PBS-T	PBS; 0.1% Tween 20
RIPA Lysis Buffer (10x)	Sigma-Aldrich, Taufkirchen, Germany (Reference #20-188)

Sample Buffer (5x)	1 M Tris/HCL (pH 6.8); 62.5% (v/v) Glycerin; 10% (w/v) Sodium Dodecyl Sulfate (SDS)
TBS-T	20 mM Tris (pH 7.5); 150 mM NaCl; 0.1% Tween 20
Tris-Glycine SDS Running Buffer	Novex, Darmstadt, Germany (Reference #LC2675)
Transfer Buffer (10x)	25 mM Tris; 190 mM Glycine

3.1.5 Chemicals

All chemicals used in this thesis are listed in Table 3.

Table 3: Chemicals

Name	Company	Reference #
16% Formaldehyde Solution (w/v)	Thermo Fisher Scientific, Bremen, Germany	28908
2-Propanol	VWR Chemicals, Fontenay-sous-Bois, France	20.842.330
BSA	Roth, Karlsruhe, Germany	8076.4
Chloroform	Merck, Darmstadt, Germany	102.445
Citric Acid	Sigma-Aldrich, Taufkirchen, Germany	C-8532
Crystal Violet	Fluka, Schwerte, Germany	32675
Ethanol (EtOH) absolute	VWR Chemicals, Fontenay-sous-Bois, France	20.821.330
Formalin 10% Neutral Buffered	ScyTek Laboratories, Hamburg, Germany	FRN999
Glycine	Roth, Karlsruhe, Germany	3908.2
Sodium Citrate	Roth, Karlsruhe, Germany	3580.1
Sudan Black B	Sigma-Aldrich, Taufkirchen, Germany	199664
Tris	Roth, Karlsruhe, Germany	5429.1
Triton X 100	Roth, Karlsruhe, Germany	6683.1
TRIzol™ Reagent	Thermo Fisher Scientific, Bremen, Germany	15596018
Tween® 20	Merck, Darmstadt, Germany	8.221.840.500
Xylol (Isomere)	Roth, Karlsruhe, Germany	9713.3

3.1.6 Specific reagents and other materials

All specific reagents and other materials used in this thesis are listed in Table 4.

Table 4: Specific reagents and other materials

Name	Company	Reference #
Amersham™ Protran™ 0.45 µm NC	GE Healthcare, Chicago, USA	10600002
D4+ Dispensehead Cassettes	HP, Böblingen, Germany	FOL60A
Eukitt Quick-Hardening Mounting Medium	Fluka, Schwerte, Germany	3989
Goat Serum	Sigma-Aldrich, Taufkirchen, Germany	G9023
GoTaq® qPCR Master Mix (2x)	Promega, Madison, USA	A600A
Lipofectamine™ RNAiMAX Transfection Reagent	Invitrogen, Darmstadt, Germany	13778150
Novex™ WedgeWell™ 4-12% Tris-Glycine Gel	Invitrogen, Darmstadt, Germany	XP04122BOX
Oligo(dT) Primer	Promega, Madison, USA	C110A
PageRuler™ Prestained Protein Ladder	Thermo Fisher Scientific, Bremen, Germany	26616
Phosphatase Inhibitor Cocktail	Roche, Basel, Switzerland	4906837001
Polyethylenimine (PEI)	Merck, Darmstadt, Germany	408727
Precision Blue Real-Time PCR Dye	Merck, Darmstadt, Germany	1722-5555
Propidium Iodide (PI)	Sigma-Aldrich, Taufkirchen, Germany	P4864
Protease Inhibitor Cocktail	Roche, Basel, Switzerland	4693132001
Protein Assay Dye Reagent Concentrate	Bio-Rad, Hercules, USA	500-0006
Protein Standard	Sigma-Aldrich, Taufkirchen, Germany	P0914
Random Primer	Promega, Madison, USA	34095
SuperSignal™ West Femto Maximum Sensitivity Substrate	Thermo Fisher Scientific, Bremen, Germany	C118A
T8+ Dispensehead Cassettes	HP, Böblingen, Germany	FOL59A
TaqMan® Gene Expression Master Mix	Applied Biosystems, Foster City, USA	4369016
Trypsin-EDTA (1x)	Gibco, Darmstadt, Germany	25300054

Vectashield Mounting Medium for Fluorescence	Vector Laboratories, Eching, Germany	H-1000
Whatman™ Gel Blot Paper	GE Healthcare, Chicago, USA	GB003

3.1.7 Plasmids

The plasmids used in this thesis are listed in Table 5.

Table 5: Plasmids

Name	Company	Reference #
pLK0.1 - TRC cloning vector	AddGene, Watertown, USA	10878
pLV hU6-sgRNA hUbc-dCas9-KRAB-T2a-Puro	A kind gift from Charles Gersbach	

3.1.8 Small hairpin RNA (shRNA) and CRISPR interference (CRISPRi) sequences

The small hairpin RNA (shRNA) and CRISPR interference (CRISPRi) sequences used in this thesis are listed in Table 6.

Table 6: Small hairpin RNA (shRNA) and CRISPR interference (CRISPRi) sequences

Name	Sequence
shCTRL-fwd	CCGGTCCTAAGGTTAAGTCGCCCTCGCTCGAGCGAGGGCGACTTAACCTTAGGTTTTTG
shCTRL-rev	AATTCAAAAACCTAAGGTTAAGTCGCCCTCGCTCGAGCGAGGGCGACTTAACCTTAGGA
shKIF3A-fwd	CCGGCGTCAGTCTTTGATGAAACTACTCGAGTAGTTTCATCAAAGACTGACGTTTTTG
shKIF3A-rev	AATTCAAAAACGTCAGTCTTTGATGAAACTACTCGAGTAGTTTCATCAAAGACTGACG
CRISPRiCTRL-fwd	CACCGGAGACGGACGTCTCA
CRISPRiCTRL-rev	AAACTGAGACGTCCGTCTCC
CRISPRiKIF3A-fwd	CACCGCGAGGTGTTTCGGTAGTCTC
CRISPRiKIF3A-rev	AAACGAGACTACCGAAACACCTCGC

3.1.9 Primers

The following primers were used for GoTaq® real-time PCR and were obtained from IDT Integrated DNA Technologies, Iowa, USA (see Table 7). Primers were provided as 25 nmol DNA oligonucleotides and were resuspended to a 100 µM stock solution in ddH_2O. Forward (fwd) and reverse (rev) primers were diluted and combined to a 10 µM primer mix working solution.

Table 7: Primer for GoTaq® real-time PCR

Name	Sequence (5´ → 3´)
DR5-fwd	CCTGAGCAGGAAATGGAAGT
DR5-rev	GCCTCCTCCTCTGAGACCTT
GAPDH-fwd	GTCAGCCGCATCTTCTTTTG
GAPDH-rev	GCGCCCAATACGACCAAATC
IFI35-fwd	CACGATCAACATGGAGGAGTGC
IFI35-rev	GGCAGGAAATCCAGTGACCAAC
IFIT1-fwd	GCCTTGCTGAAGTGTGGAGGAA
IFIT1-rev	ATCCAGGCGATAGGCAGAGATC
IFIT3-fwd	CCTGGAATGCTTACGGCAAGCT
IFIT3-rev	GAGCATCTGAGAGTCTGCCCAA
ISG15-fwd	CTCTGAGCATCCTGGTGAGGAA
ISG15-rev	AAGGTCAGCCAGAACAGGTCGT
KIF3A-fwd	TCCCAATTCATTTGCTCACA
KIF3A-rev	GTCTGATCCTTGCCCAAAAG
MX1-fwd	GGCTGTTTACCAGACTCCGACA
MX1-rev	CACAAAGCCTGGCAGCTCTCTA
OAS1-fwd	AGGAAAGGTGCTTCCGAGGTAG
OAS1-rev	GGACTGAGGAAGACAACCAGGT
OAS2-fwd	GCTTCCGACAATCAACAGCCAAG
OAS2-rev	CTTGACGATTTTGTGCCGCTCG
OAS3-fwd	CCTGATTCTGCTGGTGAAGCAC
OAS3-rev	TCCCAGGCAAAGATGGTGAGGA
PGK1-fwd	GACAGCAGCCTTAATCCTCTG
PGK1-rev	CTAACAAGCTGACGCTGGA
STAT1-fwd	ATGGCAGTCTGGCGGCTGAATT
STAT1-rev	CCAAACCAGGCTGGCACAATTG

DR5: death receptor 5, GAPDH: glyceraldehyde 3-phosphate dehydrogenase, IFI35: interferon-induced protein 35, IFIT: interferon-induced protein with tetratricopeptide repeats, ISG15: ISG15 ubiquitin like modifier, KIF3A: kinesin family member 3A, MX1: MX dynamin like GTPase 1, OAS: 2'-5'-oligoadenylate synthetase, PGK1: phosphoglycerate kinase 1, STAT1: signal transducer and activator of transcription 1

The primers listed in Table 8 were used for TaqMan® real-time PCR and were obtained from IDT Integrated DNA Technologies, Iowa, USA. Primers were provided as PrimeTime Std qPCR Assays and were resuspended in IDTE buffer to a 20x working solution.

Table 8: Primer for TaqMan® real-time PCR

Name	Assay name
GAPDH	Hs.PT.39a.22214836
GLI1	Hs.PT.58.26486279
PGK1	Hs.PT.58v.606641
PTCH1	Hs.PT.58.4907689
SMO	Hs.PT.58.26167982

GAPDH: glyceraldehyde 3-phosphate dehydrogenase, GLI1: glioma-associated oncogene 1; PGK1: phosphoglycerate kinase 1, PTCH1: patched 1, SMO: smoothened

3.1.10 Enzymes

The enzymes used in this thesis are listed in Table 9.

Table 9: Enzymes

Name	Company	Reference #
M-MLV Reverse Transcriptase	Promega, Madison, USA	M3681
RNase A (DNase-free)	AppliChem, Darmstadt, Germany	A3832
RNasin® Ribonuclease Inhibitor	Promega, Madison, USA	N2511

3.1.11 Antibodies

3.1.11.1 Western blot analyses

The antibodies used for western blot analyses in this thesis are listed in Table 10.

Table 10: Antibodies used for western blot analyses

Name	Company	Reference #	Dilution
Actin (C4)	EMD Millipore, Burlington, USA	MAB1501	1:5000
Anti-Mouse IgG, HRP-linked	Cell Signaling Technology, Cambridge, UK	7076	1:5000

Anti-Rabbit IgG, HRP-linked	Cell Signaling Technology, Cambridge, UK	7074	1:5000
DR5 (D4E9) XP® Rabbit mAB	Cell Signaling Technology, Cambridge, UK	8074	1:1000
KIF3A (D763) Rabbit mAB	Cell Signaling Technology, Cambridge, UK	8507	1:1000
Phospho-STAT1 (Tyr701) (58D6) Rabbit mAB	Cell Signaling Technology, Cambridge, UK	9172	1:1000
STAT1 Rabbit pAB	Cell Signaling Technology, Cambridge, UK	9172	1:1000

DR5: death receptor 5, KIF3A: kinesin family member 3A, STAT1: signal transducer and activator of transcription 1

3.1.11.2 Immunofluorescence analyses

The antibodies used for immunofluorescence analyses in this thesis are listed in Table 11.

Table 11: Antibodies used for immunofluorescence analyses

Name	Company	Reference #	Dilution
4´,6-Diamidin-2-phenylindol (DAPI)	Thermo Fisher Scientific, Bremen, Germany	62248	1:1000
Acetylated tubulin (6-11B-1) Mouse mAB	Sigma-Aldrich, Taufkirchen, Germany	T6793	1:500
Chicken anti-Rabbit IgG, Alexa Fluor 488	Thermo Fisher Scientific, Bremen, Germany	A-21441	1:2500
Goat anti-Mouse IgG2b, Alexa Fluor 594	Thermo Fisher Scientific, Bremen, Germany	A-21145	1:2500
Pericentrin Rabbit pAB	Abcam, Cambridge, UK	ab4448	1:500

3.1.12 Commercially available kits

The commercially available kits used in this thesis are listed in Table 12.

Table 12: Commercially available kits

Name	Company	Reference #
CellTiter-Glo® Luminescent Cell Viability Assay	Promega, Madison, USA	G7572
Click-iT® EdU Alexa Fluor® 488 Imaging Kit	Invitrogen, Darmstadt, Germany	C10337
Fluorescein isothiocyanat (FITC) Annexin V	BD Biosciences, San Jose, USA	556419 (FITC Annexin V) 556454 (Annexin V Binding Buffer)

3.1.13 Other consumables

All other consumables, including glass- and plasticware, used in this thesis are listed in Table 13.

Table 13: Consumables

Name	Company	Reference #
384-Well Clear Polystyrene Microplate	Corning, Wiesbaden, Germany	3701
384-Well White Polystyrene Microplate	Corning, Wiesbaden, Germany	3570
Cell culture dishes (10 cm Ø & 15 cm Ø)	Greiner Bio-One, Solingen, Germany	664160 639160
Cell culture flasks (25 cm^2 & 75 cm^2)	Greiner Bio-One, Solingen, Germany	690175 658175
Cell culture plates (12-well & 6-well)	Greiner Bio-One, Solingen, Germany	665102 657185
Centrifuge tubes (1.5 ml & 2 ml)	Eppendorf, Hamburg, Germany	0030123.328 0030123.344
Cover Slips (24 x 50 mm)	VWR, Darmstadt, Germany	
Falcon tubes (15 ml & 50 ml)	Greiner Bio-One, Solingen, Germany	188271 227261
Filtropur S 0.45	Sarstedt, Nümbrecht, Germany	83.1826
Hard-Shell® 384-Well PCR Plates	Bio-Rad, Hercules, USA	HSP3805
Injekt® Single-use syringes (20 ml)	Braun, Melsungen, Germany	4606205V

Microscope Cover Glasses (18 mm Ø)	VWR, Darmstadt, Germany	631-1580
Microscope Slides (24 x 60 mm)	Engelbrecht, Edermünde, Germany	K12460
Nunc™ Lab-Tek™ II Chamber Slide™ System	Thermo Fisher Scientific, Bremen, Germany	154534

3.1.14 Devices

Laboratory equipment and other devices used in this thesis are listed in Table 14.

Table 14: Devices

Name	Company
Allegra™ X-12R Centrifuge	Beckman Coulter, Krefeld, Germany
ApoTome.2	Zeiss, Oberkochen, Germany
Axio Observer.Z1	Zeiss, Oberkochen, Germany
Axio Vert.A1	Zeiss, Oberkochen, Germany
CFX384™ Real-Time System	Bio-Rad, Hercules, USA
CO_2 incubator for cell culture (HERA cell)	Heraeus, Hanau, Germany
Cryo-Safe™ Cooler	Bel-Art Products, Warminster, USA
CytoFLEX	Beckman Coulter, Krefeld, Germany
D300(e) Digital Dispenser	Tecan, Männedorf, Switzerland
Electrophoresis Power Supply	Peqlab, Darmstadt, Germany
GeneAmp® PCR System 2700	Applied Biosystems, Foster City, USA
LAS-3000 mini 2UV Transilluminator	Fujifilm, Düsseldorf, Germany
Megafuge 3.0R	Heraeus, Hanau, Germany
Milli-Q Integral 15	Merck, Darmstadt, Germany
Mini Blot Module	Invitrogen, Darmstadt, Germany
Mini Gel Tank	Invitrogen, Darmstadt, Germany
Mini Rocker-Shaker	Peqlab, Darmstadt, Germany
Multidrop Combi Reagent Dispenser	Thermo Fisher Scientific, Bremen, Germany
Multifuge X3R	Thermo Fisher Scientific, Bremen, Germany
NanoDrop Spectrophotometer ND-1000	Peqlab, Darmstadt, Germany
peqMIX Plus	Peqlab, Darmstadt, Germany
peqTWIST	Peqlab, Darmstadt, Germany

PerfectSpin 24R Refrigerated Microcentrifuge	Peqlab, Darmstadt, Germany
PH meter 7310	Inolab, Weilheim, Germany
Roller Mixer (SRT6)	Stuart, Stone, UK
Scout^{TM} Pro	Ohaus, Nänikon, Switzerland
Spark 10M Microplate Reader	Tecan, Männedorf, Switzerland
ThermoMixer C	Eppendorf, Hamburg, Germany
Vi-cell XR Cell Viability Analyzer	Beckman Coulter, Krefeld, Germany

3.1.15 Software

The different types of softwares used for data analyses in this thesis are listed in Table 15.

Table 15: Software

Name	Company
Adobe Photoshop	Adobe Inc., San Jose, USA
Bio-Rad CFX Manager	Bio-Rad, Hercules, USA
CytExpert	Beckman Coulter, Krefeld, Germany
D300(e)Control	Tecan, Männedorf, Switzerland
FILLit for Multidrop Combi 1.2.1	Thermo Fisher Scientific, Bremen, Germany
GIMP 2	https://www.gimp.org/
GraphPad Prism 5.03	GraphPad Software, San Diego, USA
Inkscape 0.92.3	https://inkscape.org/de/
Partek Flow & Partek Genomics Suite	Partek Incorporated, Missouri, USA
Python	Python Software Foundation, Wilmington, USA

3.2 Methods

3.2.1 Cell cultivation

AT/RT cell lines BT-12 and CHLA-266 were maintained as monolayer cultures in complete medium, consisting of IMDM supplemented with 20% FBS and 1x ITS. Cells were incubated at 37 °C in a 5% CO_2 atmosphere. Medium of stably transduced cell lines was supplemented with 0.5 µg/ml puromycin. For cell cultivation, BT-12 and CHLA-266 cells were split twice a week in a 1:10 and 1:5 ratio, respectively. The total number of viable cells was regularly determined using the Vi-cell XR Cell Viability Analyzer from Beckman Coulter. For serum starvation experiments, BT-12 and CHLA-266 cells were seeded in complete medium. The next day, complete medium was replaced with medium lacking serum for 72 h.

HEK293T cells were maintained as monolayer cultures in complete medium, consisting of DMEM supplemented with 10% FBS. Cells were incubated at 37 °C in a 5% CO_2 atmosphere. For cell cultivation, HEK293T cells were split twice a week in a 1:10 ratio. The total number of viable cells was regularly determined using the Vi-cell XR Cell Viability Analyzer from Beckman Coulter.

3.2.2 Cell cryopreservation

Cells were removed from the cell culture flask using Trypsin-EDTA. After centrifugation for 5 min at 200-times gravity (xg), about $2.5x10^6$ cells/ml were resuspended in 800 µl freezing medium, consisting of complete medium supplemented with 10% DMSO, and transferred to a cryogenic storage vial. Cells were frozen slowly at 1 °C/min in a Cryo-Safe™ Cooler filled with 2-propanol at -80 °C for at least 24 h. For long term storage, the cells were kept in the gas phase of liquid nitrogen. For re-cultivation, the cryogenic storage vial was thawn in a water bath at 37 °C. In order to completely remove the freezing medium, the cells were centrifuged for 5 min at 200 xg and resuspended in fresh cell culture medium.

3.2.3 Immunofluorescence

For the detection of primary cilia, AT/RT tissues and cell lines were stained with rabbit anti-Pericentrin and mouse anti-Acetylated tubulin primary antibodies, detecting the basal body and the axoneme of the primary cilium, respectively. Secondary antibodies were species-specific and conjugated with fluorescence tags (for description of the antibodies see 3.1.11.2).

AT/RT cell lines, grown on coverslips in 12-well plates, were washed with PBS and fixed and permeabilized with 4% formaldehyde solution supplemented with 0.1% Triton X 100 in PBS-T for 20 min at room temperature (RT). In order to block unspecific binding sites, cells were incubated with 1% BSA and 3% goat serum in PBS-T for 1 h at RT. Subsequently, cells were incubated with primary antibodies diluted in blocking solution overnight at 4 °C. The next day, cells were washed three times with PBS for 5 min at RT and incubated with secondary antibodies diluted in blocking solution for 45 min at RT. Following one washing step with PBS for 5 min at RT, cells were counterstained with DAPI diluted in PBS for 3 min at RT and washed two times with PBS for 5 min at RT. Finally, coverslips were mounted on glass slides using Vectashield Mounting Medium for Fluorescence and Eukitt Quick-Hardening Mounting Medium.

Paraffin AT/RT tissue sections were de-paraffined by two-time incubation in 100% xylene for 5 min at RT followed by the incubation in an alcohol dilution series at RT (three-time incubation in 100% EtOH for 3 min, two-time incubation in 95% EtOH for 2 min and one-time incubation in 70% EtOH for 1 min). Subsequently, tissue sections were washed with PBS and boiled in citrate solution for antigen retrieval for 30 min. Blocking of unspecific binding sites and staining for primary cilia was performed as described above. Before mounting, tissue sections were incubated in 1% Sudan Black B in 70% EtOH for 10 min at RT and washed with 70% EtOH afterwards in order to diminish autofluorescence.

Stained coverslips and tissue sections were analyzed using the Axio Observer.Z1 with a 63x oil objective and the ApoTome.2 from Zeiss.

3.2.4 Quantification of ciliated cells

For the quantification of ciliated cells, at least three randomly selected microscopic fields per coverslip/tissue section were examined. All images were captured as z-stacks of at least 20 images. The percentage of ciliated cells was calculated by counting the number of DAPI-labeled cells and the number of primary cilia and taking its ratio afterwards.

3.2.5 RNA interference using small interfering RNA (siRNA)

Transient knockdown of *KIF3A* was achieved using small interfering RNA (siRNA) pools (siPOOLs). siPOOLs are complex pools of 30 selected siRNA sequences that were demonstrated to efficiently remove off-target effects and improve the reliability of the results. This is achieved by diluting the concentrations of the individual siRNAs below thresholds that stimulate phenotypes. The siRNA sequences within siPOOLs are also optimized for maximal transcript coverage that enables highly efficient and specific gene silencing[132].

For RNA interference using siRNA, KIF3A siPOOLs (siKIF3A, #11127) and negative control siPOOLs (siCTRL) were obtained from siTOOLs Biotech, Martinsried, Germany. BT-12 ($2.5x10^5$ cells/well) and CHLA-266 ($5x10^5$ cells/well) cells were seeded on 6-well plates. The next day, transfection of siPOOLs was performed using Lipofectamin® RNAiMAX Reagent according to the manufacturer's instructions.

3.2.6 Generation of stable cell lines

Stable knockdown of *KIF3A* was achieved using lentiviral vectors. While stable knockdown of *KIF3A* was accomplished using shRNA-based technology in BT-12 cells, this technology did not work for CHLA-266 cells. Therefore, CRISPRi-based technology was used for this cell line. CRISPRi offers a complementary approach to RNAi, with the difference that CRISPRi controls genes primarily at the transcriptional level, while RNAi

regulates gene expression at the mRNA level. Specifically, the technology employs a catalytically dead Cas9 (commonly designated as dCas9) protein lacking endonuclease activity to regulate genes in an RNA-guided manner. Target specificity is ascertained by complementary base-pairing of a single guide RNA (sgRNA) to the genomic locus[133].

3.2.6.1 RNA interference using short hairpin RNA (shRNA)

For RNA interference using short hairpin RNA (shRNA), the lentiviral vector backbone pLK0.1 - TRC was used. A set of shRNA oligos was obtained from IDT Integrated DNA Technologies, Iowa, USA (see Table 6).

3.2.6.1.1 Virus production

For the production of lentiviral particles, HEK293T cells were seeded on 10 cm dishes, so that they reached a confluence of approximately 75% on the following day. The next day, a transfection mix was prepared. First, lentiviral vector, helper and envelope plasmids (14 µg shCTRL or shKIF3A, 14 µg pMDL/pRRE, 5.5 µg pRSV-Rev and 3 µg pMD2.G) were mixed and the volume was adjusted to 2 ml using DMEM. In parallel, 2 ml of a polyethylenimine (PEI) solution was prepared by mixing 1 µl of a 10 mg/ml PEI stock solution and 2 ml DMEM. The plasmid solution was mixed with the PEI solution and was incubated for 10 min at RT. Meanwhile, HEK293T cells were placed with 7 ml of DMEM supplemented with 15% FBS. The DNA-PEI mixture was added to the medium and the contents of the dish were mixed. The medium was replaced with fresh medium 24 h after the transfection was initiated. Twenty-four hours after the medium change, the lentiviral-containing medium was collected and filtered through a 0.45 µm filter. Following, target cells were either directly infected with the virus solution or the virus solution was aliquoted and stored at -80°C until infection.

3.2.6.1.2 Virus infection

For the infection with lentiviral particles, BT-12 ($2.5x10^5$ cells/well) and CHLA-266 ($5x10^5$ cells/well) cells were seeded on 6-well plates. The next day, cells were infected with 2 ml/well of the respective virus solution (shCTRL or shKIF3A). In addition, 2 µg/ml of polybrene was added in order to increase the transduction efficiency. After 24 h, cells were washed three times with PBS. Subsequently, stably transduced cells were selected using 0.5 µg/ml puromycin.

3.2.6.2 CRISPR interference (CRISPRi)

For CRISPR interference (CRISPRi), the lentiviral vector backbone pLV hU6-sgRNA hUbc-dCas9-KRAB-T2a-Puro was used. Single guide RNAs (sgRNAs) were designed on the basis of Guide Design Resources (http://crispr.mit.edu/). A set of sgRNA oligos was obtained from IDT Integrated DNA Technologies, Iowa, USA (see Table 6). Virus production and virus infection was performed as described above.

3.2.7 RNA extraction, cDNA synthesis and quantitative real-time PCR

RNA was extracted using TRIzol® Reagent and cDNA was synthesized from 0.5 µg of total RNA using M-MLV Reverse Transcriptase according to the manufacturer's instructions. Table 16, Table 17 and Table 18 show the compositions and conditions for cDNA synthesis.

Table 16: Composition of Mix I for cDNA synthesis

	Mix I
RNA	0.5 µg
Random/Oligo(dT) Primer Mix	0.5 µl
H_2O	ad 14 µl

Mix I was incubated for 5 min at 70 °C. Afterwards, Mix I was incubated for at least 1 min at 4 °C.

Table 17: Composition of Mix II for cDNA synthesis

	Mix II
M-MLV RT 5x Buffer	5 µl
dNTP	1.25 µl
M-MLV Reverse Transcriptase	1 µl
RNasin® Ribonuclease Inhibitor	1 µl
H_2O	2.75 µl

Mix I was supplemented with 11 µl of Mix II and incubated under the following conditions:

Table 18: Conditions for cDNA synthesis

	Condition
1	25 °C for 10:00 min
2	50 °C for 50:00 min
3	70 °C for 15 min
4	4 °C ∞

Gene expression was determined by quantitative real-time PCR using the CFX384™ Real-Time System from Bio-Rad. *GAPDH* and *PGK1* served as housekeeping genes for normalization. Relative quantification of PCR products was conducted using the ΔΔCT method. Samples were quantified in triplets. Table 19 and Table 20 show the compositions and conditions for real-time PCR, respectively.

Table 19: Real-time PCR compositions

	GoTaq®	**TaqMan®**
Master Mix	5 µl	5 µl
Primer Mix	1 µl	0.5 µl
H_2O	3 µl	3.5 µl
cDNA	1 µl	1 µl

Table 20: Real-time PCR conditions

	GoTaq®	**TaqMan®**
1		50 °C for 02:00 min
2	95 °C for 02:00 min	95 °C for 10:00 min

3	95 °C for 00:03 min	95 °C for 00:15 min
4	60 °C for 00:30 min	60 °C for 01:00 min
5	GOTO 3, x39 cycles	GOTO 3, x39 cycles
6	Melt Curve, 65 °C to 95 °C, Increment 0.5 °C for 00:05 min	

3.2.8 RNA sequencing

3.2.8.1 Sample preparation

RNA was extracted as described above and was processed using the TruSeq RNA Sample Preparation v2 Kit (low-throughput protocol; Illumina, San Diego, USA) to prepare the barcoded libraries from 0.5 µg total RNA. Libraries were validated and quantified using DNA 1000 and high-sensitivity chips on a Bioanalyzer (Agilent, Böblingen, Germany); 7.5 pM denatured libraries were used as input into cBot (Illumina, San Diego, USA), followed by deep sequencing using HiSeq 2500 (Illumina, San Diego, USA) for 101 cycles, with an additional seven cycles for index reading.

3.2.8.2 Data analysis

Fastq files were imported into Partek Flow (Partek Incorporated, Missouri, USA). Quality analysis and quality control were performed on all reads to assess read quality and to determine the amount of trimming required (both ends: 13 bases 5´and 1 base 3´). Two samples were excluded from the analysis, since they did not pass the quality control. Trimmed reads were aligned against the hg38 genome using the STAR v2.4.1d aligner. Unaligned reads were further processed using Bowtie 2 v2.2.5 aligner. Aligned reads were combined before quantifying the expression against the ENSEMBL (release 84) database by the Partek Expectation-Maximization algorithm. Finally, statistical gene set analysis was performed using the non-parametric Kruskal Wallis test to determine differential expression at the gene level. Partek flow default settings were used in all analyses.

3.2.8.3 Pathway analysis

Ingenuity pathway analysis (IPA, Qiagen, Hilden, Germany) was conducted using genes with significant differential expression (fold change ±1.5 and p≤0.05). The significance cut-off for IPA was set to p≤0.05 for identification of canonical pathways and upstream regulators. Heatmap visualization and unsupervised hierarchical clustering were performed after normalizing mean expression to 0 with a standard deviation of 1 and using Pearson's dissimilarity algorithm and average linkage in Partek Genomics Suite (Partek Incorporated, Missouri, USA).

3.2.9 Cell lysis, protein extraction and western blot

Cells were lysed and protein was extracted using RIPA Lysis Buffer supplemented with protease and phosphatase inhibitor cocktail. Protein was quantified with the Bradford method using the Protein Assay Dye Reagent Concentrate[134]. Samples were separated by SDS polyacrylamide gel electrophoresis (SDS-PAGE, 30 min at 65 V, followed by 90 min at 130 V) using Novex™ WedgeWell™ 4-12% Tris-Glycine Gels and transferred to Amersham™ Protran™ 0.45 µm nitrocellulose membranes by wet blot (1h at 10 V) using the Mini Gel Tank and Blot Module from Thermo Fisher Scientific. In order to block unspecific binding sites, membranes were incubated with 5% BSA in TBS-T for 1 h at RT. Subsequently, membranes were incubated with primary antibodies diluted in blocking solution overnight at 4 °C. The next day, membranes were washed three times with TBS-T for 5 min at RT and incubated with secondary antibodies diluted in blocking solution for 1 h at RT. Following three washing steps with TBS-T for 5 min at RT, proteins were visualized using the SuperSignal® West Femto Maximum Sensitivity Substrate and detected using the LAS-3000 Imaging System from Fujifilm.

3.2.10 Proteomics profiling

3.2.10.1 Sample preparation

BT-12 and CHLA-266 cells, grown in 6-wells or 10 cm dishes, were either transfected with siPOOLs as described above (see 3.2.5) for 72 h or treated with 30 µM of Ciliobrevin D dissolved in DMSO or DMSO as negative control for 24 h. After transfection or treatment, cells were washed twice with ice cold PBS and cell pellets were collected through centrifugation for 5 min at 800 xg and 4 °C. Proteins were extracted as described previously[135]. Briefly, cells were homogenized in urea buffer with a TissueLyser (Qiagen, Hilden, Germany) and subsequent sonication. After centrifugation for 15 min at 14000 xg and 4 °C, supernatants were collected. Protein concentration was determined via Pierce 660 nm Protein Assay (Thermo Fisher Scientific, Bremen, Germany) and 10 µg protein per sample were desalted through electrophoretic migration at 50 V for 10 min on a 4-12% Bis-Tris polyacrylamide gel. After silver staining, protein bands were cut out reduced, alkylated and digested with trypsin before peptide extraction via sonication. Thus, generated peptide samples were diluted with 0.1% TFA at a ratio of 1:8.

3.2.10.2 LC-MS analysis

For mass spectrometric analysis, 15 µl peptide solution per sample was analyzed on a nano-high-performance liquid chromatography electrospray ionization mass spectrometer. The analytical system was composed of a RSLCnano U3000 HPLC coupled to an Orbitrap Elite or a QExactive plus mass spectrometer via a nano-electrospray ion source (Thermo Fischer Scientific, Bremen, Germany). Injected peptides were concentrated and desalted at a flow rate of 6 µl/min on a trapping column (Acclaim PepMao C18, 2 cm x 100 µm x 3 µm particle size, 100 Å pore size, Thermo Fischer Scientific, Bremen, Germany) with 0.1% TFA for 10 min. Subsequently, peptides were separated at a constant flowrate of 300 nl/min over a 120 min gradient on an analytical column (Acclaim PepMap RSLC C18, 25 cm x 75 µm x 2 µm particle size, 100 Å pore size, Thermo Fischer Scientific, Bremen, Germany) at 60 °C. Separation was achieved through

a gradient from 4 to 40% solvent B (solvent A: 0.1% (v/v) formic acid in water, solvent B: 0.1% (v/v) formic acid, 84% (v/v) acetonitrile in water). Afterwards, peptides were ionized at a voltage of 1400 V and introduced into the mass spectrometer operated in positive mode. On the Orbitrap Elite, MS scans were recorded in profile mode in a range from 350-1700 m/z at a resolution of 60000 while tandem mass spectra were recorded in the ion trap at normal scan rate. Tandem mass spectra were recorded with a data dependent Top20 method and 35% normalized collision energy. Dynamic exclusion was activated with a repeat count of 1 for 45 s and only charge states 2+ and 3+ were analyzed. MS scans on the QExactive plus were recorded in profile mode in a range from 350-2000 m/z at a resolution of 70000, while tandem mass spectra were recorded at a resolution of 17500. Tandem mass spectra were recorded with a data dependent Top10 method and 30% normalized collision energy. Dynamic exclusion was activated with a repeat count of 1 for 100 ms.

3.2.10.3 Computational mass spectrometric data analysis

Proteome Discoverer (version 2.3.0.523, Thermo Fisher Scientific, Bremen, Germany) was applied for peptide/protein identification with Mascot and MS Amanda as search engines employing the UniProt database (human; including isoforms; date 2019-05-29). A false discovery rate of 1% ($p \leq 0.01$) on peptide level was set as identification threshold. Proteins were quantified with Progenesis QI for Proteomics (Version 2.0, Nonlinear Dynamics, Waters Corporation, Newcastle upon Tyne, UK).

3.2.11 Cell proliferation

For the analysis of cell proliferation, either stably transduced or parental BT-12 ($1x10^4$ cells/well) and CHLA-266 ($2x10^4$ cells/well) cells were seeded on 8-well glass slides (Nunc™ Lab-Tek™ II Chamber Slide™ System). The next day, parental cells were either transfected using siPOOLs as described above (see 3.2.5) or treated with 30 µM of Ciliobrevin D dissolved in DMSO or DMSO as negative control. After 72 or 24 h, cell

proliferation was determined using the Click-iT® EdU Alexa Fluor® 488 Imaging Kit according to the manufacturer's instructions and analyzed using the Axio Observer.Z1 with a 40x oil objective and the ApoTome.2 from Zeiss. For the quantification of proliferating cells, at least three randomly selected microscopic fields per 8-well were examined. The percentage of proliferating cells was calculated by counting the number of DAPI-labeled cells and the number of EdU-labeled cells and taking its ratio afterwards.

3.2.12 Clonogenicity

For the analysis of self-renewal capacity, clonogenicity was analyzed.

In case of siRNA-mediated transfection, parental BT-12 ($2.5x10^5$ cells/well) and CHLA-266 ($5x10^5$ cells/well) cells were seeded on 6-well plates. The next day, cells were transfected with siPOOLs as described above (see 3.2.5). After 48 h, transfected BT-12 (100 cells/dish) and CHLA-266 (500 cells/dish) cells were harvested and seeded on 10 cm dishes.

In case of lentiviral transduction, stably transduced BT-12 (100 cells/well) and CHLA-266 (500 cells/well) cells were seeded on 10 cm dishes.

In case of Ciliobrevin D treatment, parental BT-12 (100 cells/well) and CHLA-266 (500 cells/well) cells were seeded on 10 cm dishes. The next day, cells were treated with 30 µM of Ciliobrevin D dissolved in DMSO or DMSO as negative control. After 24 h, medium containing Ciliobrevin D or DMSO was replaced with fresh medium.

Every seven days, some additional medium was added. After 17 (BT-12) or 24 (CHLA-266) days, cells were washed with PBS, fixed with 10% formaldehyde for 30 min at RT and stained with 0.1% crystal violet for 1 h at RT. Following, cells were washed with ddH_2O and number of colonies was counted and quantified.

3.2.13 Cell cycle

For the analysis of the cell cycle, PI staining was performed. For this, either stably transduced or parental BT-12 ($1.25x10^5$ cells/well) and CHLA-266 ($2.5x10^5$ cells/well) cells were seeded on 12-well plates. The next day, parental cells were either transfected using siPOOLs as described above (see 3.2.5) or treated with 30 µM of Ciliobrevin D dissolved in DMSO or DMSO as negative control. After 72 or 24 h, cells were harvested and fixed by resuspending the cell pellet in 100 µl PBS, followed by the addition of 900 µl ice cold EtOH (70%) and subsequent vortexing. Cells were fixed for at least 30 min at 4 °C or stored at -20 °C. After centrifugation for 5 min at 500 xg and 4 °C, cells were washed with PBS and centrifuged again for 5 min at 500 xg and 4 °C. Following, cell pellet was resuspended in 50 µl RNase A (0.1 mg/ml), followed by the addition of 150 µl PI (50 µg/ml). Cells were stained overnight at 4 °C. The next day, cells were analyzed using the CytoFLEX from Beckman Coulter.

3.2.14 Annexin V

For the analysis of apoptosis, Annexin V staining was performed. For this, either stably transduced or parental BT-12 ($1.25x10^5$ cells/well) and CHLA-266 ($2.5x10^5$ cells/well) cells were seeded on 12-well plates. The next day, parental cells were either transfected using siPOOLs as described above (see 3.2.5) or treated with 30 µM of Ciliobrevin D dissolved in DMSO or DMSO as negative control. After 72 or 24 h, cells were stained with FITC Annexin V and PI according to the manufacturer's instructions and analyzed using the CytoFLEX from Beckman Coulter.

3.2.15 Dose-dependent response to Ciliobrevin D

For the analysis of the dose-dependent response to Ciliobrevin D (Calbiochem, Darmstadt, Germany, #250401), BT-12 ($1.5x10^3$ cells/well) and CHLA-266 ($4x10^3$ cells/well) cells were seeded on white 384-well plates in complete medium. The next

day, complete medium was replaced either with complete medium again or with medium lacking serum. Following, Ciliobrevin D dissolved in DMSO was added in a concentration gradient (0.005 µM - 100 µM) in a randomized manner using the D300(e) Digital Dispenser from Tecan. The DMSO concentration was normalized to 0.25% in each well. After 72 h, cell viability was analyzed.

3.2.16 Cell viability

Cell viability was determined using the CellTiter-Glo® Luminescent Cell Viability Assay according to the manufacturer's instructions. The CellTiter-Glo® Reagent was diluted with PBS (1:2, v/v).

3.2.17 *Drosophila melanogaster* experiments

The *in vivo Drosophila melanogaster* (*Drosophila*) experiments were performed by Dr. Astrid Jeibmann, Isabel Tegeder, Katharina Thiel and Johannes Berlandi in the laboratory of Prof. Dr. Martin Hasselblatt, Institute of Neuropathology, University Hospital Münster, Münster, Germany.

Fly husbandry: All strains were raised on corn meal yeast agar and kept at 25 °C and 60% humidity. The following fly strains were used:

$$\frac{repo-GAL4,UAS-mCD8GFP}{repo-GAL4,UAS-mCD8GFP};\frac{repo-GAL4,UAS-mCD8GFP}{TM6\ B}$$

(provided by Prof. Dr. Christian Klämbt, Institute of Neurobiology, University Münster, Münster, Germany).

$$\frac{+}{+};\frac{TM2}{tubulin-GAL80,TM6,Tb}$$

(provided by Harvard *Drosophila* Stock Collection, Boston, USA)

$$\frac{UAS-Snr1-RNAi}{UAS-Snr1-RNAi};\frac{+}{+}$$

(all RNA_i lines provided by Vienna *Drosophila* Resource Center, Vienna, Austria).

Genetic modifier screen: Cell type-specific knockdown of *Snf5-related 1 (Snr1)* expression in glial cells was achieved by using the *repo-GAL4* driver and *UAS-Snr1-RNA$_i$,* respectively. In order to establish a stable *Snr1* screening strain, transcriptional inhibitor *tubulin-GAL80* was used.

$$\frac{+}{+}; \frac{repo-GAL4,UAS-mCD8GFP,UAS-Snr1-RNAi}{repo-GAL4,UAS-mCD8GFP,UAS-Snr1-RNAi}; \frac{repo-GAL4,UAS-mCD8GFP,}{tubulin-Gal80,TM6,Tb}$$

A genetic modifier screen was conducted by crossing the screening strain (decreased *Snr1* expression in glial cells) to RNA_i lines targeting a total of 59 cilia-associated *Drosophila* genes (Supplementary table 1). Candidate genes for the modifier screen had been chosen based on a flybase (http://flybase.org) search for cilia-associated genes having at least one human orthologue. Double knockdown of *Snr1* and the candidate genes was examined for the potential to mitigate deleterious effects of decreased *Snr1* and to rescue pupal lethality (positive shift). The shifting rates for animals affected by double knockdown were scored by counting the number of empty shells and comparing them with the whole number of pupae. Those candidate genes whose additional knockdown led to a pronounced positive shift (>20% hatching flies) were further validated in triplicate. To control for GAL4 dosage effects, the *Snr1* screening strain was crossed to *UAS-mCherry-RNA$_i$*.

3.2.18 Mice experiments

The *in vivo* mice experiments were performed by Rita Cascão (PhD), Eunice Paisana and Carlos Custódia in the laboratory of Cláudia Faria (MD, PhD), Instituto de Medicina Molecular João Lobo Antunes, Faculdade de Medicina da Universidade de Lisboa, Lisbon, Portugal.

Six- to eight-week-old NOD.Cg-Prkdcscid Il2rgtm1Wjl/SzJ (NSG) mice were purchased from Charles River Laboratories France (Lyon, France). All animals were kept in specific pathogen-free (SPF) facilities, randomly housed per groups under standard conditions

(at 20-22 °C under 10 h dark/14 h light), and given free access to food (RM3, SDS Diets, DIETEX, France) and water (decontaminated by reverse osmosis). In accordance with Directive 2010/63/EU (transposed to Portuguese legislation through Decreto-Lei No. 113/2013, of August 7th), all animal procedures were approved by the institutional animal welfare body (ORBEA-iMM), in order to ensure that the use of animals complies with all applicable legislation and follows the 3R's principle, and licensed by the Portuguese competent authority (Direcção Geral de Alimentação e Veterinária, license number: 012028\2016). Humane endpoints were established for 10% body weight loss, paralysis and neurological impairment. Before any invasive procedure, mice were anesthetized using a mixture of 75mg/kg BW Ketamine and 1mg/kg BW Medetomidine. Mice were injected intracranially with BT-12 cells (250000 cells/3µL, per mouse) in the right hemisphere of the frontal cortex. All mice were monitored for body weight, discomfort and distress every other day. Once any of the aforementioned humane endpoints was reached, the mice were euthanized using anesthetic overdose with sodium pentobarbital, and the central neural system was collected for histopathologic analysis.

3.2.19 Drug screening

3.2.19.1 Preparation of clinical library plates

For the clinical library screen, inhibitors were dispensed in 9 dilution steps (0.005 µM - 25 µM, logarithmic distribution) using the D300(e) Digital Dispenser from Tecan and the DMSO concentration was normalized to 0.25% in each well. The inhibitors were dispensed in a randomized manner into white 384-well plates. The outer two rows and columns were omitted for inhibitor distribution to avoid additional evaporation-based plate effects. Finally, assay plates were sealed with parafilm and stored at -80 °C.

The compounds in this library comprise clinically well-established chemotherapeutic agents, including alkylating agents, anthracyclines, cytoskeletal disruptors (taxanes), platinum-based agents and nucleotide analogues. Besides, the compounds in this library

effect most of the cancer-related targets, including various receptors and kinases and the epigenome (the complete description of the clinical compound library is shown in Supplementary table 2).

3.2.19.2 Screening of cell lines with the clinical library

One hour before addition of the prepared cell suspension, the assay plates were removed from -80 °C and thawed at RT. Seeding of cell suspension into the plates was carried out using the Multidrop Combi Reagent Dispenser from Thermo Fisher Scientific. For each cell line, the optimal seeding number per well was determined beforehand to ensure exponential growth during the exposure to the inhibitors for 72 h. The determination of the optimal cell seeding number was performed using a serial cell number dilution between 500 and 10000 cells/well in clear 384-well plates. After 72 hours, the optimal cell number was microscopically determined (70-80% confluence). For BT-12 and CHLA-266 cells, an optimal cell number of 1500 cells/well and 4000 cells/well was assessed, respectively. The final assay volume was 30 µl per well.

3.2.19.3 Cell viability

Cell viability was analyzed as described above (see 3.2.16).

3.2.20 Statistical analyses

Statistical analyses were performed using GraphPad Prism 5.03 (GraphPad Software, San Diego, USA). All data are presented as mean ±SEM of at least three independent experiments, unless stated otherwise. Comparisons between groups were made employing student´s t-test or ANOVA as appropriate. p-values ≤0.05 were considered significant.

Dose-response curves were generated using Python (Python Software Foundation, Wilmington, USA). The data was fitted to:

$y(x) = \frac{\mathrm{a-d}}{1+\left(\frac{x}{c}\right)^{b}} + d$, where

- $y(0) = a \rightarrow a \dots Top$
- $y(\infty) = d \rightarrow d \dots Bottom$
- $y(c) = \frac{a+d}{2} \rightarrow c \dots IC_{50}$
- $y'(c) = -\frac{a-d}{4c} xb \rightarrow b \dots Steepness$

The data was fitted with four initial IC_{50} guesses (0.1; 1; 10; 100). The relative error between the three fits is computed $\frac{max\{IC_{50}\}-min\{IC_{50}\}}{mean\{IC_{50}\}}$. If the fit is stable, the relative error shall be small (less than 0.5%).

4 Results

4.1 Detection of primary cilia in AT/RT patient samples and cell lines

4.1.1 Description of the cohort of AT/RT patient samples

In this thesis, tumor tissue sections from 13 AT/RT patients were examined. These were kindly provided by Prof. Dr. Martin Hasselblatt from the Institute of Neuropathology at the University Hospital in Münster, Germany, and divided into subgroups using 450k methylation array profiling at the German Cancer Research Center in Heidelberg, Germany. Overall, the AT/RT patient samples investigated in this thesis included six AT/RT-TYR, four AT/RT-MYC and three AT/RT-SHH tumors (Table 21). Within this cohort, AT/RT-TYR tumors presented both infratentorially and supratentorially, while AT/RT-MYC tumors were more common in supratentorial regions. AT/RT-SHH tumors, though, exclusively occurred in the supratentorial compartment (Table 21). AT/RT-TYR and AT/RT-SHH tumors were more common in male patients, while AT/RT-MYC tumors were prominently present in female patients (Table 21). Concerning the age at diagnosis, AT/RT-TYR and AT/RT-MYC tumors presented both in patients <1 year and in patients >1 year, while AT/RT-SHH tumors exclusively occurred in patients >1 year (Table 21). Regarding the *SMARCB1* status, most of the AT/RT-TYR tumors demonstrated mutations, while all AT/RT-MYC and AT/RT-SHH tumors showed structural variations (Table 21).

Table 21: Description of the cohort of AT/RT patient samples.

ID	Molecular subgroup	Location	Gender	Age at diagnosis (months)	*SMARCB1* status
168	TYR	Supratentorial	Male	12	Structural variation
165	TYR	Infratentorial	Female	19	Mutation
145	TYR	Infratentorial	Male	2	Mutation
79	TYR	Supratentorial	Male	6	Structural variation
112	TYR	Infratentorial	Male	15	Mutation
32	TYR	Supratentorial	Female	10	Mutation
157	MYC	Infratentorial	Male	23	Structural variation
167	MYC	Supratentorial	Female	11	Structural variation
153	MYC	Supratentorial	Female	30	Structural variation
25	MYC	Supratentorial	Female	4	Structural variation
166	SHH	Supratentorial	Female	19	Structural variation
3	SHH	Supratentorial	Male	16	Structural variation
9	SHH	Supratentorial	Male	12	Structural variation

TYR: tyrosinase, SHH: sonic hedgehog

4.1.2 Detection of primary cilia in tumor tissue sections of AT/RT patients

Initially, immunofluorescence was performed to detect primary cilia in the tumor tissue sections of the 13 AT/RT patients. Notably, primary cilia were detected in all the tumor tissue sections of the AT/RT patients investigated in this thesis (a representative immunofluorescence image for an AT/RT-TYR tumor is shown in Figure 5 A). Quantification of the percentage of ciliated cells in each of the AT/RT patient samples revealed that AT/RT-TYR tumors demonstrated the highest percentage of ciliated cells (range 12-22%), while AT/RT-MYC and AT/RT-SHH tumors showed a variable degree (range 4-29%) and the lowest proportion (range 2-6%) of cells with a primary cilium, respectively (Figure 5 B).

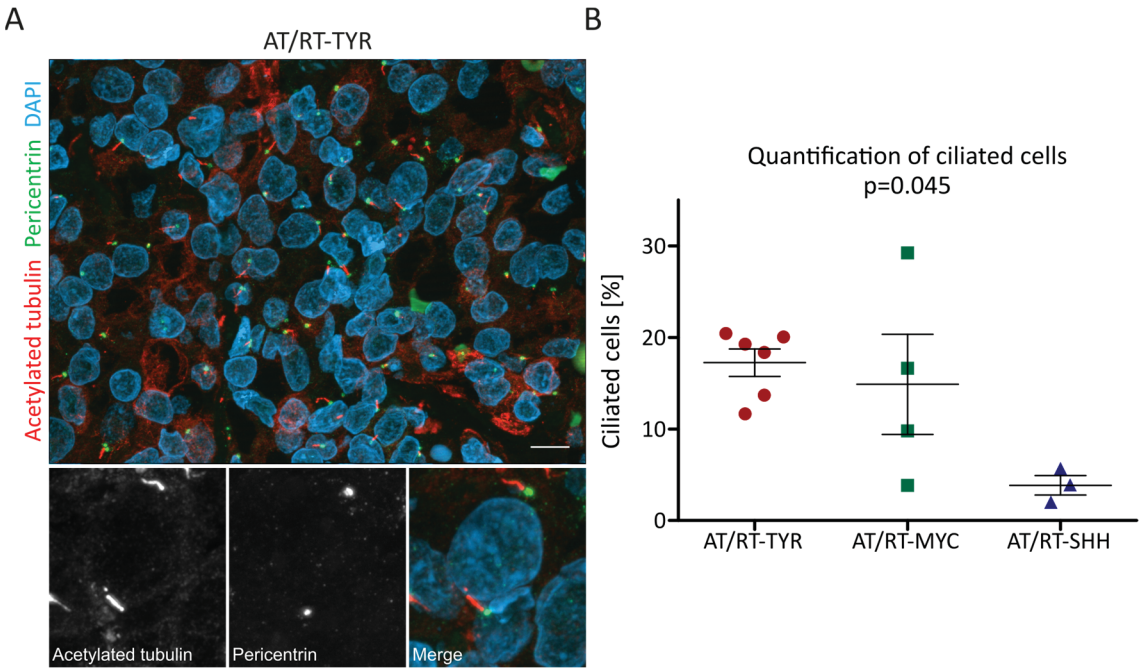

Figure 5: Detection of primary cilia in tumor tissue sections of AT/RT patients. Tumor tissue sections of AT/RT patients were de-paraffined and stained for Pericentrin (green) and Acetylated tubulin (red), detecting the basal body and the axoneme of the primary cilium, respectively. Nuclei were counterstained with 4´,6-diamidin-2-phenylindol (DAPI, blue). Overall, a total of 13 AT/RT patient samples were examined, including six AT/RT-TYR, four AT/RT-MYC and three AT/RT-SHH tumors. A representative immunofluorescence image for an AT/RT-TYR tumor is shown in (A). Quantification of the percentage of ciliated cells in each of the AT/RT patient samples revealed a significant difference across tumor subgroups (B). Statistical analysis was performed using one-way analysis of variance (ANOVA). *p<0.05. The scale bar corresponds to 10 µm.

4.1.3 Detection of primary cilia in AT/RT cell lines

To date, a collection of 14 distinct AT/RT cell lines is available in our laboratory. In order to divide these cell lines into molecular subgroups, RNA sequencing (of 9 AT/RT cell lines) was conducted. Subsequently, the RNA sequencing data were compared to the subgroup-specific signatures of the AT/RT transcriptomes reported for primary tumor samples[61]. Overall, BT-12, BT-16 and CHLA-266 were found to most likely correspond to the TYR subgroup of AT/RT, while CHLA-06 and VU-397 and CHLA-02, CHLA-04, CHLA-05 and HHU-01 were found to most likely correspond to the MYC subgroup and the SHH subgroup of AT/RT, respectively (data not shown).

In order to identify suitable cell line models to investigate the role of primary cilia in AT/RT, not only the subgroup-specific signatures of the AT/RT transcriptomes but also

the expression levels of *kinesin family member 3A (KIF3A)* were considered, since KIF3A is one subunit of the heterotrimeric motor protein kinesin-2 and, thus, is involved in the assembly of primary cilia[67]. Previous studies have shown that disruption of primary ciliogenesis can be achieved by genetic ablation of *KIF3A*[105,106,136,137].

To investigate the expression levels of *KIF3A* in the AT/RT cell lines available in our research group, the above-mentioned RNA sequencing data were consulted. Given the fact that BT-12 and CHLA-266 most likely correspond to the TYR subgroup of AT/RT and also showed the highest expression of *KIF3A* in comparison to all the other AT/RT cell lines (log2 expression of 0.64 (BT-12) and 0.51 (CHLA-266) compared to log2 expression of 0.33 (BT-16), 0.49 (VU-397), 0.37 (CHLA-06), 0.51 (CHLA-04), 0.34 (CHLA-05), 0.30 (CHLA-02) and 0.17 (HHU-01), Figure 6), these cell lines were chosen for further investigation.

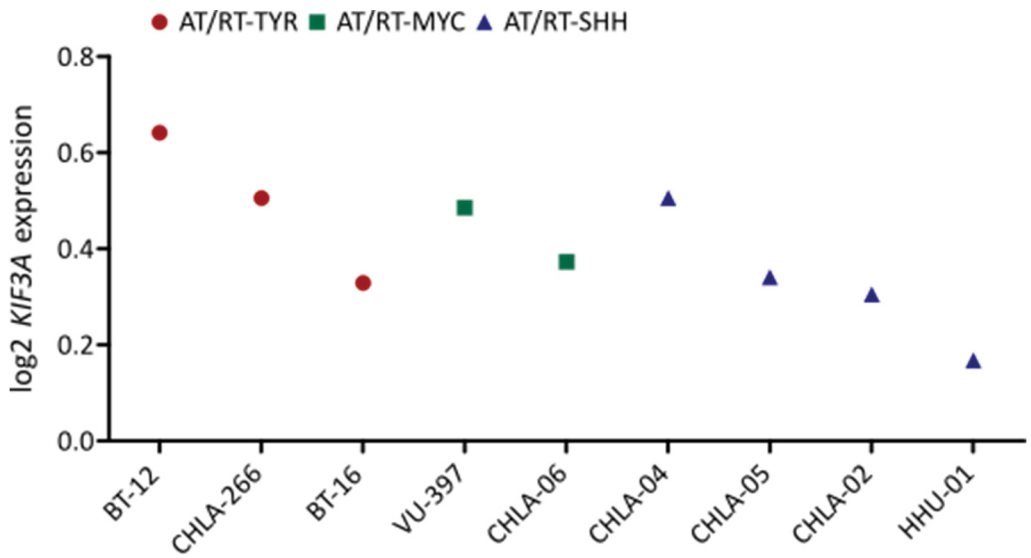

Figure 6: Expression levels of *kinesin family member 3A (KIF3A)* in AT/RT cell lines. *KIF3A* expression levels were derived from RNA sequencing data. Given the highest expression of *KIF3A* in the AT/RT cell lines BT-12 and CHLA-266, these cell lines were chosen for further investigation.

After identifying BT-12 and CHLA-266 as suitable cell line models to investigate the role of primary cilia in AT/RT, immunofluorescence was performed to detect primary cilia in these cell lines. For this, the same immunofluorescence protocol already used for the AT/RT patient samples was employed.

Indeed, primary cilia were detected in BT-12 and CHLA-266 cells (Figure 7 A, B).

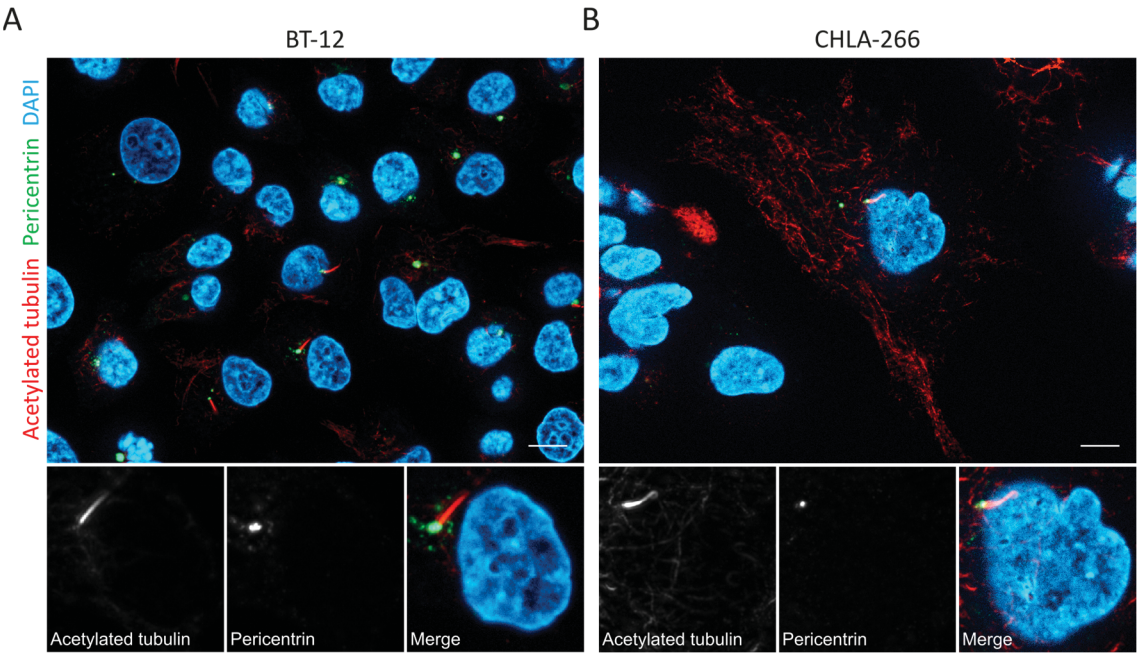

Figure 7: Detection of primary cilia in the AT/RT cell lines BT-12 and CHLA-266. AT/RT cell lines BT-12 (A) and CHLA-266 (B) were fixed and stained for Pericentrin (green) and Acetylated tubulin (red), detecting the basal body and the axoneme of the primary cilium, respectively. Nuclei were counterstained with 4´,6-diamidin-2-phenylindol (DAPI, blue). The scale bar corresponds to 10 µm.

4.1.4 Serum starvation promotes primary ciliogenesis in the AT/RT cell lines BT-12 and CHLA-266

Since serum starvation represents a commonly used method to promote primary ciliogenesis[136,138], it was next investigated if this also applies to the AT/RT cell lines investigated in this thesis.

Quantitative real-time PCR revealed that the expression of *KIF3A* was significantly increased following serum starvation of BT-12 and CHLA-266 cells (1.6- to 1.7-fold increase, Figure 8 A, B). Additionally, a significant increase in the expression of *GLI1*, *PTCH1* and *SMO*, three key SHH signature genes whose respective gene products are localized to the primary cilium, was observed (1.4- to 2.9-fold increase, Figure 8 A, B). Consistent with this, the percentage of ciliated cells was significantly increased following serum starvation (from 9.2% to 23.7% in BT-12 cells and from 9.9% to 21.5% in CHLA-

266 cells, Figure 8 C). Representative immunofluorescence images are shown in Supplementary figure 1.

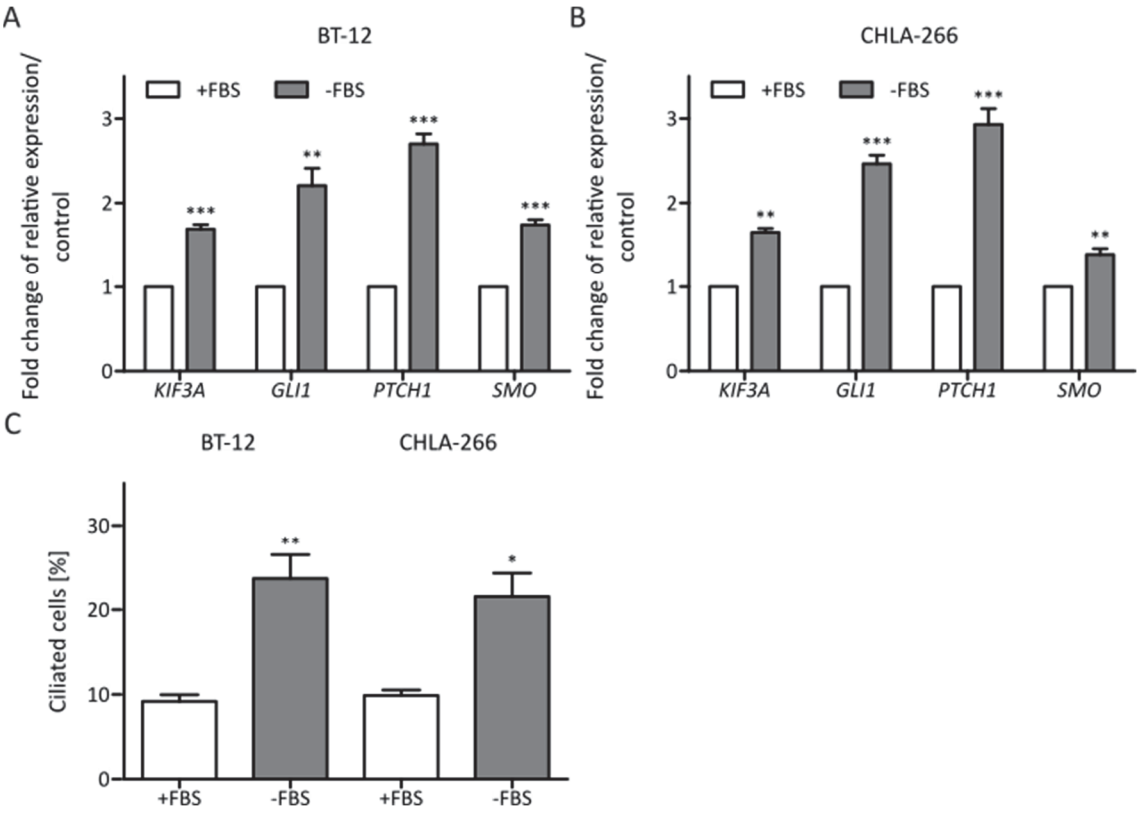

Figure 8: Serum starvation promotes primary ciliogenesis in the AT/RT cell lines BT-12 and CHLA-266. For serum starvation experiments, BT-12 and CHLA-266 cells were seeded in complete medium. The next day, complete medium was replaced either with complete medium again (+fetal bovine serum (FBS)) or with medium lacking serum (-FBS) for 72 h. Quantitative real-time PCR revealed increased expression of *kinesin family member 3A (KIF3A)*, *glioma-associated oncogene 1 (GLI1)*, *patched 1 (PTCH1)* and *smoothened (SMO)* following serum starvation in BT-12 and CHLA-266 cells (A, B). mRNA expression was normalized to the housekeeping genes *glyceraldehyde 3-phosphate dehydrogenase (GAPDH)* and *phosphoglycerate kinase 1 (PGK1)* and calculated relative to +FBS. Immunofluorescence confirmed that serum starvation increases the percentage of ciliated cells in BT-12 and CHLA-266 cells (C). Representative immunofluorescence images are shown in Supplementary figure 1. Values shown represent mean ±SEM of three replicates. *p<0.05; **p<0.01; ***p<0.001 (student´s t-test).

4.2 Functional consequences of knockdown of *kinesin family member 3A* in the AT/RT cell lines BT-12 and CHLA-266

4.2.1 Knockdown of *kinesin family member 3A* disrupts primary ciliogenesis in the AT/RT cell lines BT-12 and CHLA-266

To functionally investigate the role of primary cilia in AT/RT, both siRNA-mediated (transient) and shRNA/CRISPRi-mediated (stable) knockdown of the crucial ciliary marker *KIF3A* was performed in the two AT/RT cell lines investigated in this thesis.

Quantitative real-time PCR revealed that the expression of *KIF3A* mRNA was significantly reduced following both transient and stable knockdown of *KIF3A* in BT-12 and CHLA-266 cells (78% to 88% reduction, Figure 9 A). Western blot analysis confirmed reduced expression of KIF3A protein (Figure 9 B). Consistent with this, immunofluorescence corroborated disruption of primary ciliogenesis, since the formation of primary cilia decreased following both transient and stable knockdown of *KIF3A* in BT-12 and CHLA-266 cells (Figure 9 C). Representative immunofluorescence images are shown in Supplementary figure 2.

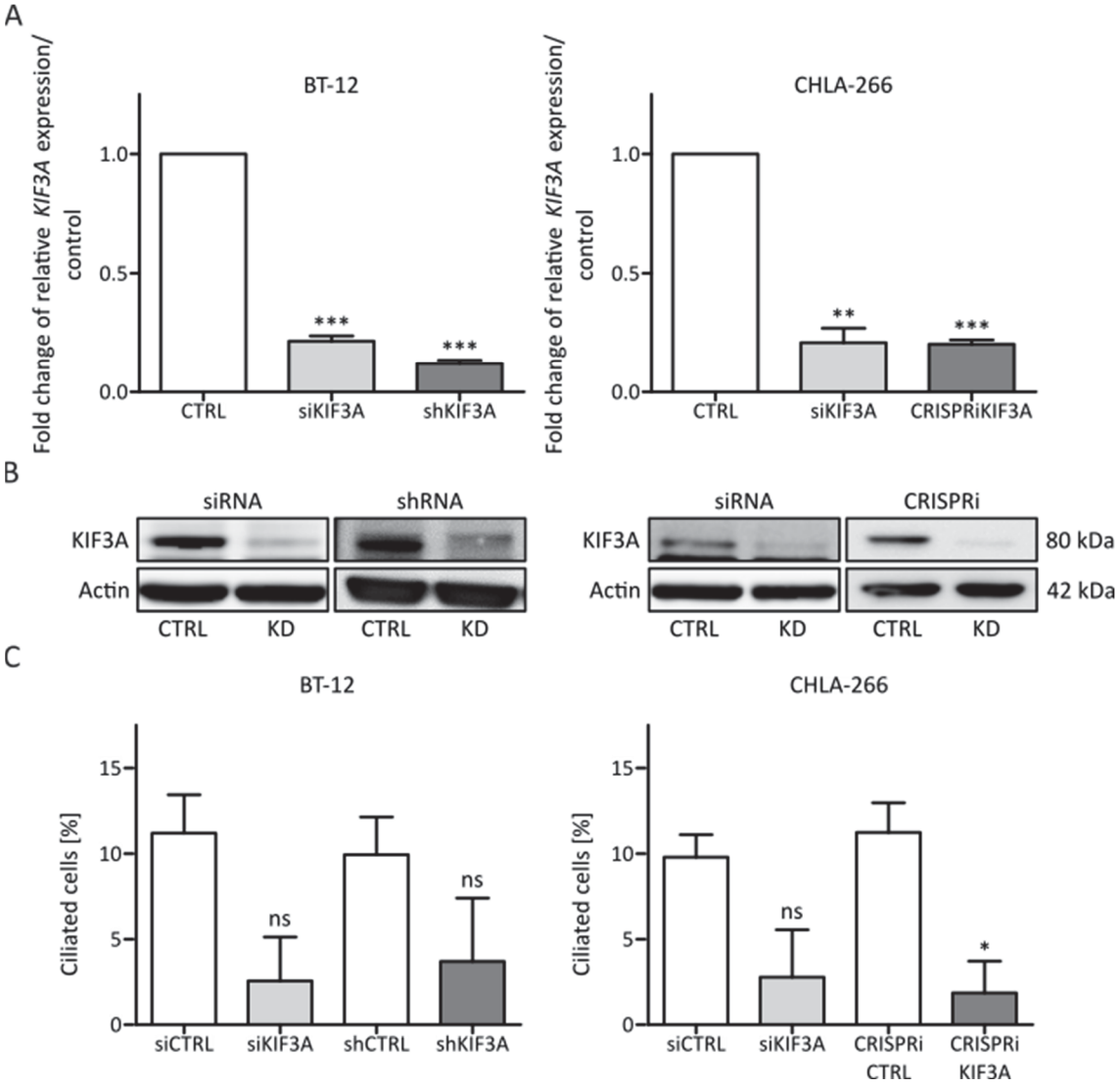

Figure 9: Knockdown of *kinesin family member 3A (KIF3A)* disrupts primary ciliogenesis in the AT/RT cell lines BT-12 and CHLA-266. Transient knockdown of *KIF3A* was achieved using siPOOLs. Stable knockdown of *KIF3A* was achieved using shRNA-based (BT-12) or CRISPRi-based (CHLA-266) technology. (A) mRNA expression was normalized to the housekeeping genes *glyceraldehyde 3-phosphate dehydrogenase (GAPDH)* and *phosphoglycerate kinase 1 (PGK1)* and calculated relative to siCTRL or shCTRL/CRISPRiCTRL. (B) Shown are also representative western blot images for KIF3A and Actin as a loading control following transient and stable *KIF3A* knockdown. (C) Quantification of the percentage of ciliated cells revealed reduction of ciliated cells following *KIF3A* knockdown in BT-12 and CHLA-266 cells. Representative immunofluorescence images are shown in Supplementary figure 2. Values shown represent mean ±SEM of three replicates. Ns: not significant; **p<0.01; ***p<0.001 (student´s t-test).

4.2.2 Knockdown of *kinesin family member 3A* decreases the oncogenic potential of the AT/RT cell lines BT-12 and CHLA-266

Since both transient and stable knockdown of *KIF3A* has been shown to successfully disrupt primary ciliogenesis in the AT/RT cell lines investigated in this thesis, the effect of *KIF3A* knockdown on tumor-associated properties was investigated.

Initially, the effect of transient and stable *KIF3A* knockdown on proliferation was analyzed in BT-12 and CHLA-266 cells. Indeed, a significant reduction in proliferation was observed following both transient and stable *KIF3A* knockdown in both cell lines (43% to 65% reduction, Figure 10 A, B).

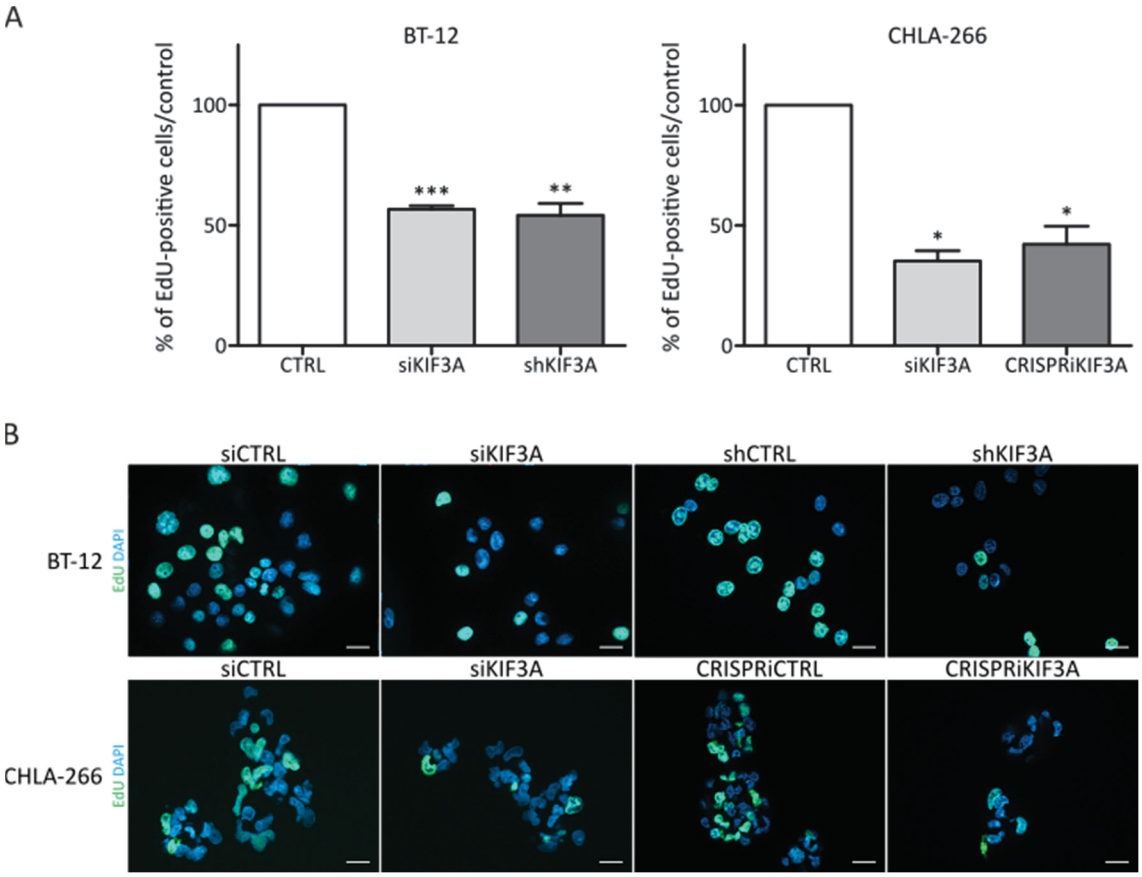

Figure 10: Knockdown of *kinesin family member 3A (KIF3A)* reduces proliferation in the AT/RT cell lines BT-12 and CHLA-266. Transient and stable transfected BT-12 and CHLA-266 cells were incubated with 10 µM EdU (modified thymidine analogue) for 6 h. Following, cells were fixed and EdU was detected using Alexa Fluor™ 488 azide (green). Cells were counterstained with 4´,6-diamidin-2-phenylindol (DAPI, blue). (A) Values shown represent mean ±SEM of three replicates. *p<0.05; **p<0.01; ***p<0.001 (student´s t-test). Shown are also representative immunofluorescence images (B). The scale bar corresponds to 20 µm.

Additionally, the effect of transient and stable *KIF3A* knockdown on clonogenicity was investigated in BT-12 and CHLA-266 cells. In fact, a significant reduction in clonogenicity was observed following both transient and stable *KIF3A* knockdown in both cell lines (46% to 69% reduction, Figure 11 A, B).

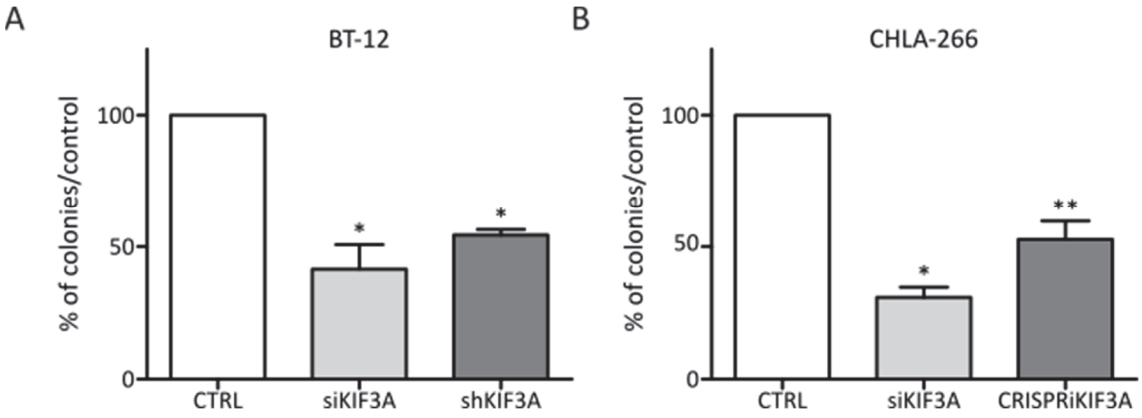

Figure 11: Knockdown of *kinesin family member 3A (KIF3A)* reduces clonogenicity in the AT/RT cell lines BT-12 and CHLA-266. Quantification of colonies formed by transient and stable transfected BT-12 (A) and CHLA-266 (B) cells following plating of 100 (BT-12) or 500 (CHLA-266) cells per 10 cm dish and 17 (BT-12) or 24 (CHLA-266) days of incubation. Values shown represent mean ±SEM of three replicates. *p<0.05; **p<0.01 (student´s t-test).

Furthermore, the effect of transient *KIF3A* knockdown on the cell cycle state was analyzed in BT-12 and CHLA-266 cells. Cell cycle analysis revealed a significant decrease in the G2M fraction of cells, concomitant with a significant increase in the sub G1 fraction of cells (Figure 12 A, B), suggesting an increase in apoptotic cells following transient *KIF3A* knockdown in both cell lines.

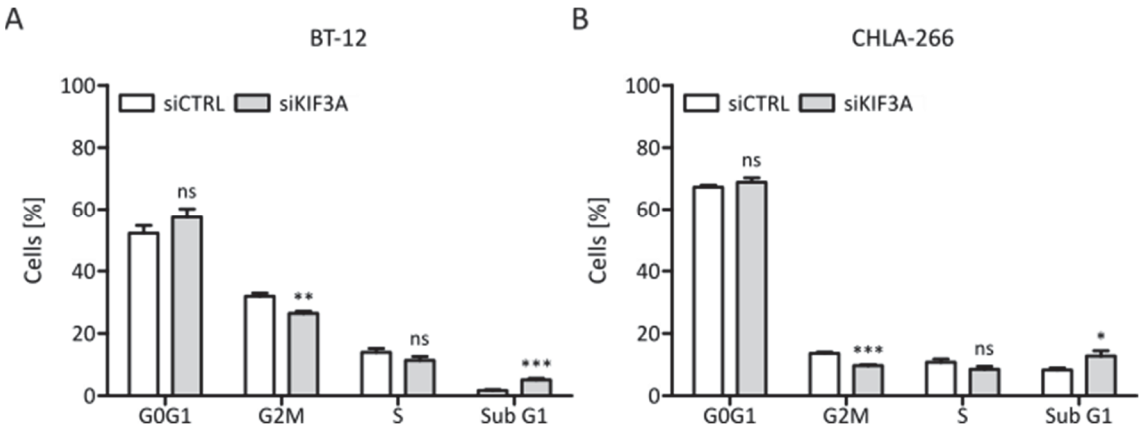

Figure 12: Knockdown of *kinesin family member 3A (KIF3A)* results in sub G1 arrest in the AT/RT cell lines BT-12 and CHLA-266. Cell cycle profiles of transient transfected BT-12 (A) and CHLA-266 (B) cells. Cells were fixed and stained with propidium iodide (PI). DNA content was analyzed using flow cytometry. Values shown represent mean ±SEM of three replicates. Ns: not significant; *p<0.05; **p<0.01; ***p<0.001 (student´s t-test).

To confirm this hypothesis, the effect of transient and stable *KIF3A* knockdown on apoptosis was investigated in BT-12 and CHLA-266 cells. In line with the cell cycle analysis, a significant increase in apoptotic cells (Annexin V+PI- and Annexin V+PI+) was observed following both transient and stable knockdown of *KIF3A* in both cell lines (1.3- to 3.9-fold increase, Figure 13 A, B).

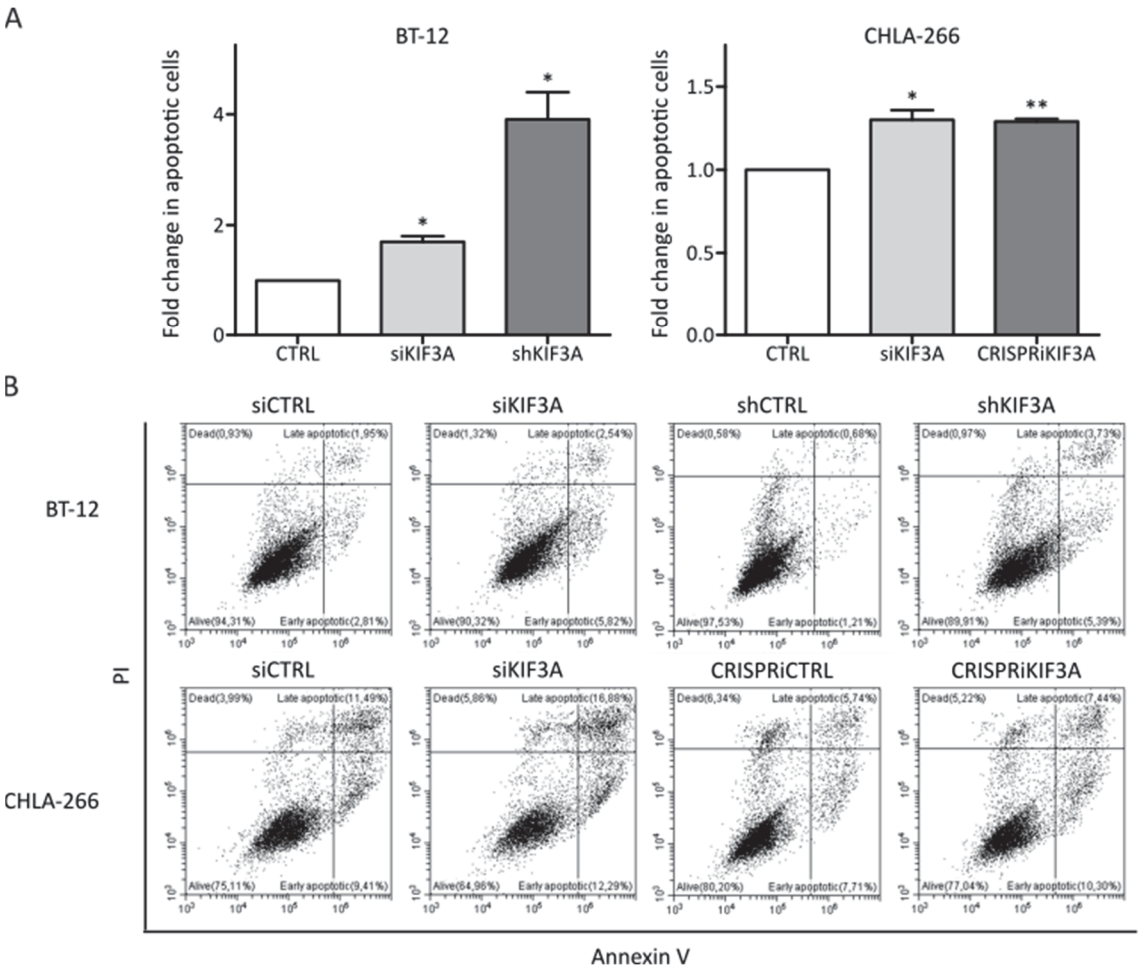

Figure 13: Knockdown of *kinesin family member 3A (KIF3A)* increases apoptosis in the AT/RT cell lines BT-12 and CHLA-266. To assess cells undergoing apoptosis, cells were stained with Annexin V and propidium iodide (PI) and analyzed using flow cytometry. (A) Shown are bar graphs representing the fold change in apoptotic cells following transient and stable knockdown of *KIF3A* in the AT/RT cell lines BT-12 and CHLA-266. Values shown represent mean ±SEM of three replicates. *p<0.05; **p<0.01 (student´s t-test). Shown are also representative flow cytometry plots (B).

4.2.3 Ciliobrevin D treatment phenocopies *kinesin family member 3A* knockdown in the AT/RT cell lines BT-12 and CHLA-266

To functionally validate the anti-tumoral effect following *KIF3A* knockdown in the AT/RT cell lines investigated in this thesis, Ciliobrevin D treatment was employed.

Ciliobrevin D is a cell-permeable benzoyl dihydroquinazolinone derivative (the chemical structure of Ciliobrevin D is shown in Figure 14) that acts as a reversible and specific blocker of AAA+ ATPase motor cytoplasmic dynein. In addition, Ciliobrevin D has been

shown to perturb protein trafficking within the primary cilium and to block SHH signaling[139].

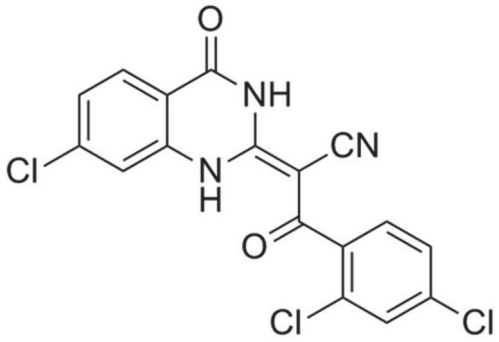

Figure 14: Chemical structure of Ciliobrevin D. The empirical formula of Ciliobrevin D is $C_{17}H_8Cl_3N_3O_2$ (Calbiochem, Darmstadt, Germany).

Initially, the effect of Ciliobrevin D on cell viability was analyzed in a dose-dependent manner in BT-12 and CHLA-266 cells. Interestingly, BT-12 and CHLA-266 cells showed just little response to Ciliobrevin D when treated in complete medium (+FBS, Figure 15 A, B). However, when treated in medium lacking serum (-FBS), BT-12 and CHLA-266 cells did respond to Ciliobrevin D, with half maximal inhibitory concentrations (IC_{50}s) reaching 19.2 µM in BT-12 cells and 10.7 µM in CHLA-266 cells (Figure 15 A, B).

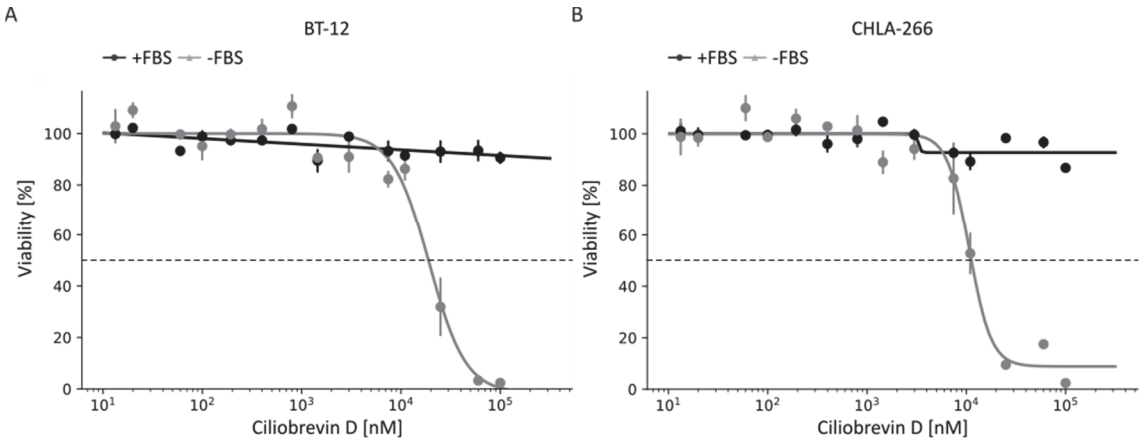

Figure 15: Ciliobrevin D response curves in the AT/RT cell lines BT-12 and CHLA-266. For the analysis of the dose-dependent response to Ciliobrevin D, BT-12 and CHLA-266 cells were seeded on white 384-well plates in complete medium. The next day, complete medium was replaced either with complete medium again (+fetal bovine serum (FBS)) or with medium lacking serum (-FBS). Following, Ciliobrevin D dissolved in dimethylsulfoxide (DMSO) was added in a concentration gradient (0.005 µM - 100 µM) in a randomized manner using the D300(e) Digital Dispenser from Tecan. The DMSO concentration was normalized to 0.25% in each well. After 72 h, cell viability was analyzed. Values shown represent mean ±SEM of three replicates.

Due to the results shown in Figure 15, the following experiments were performed under serum starvation conditions. At first, the effect of Ciliobrevin D on primary ciliogenesis was investigated in BT-12 and CHLA-266 cells. Quantitative real-time PCR revealed that the expression of *KIF3A* was significantly reduced following Ciliobrevin D treatment in BT-12 and CHLA-266 cells (41% to 71% reduction, Figure 16 A, B). Besides, a significant reduction in the expression of *GLI1*, *PTCH1* and *SMO* was observed (37% to 87% reduction, Figure 16 A, B). Consistent with this, Ciliobrevin D treatment disrupted primary ciliogenesis, since immunofluorescence confirmed complete loss of ciliated cells following Ciliobrevin D treatment (Figure 16 C). Representative immunofluorescence images are shown in Supplementary figure 3.

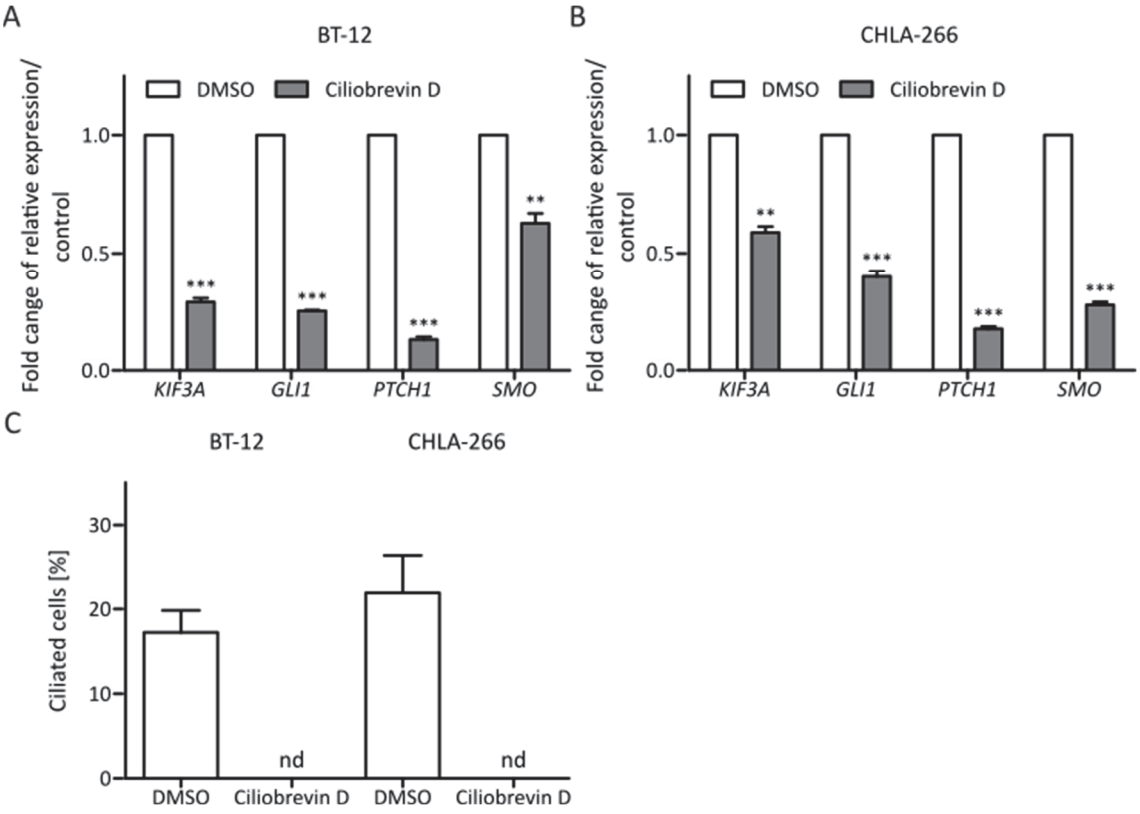

Figure 16: Ciliobrevin D treatment disrupts primary ciliogenesis in the AT/RT cell lines BT-12 and CHLA-266. BT-12 and CHLA-266 cells were seeded in complete medium. The next day, complete medium was replaced with medium lacking serum and the cells were treated with 30 µM of Ciliobrevin D or dimethylsulfoxide (DMSO) as a negative control. Quantitative real-time PCR revealed reduced expression of *kinesin family member 3A (KIF3A), glioma-associated oncogene 1 (GLI1), patched 1 (PTCH1) and smoothened (SMO)* following Ciliobrevin D treatment in BT-12 and CHLA-266 cells (A, B). mRNA expression was normalized to the housekeeping genes *glyceraldehyde 3-phosphate dehydrogenase (GAPDH)* and *phosphoglycerate kinase 1 (PGK1)* and calculated relative to +FBS. Immunofluorescence confirmed complete loss of ciliated cells in BT-12 and CHLA-266 cells (C). Representative immunofluorescence images are shown in Supplementary figure 3. Values shown represent mean ±SEM of three replicates. N.d.: not detected; **p<0.01; ***p<0.001 (student´s t-test).

Besides, the effect of Ciliobrevin D on proliferation was analyzed in BT-12 and CHLA-266 cells. Notably, Ciliobrevin D treatment completely blocked proliferation in both cell lines (Figure 17 A, B).

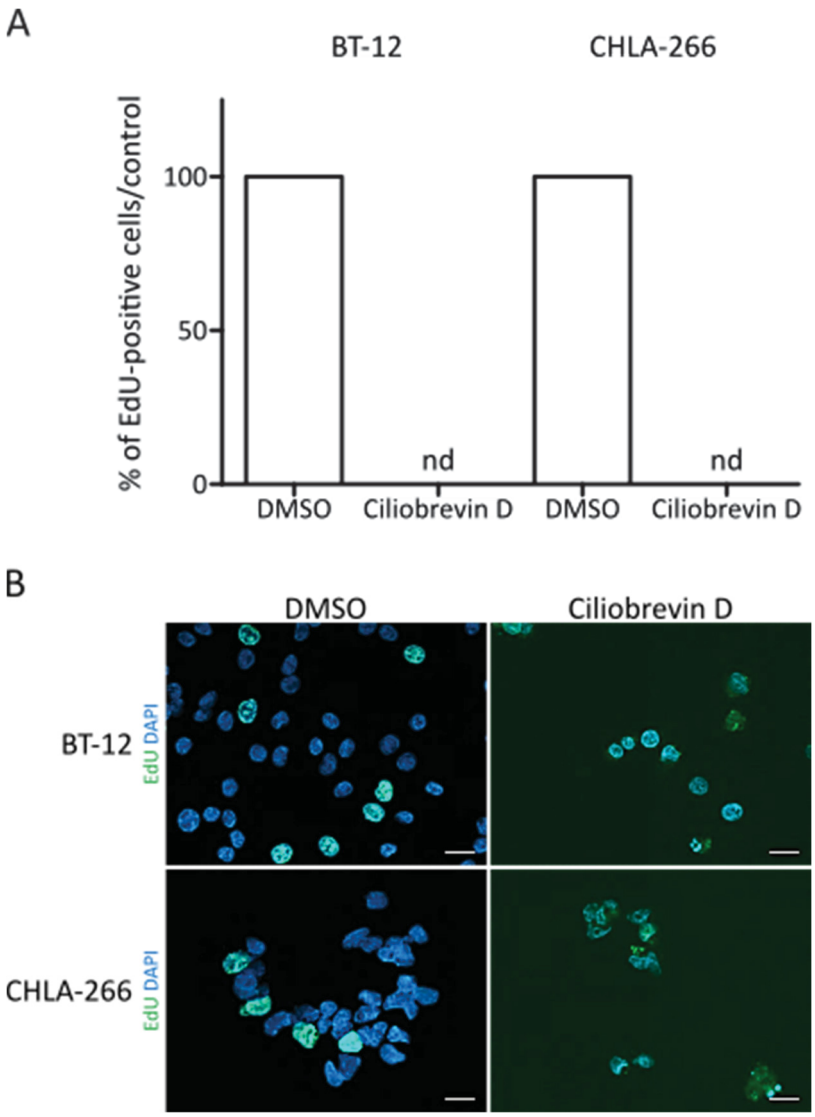

Figure 17: Ciliobrevin D treatment blocks proliferation in the AT/RT cell lines BT-12 and CHLA-266. Ciliobrevin D treated BT-12 and CHLA-266 cells were incubated with 10 µM EdU for 6 h. Following, cells were fixed and EdU (modified thymidine analogue) was detected using Alexa Fluor™ 488 azide (green). Cells were counterstained with 4´,6-diamidin-2-phenylindol (DAPI, blue). (A) Values shown represent mean ±SEM of three replicates. Nd: not detected. Shown are also representative immunofluorescence images (B). The scale bar corresponds to 20 µm.

Additionally, the effect of Ciliobrevin D on clonogenicity was investigated in BT-12 and CHLA-266 cells. A significant reduction in clonogenicity was observed following Ciliobrevin D treatment in both cell lines (50% to 51% reduction, Figure 18 A, B).

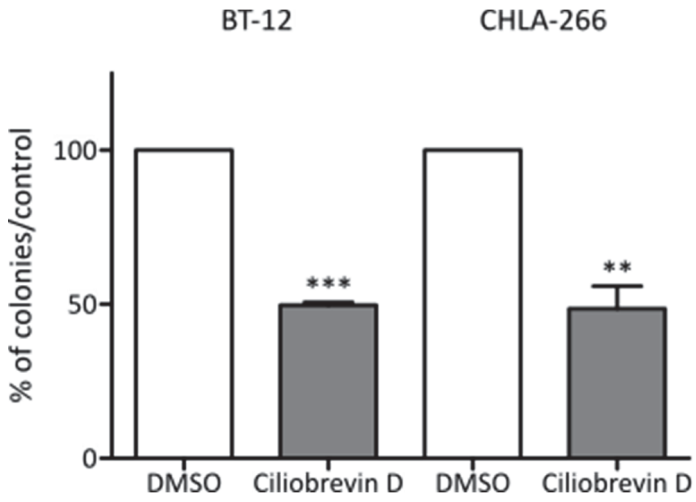

Figure 18: Ciliobrevin D treatment reduces clonogenicity in the AT/RT cell lines BT-12 and CHLA-266. Quantification of colonies formed by Ciliobrevin D treated BT-12 (A) and CHLA-266 (B) cells following plating of 100 (BT-12) or 500 (CHLA-266) cells per 10 cm dish and 17 (BT-12) or 24 (CHLA-266) days of incubation. Values shown represent mean ±SEM of three replicates. *p<0.05; **p<0.01 (student´s t-test).

Furthermore, the effect of Ciliobrevin D on the cell cycle state was analyzed in BT-12 and CHLA-266 cells. Cell cycle analysis revealed a significant decrease in the GOG1 and S fraction of cells, concomitant with a significant increase in the G2M and sub G1 fraction of cells (Figure 19 A, B), suggesting an increase in apoptotic cells following Ciliobrevin D treatment in both cell lines.

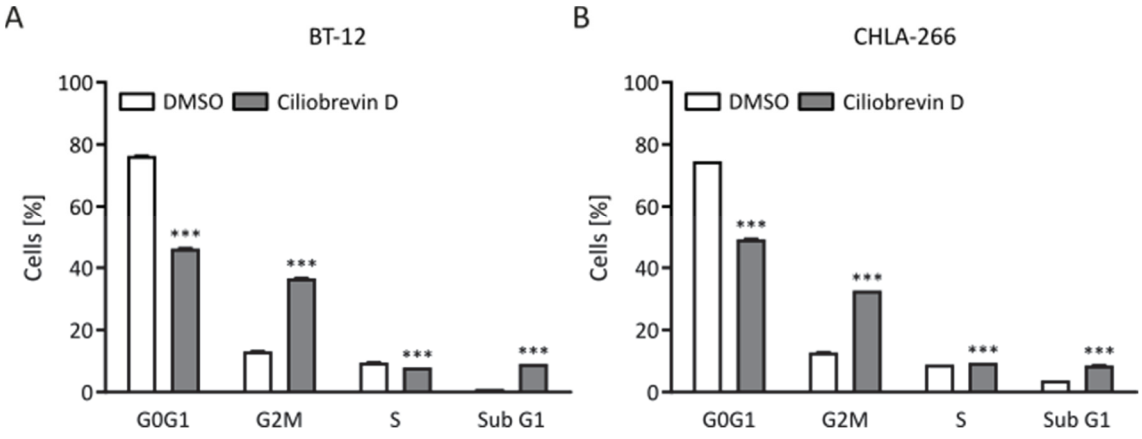

Figure 19: Ciliobrevin D treatment results in sub G1 arrest in the AT/RT cell lines BT-12 and CHLA-266. Cell cycle profiles of Ciliobrevin D treated BT-12 (A) and CHLA-266 (B) cells. Cells were fixed and stained with propidium iodide (PI). DNA content was analyzed using flow cytometry. Values shown represent mean ±SEM of three replicates. ***p<0.001 (student´s t-test).

To confirm this hypothesis, the effect of Ciliobrevin D on apoptosis was investigated in BT-12 and CHLA-266 cells. In line with the cell cycle analysis, a significant increase in apoptotic cells (Annexin V+PI- and Annexin V+PI+) was observed following Ciliobrevin D treatment in both cell lines (4- to 18-fold increase, Figure 20 A, B).

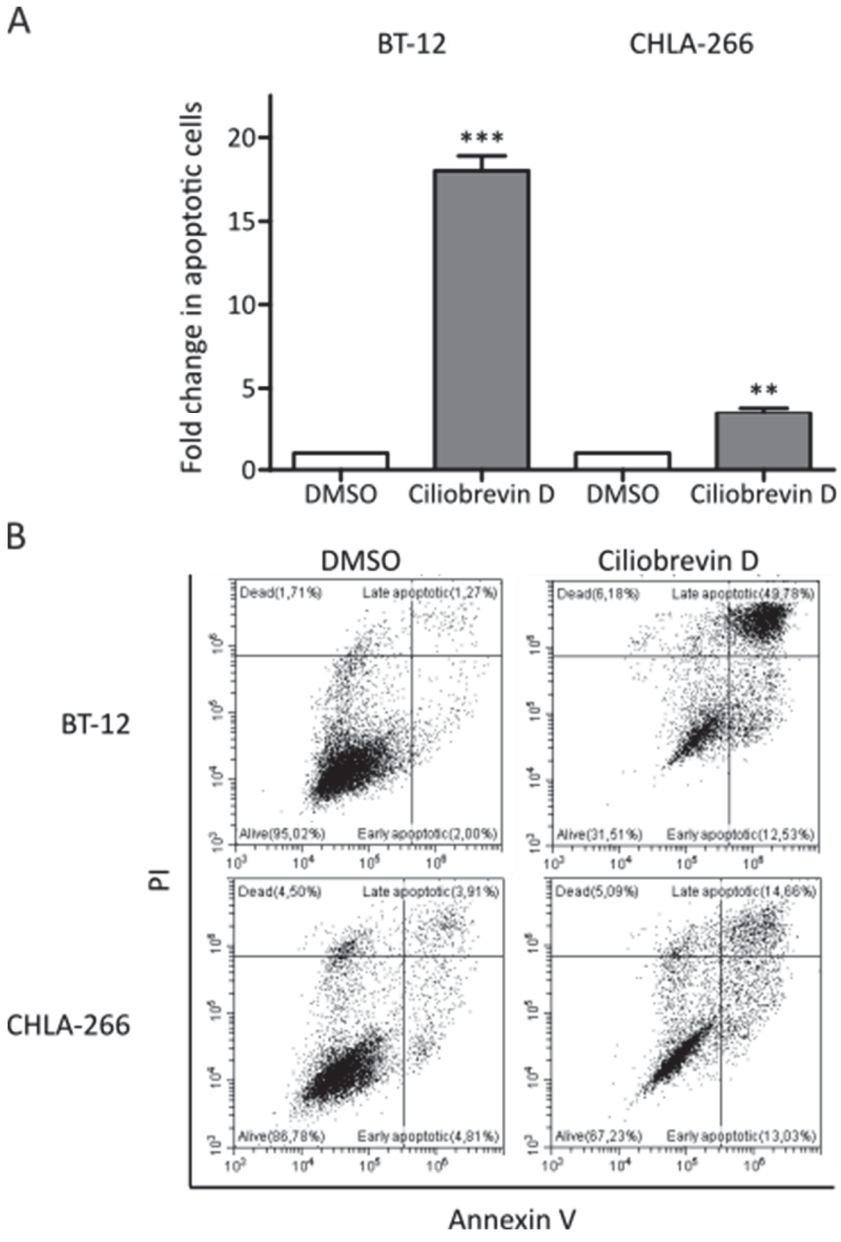

Figure 20: Ciliobrevin D treatment increases apoptosis in the AT/RT cell lines BT-12 and CHLA-266. To assess cells undergoing apoptosis, cells were stained with Annexin V and propidium iodide (PI) and analyzed using flow cytometry. (A) Shown are bar graphs representing the fold change in apoptotic cells following treatment with 30 µM of Ciliobrevin D for 24 h or DMSO as a control in the AT/RT cell lines BT-12 and CHLA-266. Values shown represent mean ±SEM of three replicates. **p<0.01; ***p<0.001 (student´s t-test). Shown are also representative flow cytometry plots.

4.3 Proteogenomic profiling reveals induction of interferon signaling following *kinesin family member 3A* knockdown in the AT/RT cell lines BT-12 and CHLA-266

4.3.1 Assessment of transcriptomic changes following *kinesin family member 3A* knockdown in the AT/RT cell lines BT-12 and CHLA-266

In order to elucidate the biological mechanism that is responsible for the anti-tumoral effect following *KIF3A* knockdown, siRNA-mediated knockdown of *KIF3A* was performed in the AT/RT cell lines BT-12 and CHLA-266. Following knockdown, global transcriptional perturbations were determined using RNA sequencing.

Using a minimal fold change of ±1.5 and a significance level of $p \leq 0.05$ as a cut-off, a total of 507 and 1861 differentially expressed genes were identified in BT-12 and CHLA-266 cells, respectively (Figure 21 A, B). Amongst these, a total of 70 genes were differentially expressed following *KIF3A* knockdown in both BT-12 and CHLA-266 cells (Figure 21 C).

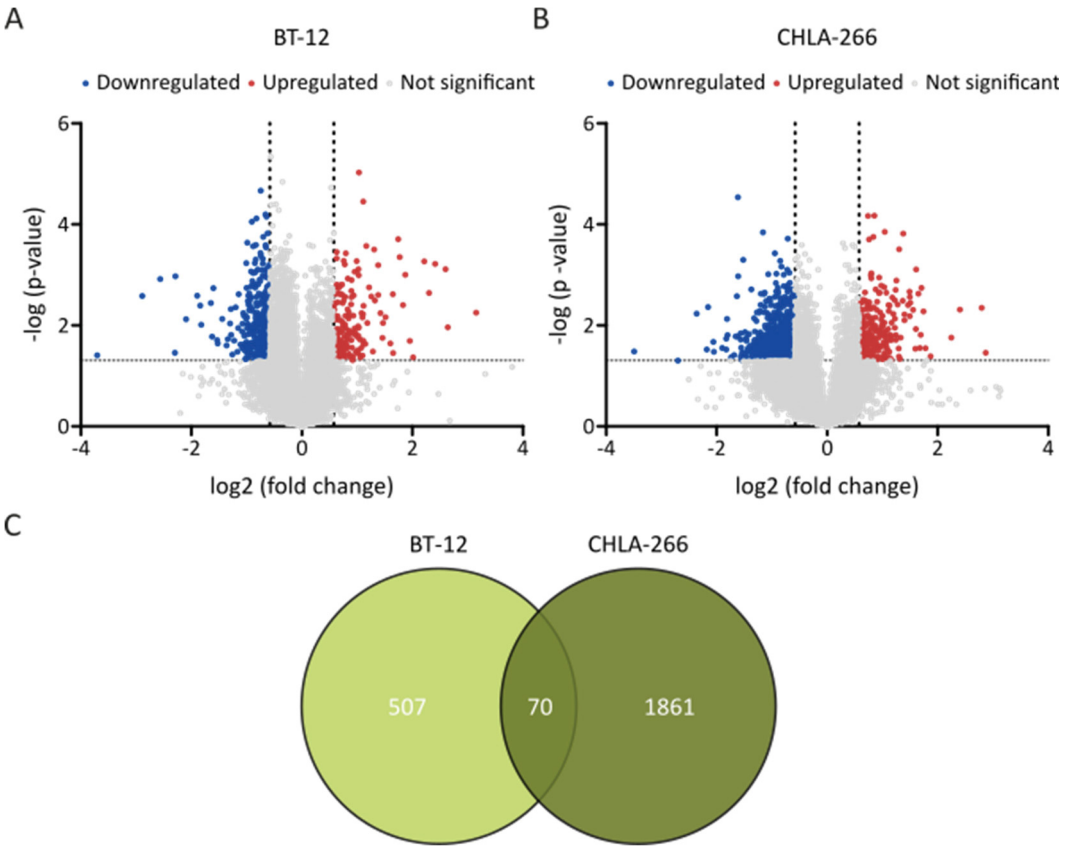

Figure 21: Knockdown of *kinesin family member 3A (KIF3A)* results in transcriptomic changes in the AT/RT cell lines BT-12 and CHLA-266. Volcano plots showing downregulated (blue dots), upregulated (red dots) and not significant (grey dots) genes following *KIF3A* knockdown in BT-12 (A) and CHLA-266 (B) cells, using a minimal fold change of ±1.5 and a significance level of p≤0.05 as a cut-off. Statistical analysis was performed using the non-parametric Kruskal Wallis test. (C) Venn diagram showing the overlap of differentially regulated genes between BT-12 and CHLA-266 cells.

To elucidate canonical pathways and upstream regulators controlled by *KIF3A* knockdown, ingenuity pathway analysis (IPA) was performed on the 70 genes that were differentially expressed following *KIF3A* knockdown in both BT-12 and CHLA-266 cells.

Overall, three canonical pathways significantly dysregulated following *KIF3A* knockdown in both BT-12 and CHLA-266 cells were identified, namely thiamin salvage III, interferon signaling and inflammasome pathway (Table 22).

Table 22: Canonical pathways controlled by *kinesin family member 3A (KIF3A)* knockdown at the transcriptome level. The canonical pathways are listed according to their p-value.

Ingenuity canonical pathways	p-value
Thiamin salvage III	0.002
Interferon signaling	0.003
Inflammasome pathway	0.047

Among the upstream regulators significantly dysregulated following *KIF3A* knockdown in both BT-12 and CHLA-266 cells, almost all upstream regulators (9 of 11, 82%) were functionally linked to lipid biosynthesis and metabolism, while 2 of the 11 upstream regulators (18%) were functionally linked to interferon signaling (Table 23).

Table 23: Upstream regulators controlled by *kinesin family member 3A (KIF3A)* knockdown at the transcriptome level. The upstream regulators are listed according to the activation z-score.

Upstream regulator	Molecule type	Activation z-score	p-value of overlap
SREBF1	Transcription regulator	-2.4	$1.9x10^{-7}$
SREBF2	Transcription regulator	-2.4	$1.8x10^{-10}$
SCAP	Other	-2.4	$2.1x10^{-12}$
ATP7B	Transporter	-2.2	$4.7x10^{-10}$
SH3TC2	Other	-2.0	$2.2x10^{-8}$
Insulin	Group	-2.0	$9.5x10^{-4}$
NCOA2	Transcription regulator	-2.0	$5.3x10^{-6}$
LEP	Growth factor	1.5	$9.4x10^{-5}$
POR	Enzyme	2.0	$1.1x10^{-6}$
MFSD2A	Transporter	2.0	$6.8x10^{-9}$
INSIG1	Other	2.4	$8.6x10^{-10}$

SREBF: sterol regulatory element binding transcription factor, SCAP: SREBF chaperone, ATP7B: ATPase copper transporting beta, SH3TC2: SH3 domain and tetratricopeptide repeats 2, NCOA2: nuclear receptor co-activator 2, LEP: leptin, POR: cytochrome p450 oxidoreductase, MFSD2A: major facilitator superfamily domain containing 2A, INSIG1: insuin-induced gene 1

Unsupervised hierarchical clustering of the 70 genes differentially expressed following *KIF3A* knockdown in both BT-12 and CHLA-266 cells was sufficient to subdivide both models into treatment groups (siCTRL vs siKIF3A, Figure 22).

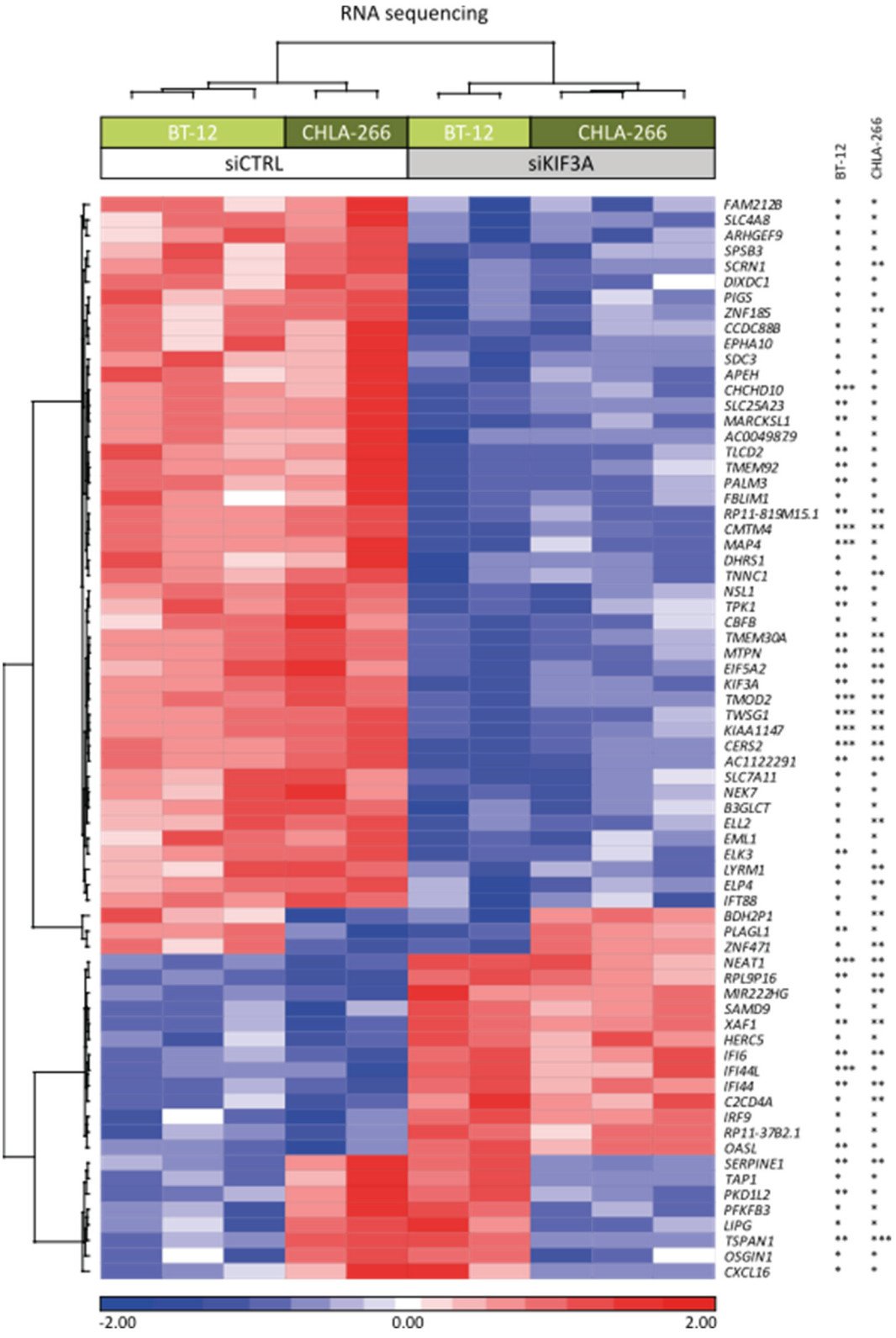

Figure 22: Unsupervised hierarchical clustering of the genes differentially expressed following *kinesin family member 3A (KIF3A)* knockdown in the AT/RT cell lines BT-12 and CHLA-266. The heatmap is based on all genes differentially regulated following *KIF3A* knockdown in both BT-12 and CHLA-266 cells, using a minimal fold change of ±1.5 and a significance level of p≤0.05 as a cut-off. Upregulated genes are shown in red and downregulated genes are shown in blue. *p<0.05; **p<0.01; ***p<0.001 (non-parametric Kruskal Wallis test).

4.3.2 Assessment of proteomic changes following *kinesin family member 3A* knockdown in the AT/RT cell lines BT-12 and CHLA-266

In order to analyze the correlation of the regulatory effects on RNA and protein level caused by *KIF3A* knockdown, siRNA-mediated knockdown of *KIF3A* was performed in the AT/RT cell lines BT-12 and CHLA-266. Following knockdown, global perturbations at the proteome level were determined using mass spectrometry.

Using a minimal fold change of ±1.5 and a significance level of p≤0.05 as a cut-off, a total of 102 and 88 differentially expressed proteins were identified in BT-12 and CHLA-266 cells, respectively (Figure 23 A, B). Amongst these, a total of 9 proteins were differentially expressed following *KIF3A* knockdown in both BT-12 and CHLA-266 cells (Figure 23 C).

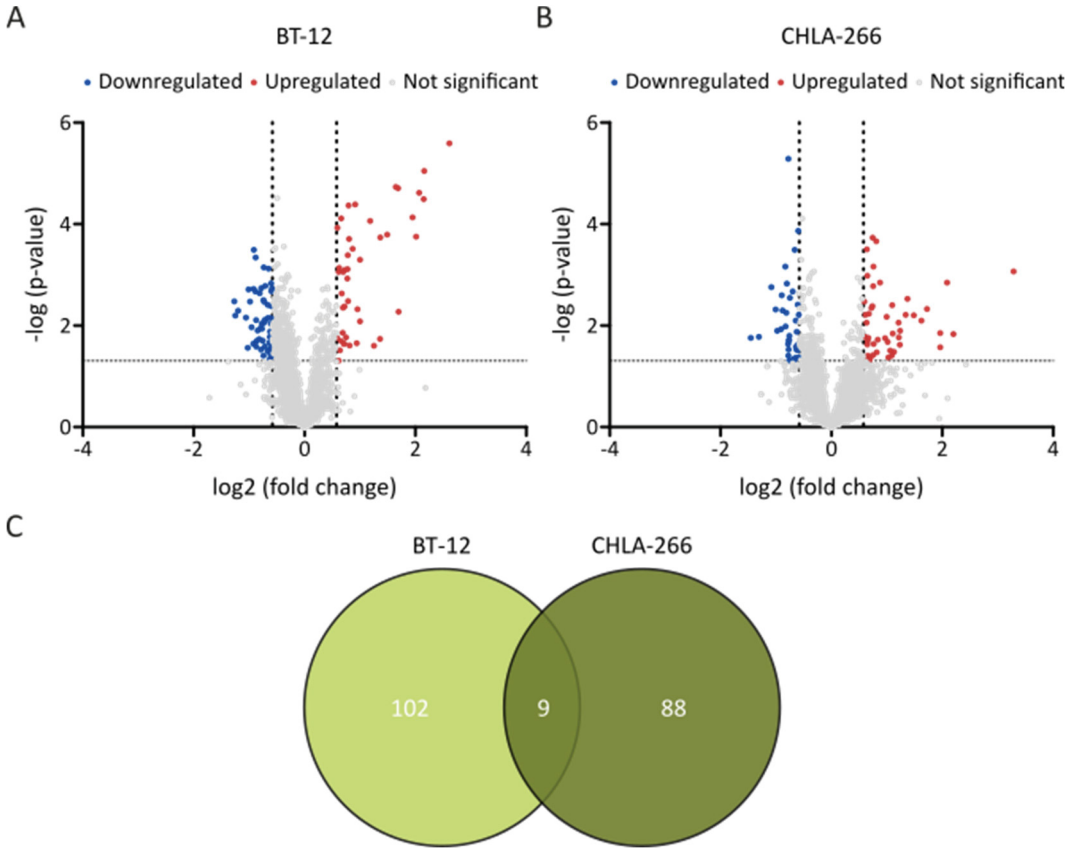

Figure 23: Knockdown of *kinesin family member 3A (KIF3A)* results in proteomic changes in the AT/RT cell lines BT-12 and CHLA-266. Volcano plots showing downregulated (blue dots), upregulated (red dots) and not significant (grey dots) proteins following *KIF3A* knockdown in BT-12 (A) and CHLA-266 (B) cells, using a minimal fold change of ±1.5 and a significance level of p≤0.05 as a cut-off. Statistical analysis was performed using the non-parametric Kruskal Wallis test. (C) Venn diagram showing the overlap of differentially regulated proteins between BT-12 and CHLA-266 cells.

To elucidate canonical pathways and upstream regulators controlled by *KIF3A* knockdown, IPA was performed on the 9 proteins that were differentially expressed following *KIF3A* knockdown in both BT-12 and CHLA-266 cells.

Overall, 37 canonical pathways significantly dysregulated following *KIF3A* knockdown in both BT-12 and CHLA-266 cells have been identified. Notably, 32 out of the 37 canonical pathways (86%) were functionally linked to interferon signaling, with interferon signaling itself being the most dysregulated canonical pathway identified (Table 24).

Table 24: Canonical pathways controlled by *kinesin family member 3A (KIF3A)* knockdown at the proteome level. The canonical pathways are listed according to their p-value.

Ingenuity canonical pathways	p-value
Interferon signaling	$7.4x10^{-10}$
Activation of IRF by cytosolic pattern recognition receptors	$1.8x10^{-6}$
Role of pattern recognition receptors in recognition of bacteria and viruses	$1.7x10^{-3}$
TEC kinase signaling	$1.9x10^{-3}$
IL-22 signaling	$9.8x10^{-3}$
Role of JAK1, JAK2 and TYK2 in interferon signaling	$9.8x10^{-3}$
Role of JAK family kinases in IL-6-type cytokine signaling	$1.0x10^{-2}$
IL-9 signaling	$1.4x10^{-2}$
Role of JAK2 in hormone-like cytokine signaling	$1.4x10^{-2}$
Role of PKR in interferon induction and antiviral response	$1.7x10^{-2}$
Oncostatin M signaling	$1.7x10^{-2}$
Role of RIG1-like receptors in antiviral innate immunity	$1.8x10^{-2}$
iNOS signaling	$1.8x10^{-2}$
EGF signaling	$2.2x10^{-2}$
Retinoic acid mediated apoptosis signaling	$2.4x10^{-2}$
CNTF signaling	$2.5x10^{-2}$
Thrombopoietin signaling	$2.6x10^{-2}$
Role of JAK1 and JAK3 in Î³c cytokine signaling	$2.8x10^{-2}$
GM-CSF signaling	$2.8x10^{-2}$
Growth hormone signaling	$2.9x10^{-2}$
T helper cell differentiation	$3.0x10^{-2}$
IL-7 signaling pathway	$3.2x10^{-2}$
Role of BRCA1 in DNA damage response	$3.2x10^{-2}$
IL-3 signaling	$3.2x10^{-2}$
JAK/STAT signaling	$3.2x10^{-2}$
Prolactin signaling	$3.3x10^{-2}$

FLT3 signaling in hematopoietic progenitor cells	$3.4x10^{-2}$
PDGF signaling	$3.5x10^{-2}$
Death receptor signaling	$3.6x10^{-2}$
p53 signaling	$3.9x10^{-2}$
UVA-induced MAPK signaling	$3.9x10^{-2}$
Pancreatic adenocarcinoma signaling	$4.4x10^{-2}$
Type I diabetes mellitus signaling	$4.5x10^{-2}$
p38 MAPK signaling	$4.7x10^{-2}$
Renin-Angiotensin signaling	$4.7x10^{-2}$
IL-15 production	$4.8x10^{-2}$
TH1 Pathway	$4.9x10^{-2}$

IRF: interferon regulatory factor, IL: interleukin, JAK: janus kinase, TYK2: tyrosine kinase 2, PKR: protein kinase r, RIG1: retinoic acid inducible gene 1, iNOS: inducible nitric oxide synthase, EGF: epidermal growth factor, CNTF: ciliary neurotrophic factor, GM-CSF: granulocyte-macrophage colony-stimulating factor, STAT: signal transducer and activator of transcription, FLT3: fms related receptor tyrosine kinase 3, PDGF: platelet derived growth factor, MAPK: mitogen-activated protein kinase

Among the upstream regulators significantly dysregulated following *KIF3A* knockdown in both BT-12 and CHLA-266 cells, almost all upstream regulators (24 of 31, 77%) were functionally linked to interferon signaling as well (Table 25).

Table 25: Upstream regulators controlled by *kinesin family member 3A (KIF3A)* knockdown at the proteome level. The upstream regulators are listed according to the activation z-score.

Upstream regulator	Molecule type	Activation z-score	p-value of overlap
IFNA2	Cytokine	-2.6	$6.2x10^{-13}$
IFNG	Cytokine	-2.6	$1.5x10^{-7}$
PRL	Cytokine	-2.4	$3.7x10^{-10}$
IFNL1	Cytokine	-2.4	$2.5x10^{-13}$
EIF2AK2	Kinase	-2.4	$5.9x10^{-13}$
IFN Beta	Group	-2.4	$5.7x10^{-12}$
Interferon alpha	Group	-2.4	$5.6x10^{-9}$
IRF7	Transcription regulator	-2.4	$1.8x10^{-11}$
IRF1	Transcription regulator	-2.2	$3.7x10^{-9}$
STAT1	Transcription regulator	-2.2	$1.7x10^{-9}$
IRF3	Transcription regulator	-2.2	$7.8x10^{-9}$
PML	Transcription regulator	-2.2	$2.4x10^{-9}$
TNF	Cytokine	-2.2	$2.6x10^{-5}$
Ifn	Group	-2.2	$6.1x10^{-10}$
TLR7	Transmembrane receptor	-2.2	$1.2x10^{-8}$

TLR9	Transmembrane receptor	-2.2	$1.8x10^{-8}$
TGM2	Enzyme	-2.0	$1.4x10^{-6}$
JAK	Group	-2.0	$1.7x10^{-9}$
Ifnar	Group	-2.0	$4.0x10^{-8}$
IFNB1	Cytokine	-2.0	$3.9x10^{-6}$
IRF5	Transcription regulator	-2.0	$2.2x10^{-8}$
MAVS	Other	-2.0	$1.2x10^{-8}$
TNFSF10	Cytokine	-2.0	$5.2x10^{-8}$
IFN type 1	Group	-1.9	$3.3x10^{-9}$
MAPK1	Kinase	1.9	$9.9x10^{-12}$
TRIM24	Transcription regulator	1.9	$5.2x10^{-8}$
IL4	Cytokine	2.0	$4.2x10^{-4}$
MYC	Transcription regulator	2.0	$4.1x10^{-5}$
SOCS1	Other	2.0	$1.8x10^{-7}$
ACKR2	G-protein coupled receptor	2.0	$1.7x10^{-9}$
BTK	Kinase	2.2	$4.9x10^{-10}$

IFNA: interferon alpha, IFNG: interferon gamma, PRL: prolactin, IFNL: interferon lambda, EIF2AK2: eukaryotic translation initiation factor 2 alpha kinase 2, IRF: interferon regulatory factor, STAT1: signal transducer and activator of transcription 1, PML: promyelocytic leukemia, TNF: tumor necrosis factor, TLR: toll-like receptor, TGM2: transglutaminase 2, JAK: janus kinase, IFNAR: interferon alpha and beta receptor subunit, IFNB: interferon beta, MAVS: mitochondrial antiviral signaling protein, TNFSF10: TNF superfamily member 10, MAPK1: mitogen-activated protein kinase 1, TRIM24: tripartite motif containing 24, IL4: interleukin 4, SOCS1: suppressor of cytokine signaling 1, ACKR2: atypical chemokine receptor 2, BTK: bruton tyrosinase kinase

Unsupervised hierarchical clustering of the 9 proteins differentially expressed following *KIF3A* knockdown in both BT-12 and CHLA-266 cells was sufficient to subdivide both models into treatment groups (siCTRL vs siKIF3A, Figure 24).

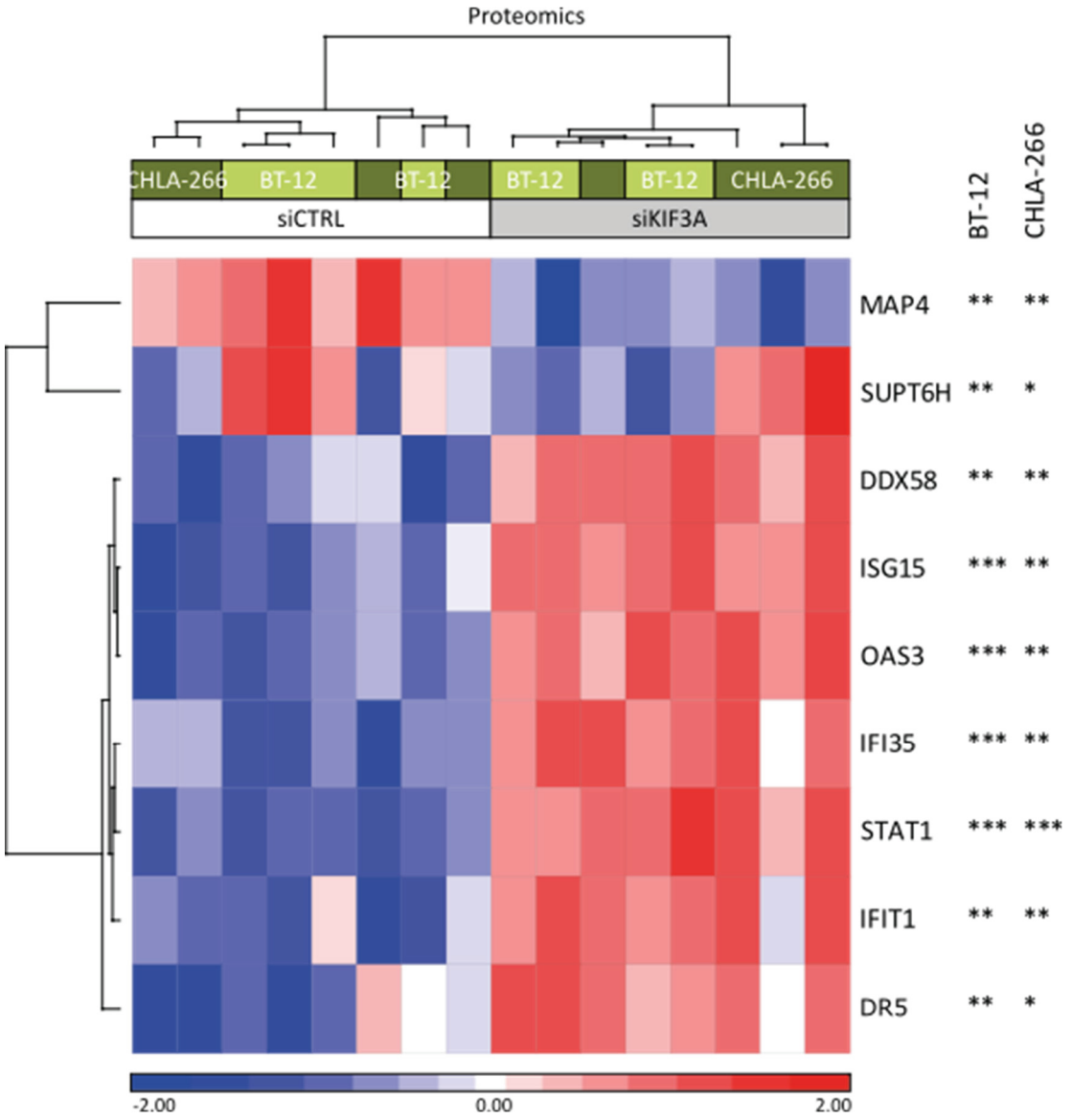

Figure 24: Unsupervised hierarchical clustering of the proteins differentially expressed following *kinesin family member 3A (KIF3A)* knockdown in the AT/RT cell lines BT-12 and CHLA-266. The heatmap is based on all proteins differentially regulated following *KIF3A* knockdown in both BT-12 and CHLA-266 cells, using a minimal fold change of ±1.5 and a significance level of p≤0.05 as a cut-off. Upregulated proteins are shown in red and downregulated proteins are shown in blue. *p<0.05; **p<0.01; ***p<0.001 (non-parametric Kruskal Wallis test).

4.3.3 Proteogenomic profiling following *kinesin family member 3A* knockdown in the AT/RT cell lines BT-12 and CHLA-266

By combining proteomics and genomics, proteogenomics allows for the analysis of the correlation of mRNA and protein across samples, thereby improving investigational power and identifying complex mechanisms behind biological functions. By employing

RNA sequencing and mass spectrometry following siRNA-mediated *KIF3A* knockdown in the AT/RT cell lines BT-12 and CHLA-266, transcriptomic and proteomic changes were assessed (see 4.3.1 and 4.3.2). Considering both the transcriptomic and the proteomic data, the only overlap observed between both data sets and between both cell lines was a significant induction of interferon signaling following *KIF3A* knockdown (Figure 25).

Figure 25: Proteogenomic profiling reveals induction of interferon signaling following *kinesin family member 3A (KIF3A)* knockdown in the AT/RT cell lines BT-12 and CHLA-266. Gene set enrichment analysis (GSEA) was performed for merged RNA sequencing and proteomics data. The integrative analysis shows only one gene set that is enriched in both data sets. Green circles: Overlap between mass spectrometry (MS) and RNA sequencing (RS) upregulated in *KIF3A* knockdown cells. Purple circles: Upregulated in MS *KIF3A* knockdown cells. Blue circle: Upregulated in RS *KIF3A* knockdown cells. Yellow circle: Upregulated in MS control cells.

Validation by quantitative real-time PCR revealed a significant increase in the expression of ten exemplary genes involved in interferon signaling, including *STAT1*, *OAS1*, *OAS2*, *OAS3*, *MX1*, *IFIT1*, *IFIT3*, *IFI35*, *ISG15* and *DR5*, following transient *KIF3A* knockdown in both cell lines investigated in this thesis (Figure 26 A, B). Western blot analysis corroborated not only increased STAT1 expression but also increased STAT1 phosphorylation on residue 701, thus, increased STAT1 activation following transient *KIF3A* knockdown in BT-12 and CHLA-266 cells. Moreover, an increased expression of DR5 was observed (Figure 26 C).

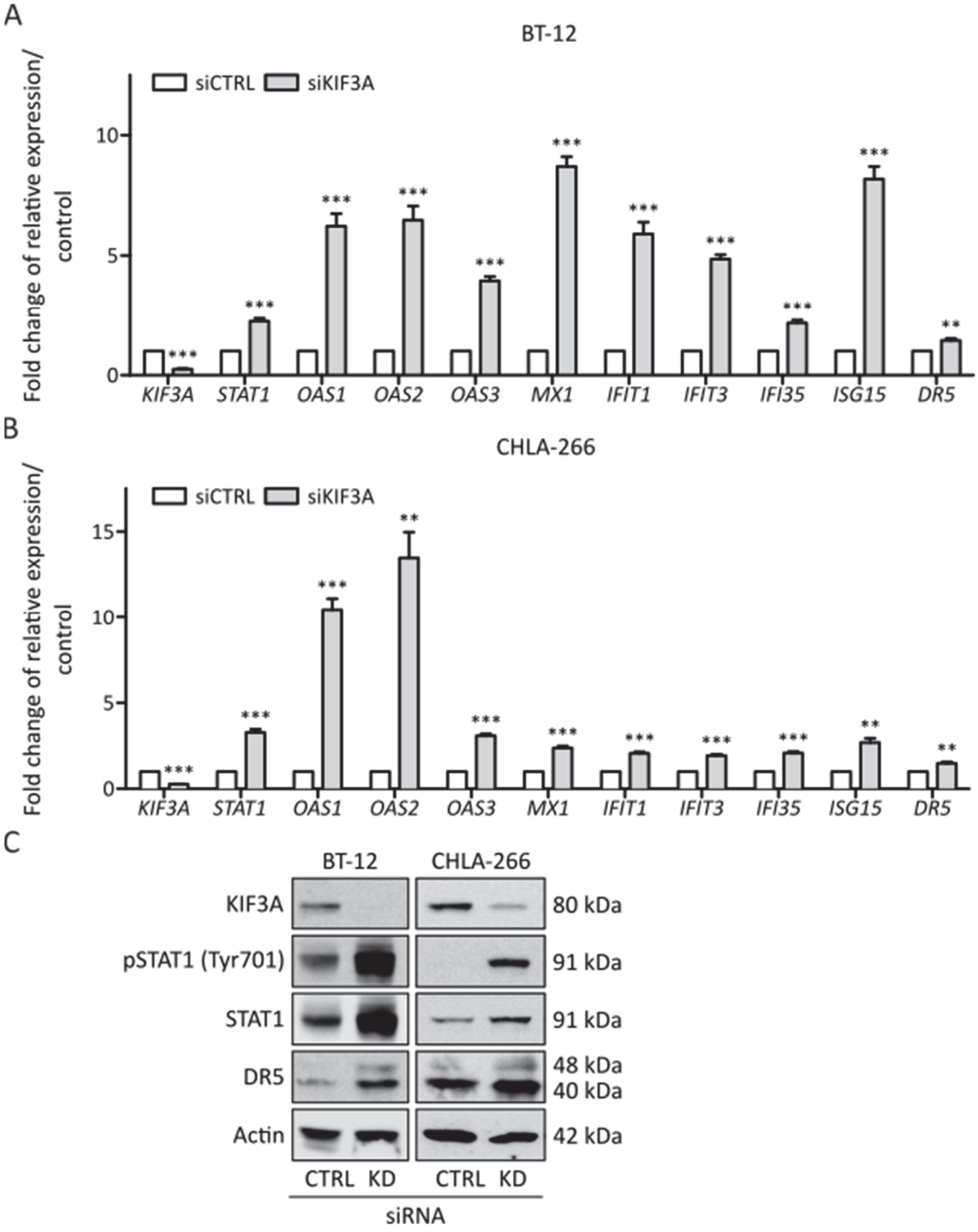

Figure 26: Proteogenomic profiling reveals induction of interferon signaling following *kinesin family member 3A (KIF3A)* knockdown in the AT/RT cell lines BT-12 and CHLA-266. siRNA-mediated knockdown of *KIF3A* in BT-12 and CHLA-266 cells was achieved using siPOOLs. (A) mRNA expression was normalized to the housekeeping genes *glyceraldehyde 3-phosphate dehydrogenase (GAPDH)* and *phosphoglycerate kinase 1 (PGK1)* and calculated relative to siCTRL. Values shown represent mean ± SEM of three replicates. **p<0.01; ***p<0.001 (student´s t-test). (B) Representative western blot images for KIF3A, pSTAT1 (Tyr701), STAT1, death receptor 5 (DR5) and Actin as a loading control following siRNA-mediated *KIF3A* knockdown.

Additionally, broad comparative expression analysis indicated a total of 1250 genes showing an anti-correlated expression with *KIF3A*. Amongst these, a large number of genes associated with interferon signaling and apoptosis were detected, including *STAT1*, *OAS1*, *OAS2*, *OAS3*, *MX1*, *IFIT1*, *IFIT3*, *IFI35*, *ISG15* and *DR5* (Figure 27 A-J).

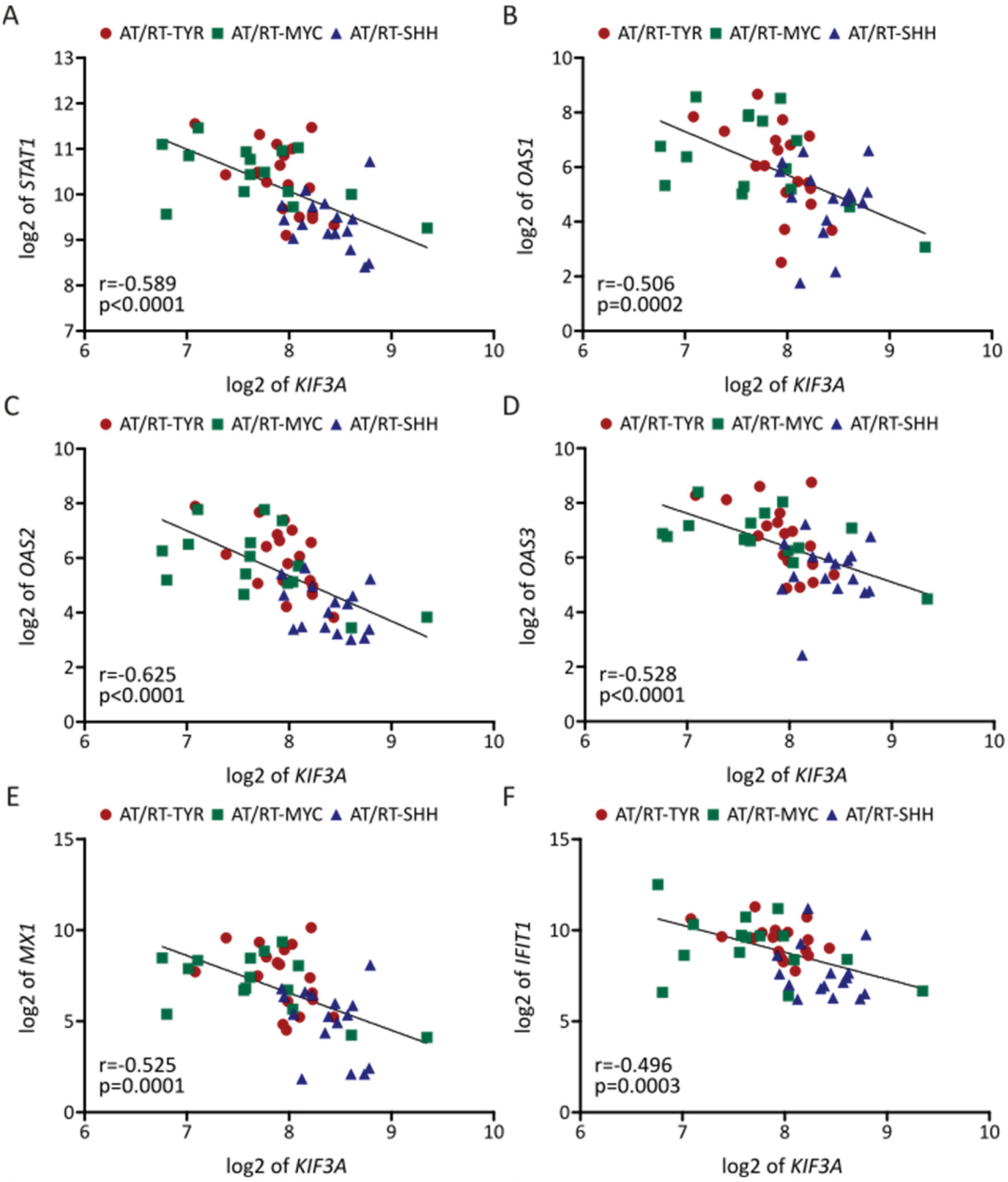

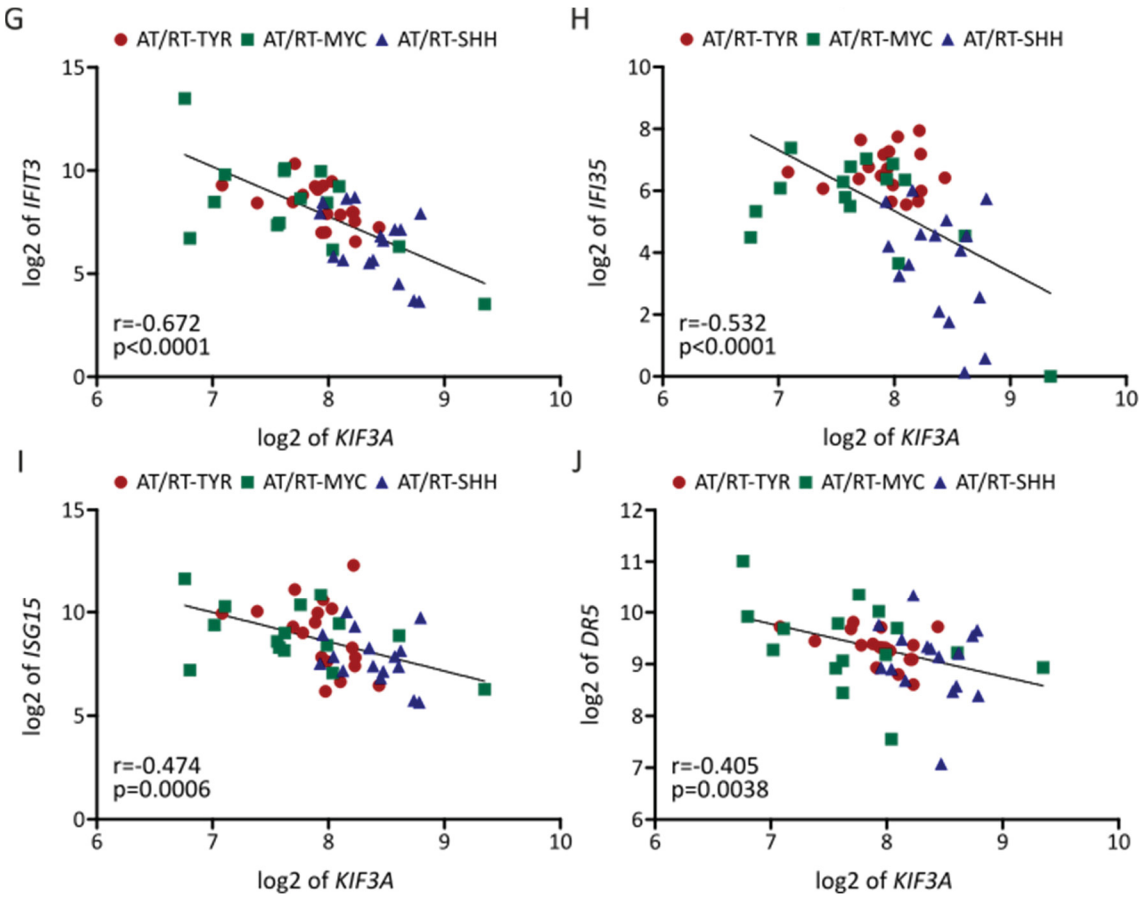

Figure 27: Interferon-induced genes show anti-correlated expression with *kinesin family member 3A (KIF3A)*. Gene expression data is derived from the Tumor ATRT - Kool - 49 - MAS5.0 - u133p2 data set available at the R2: Genomics analysis and visualization platform (http://r2.amc.nl).

4.4 Cilia-associated genes are involved in the lethal phenotype in a *Drosophila* model of *SWI/SNF related matrix associated actin dependent regulator of chromatin subfamily b member 1* deficiency

Given the anti-tumoral effect of *KIF3A* knockdown *in vitro*, the role of primary cilia in AT/RT biology was also investigated *in vivo*.

The first *in vivo* studies for this project were conducted in collaboration with the research group of Prof. Dr. Martin Hasselblatt from the Institute of Neuropathology at the University Hospital in Münster, Germany. His group has established a *Drosophila* model of glial-specific *Snr1* (*Drosophila* orthologue of *SMARCB1*) deficiency that leads to death at the pupal stage of development and, therefore, allows for high throughput screens of genes functionally involved in the lethal phenotype of *Snr1* deficiency (Figure 28).

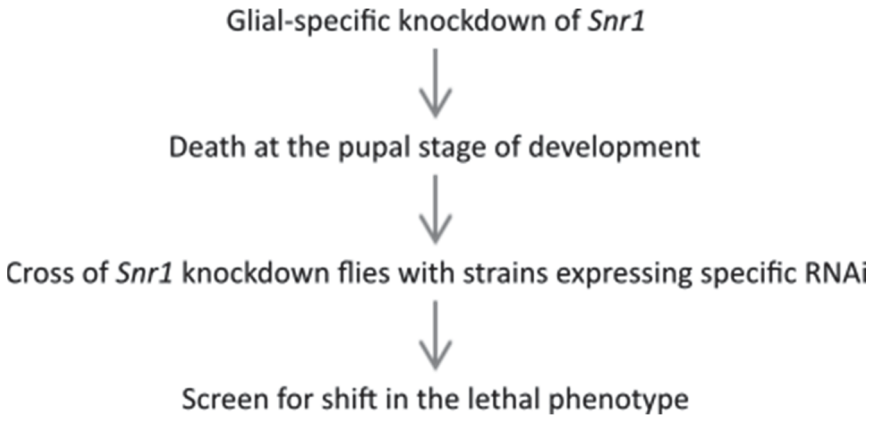

Figure 28: Workflow for the modifier screen in *Drosophila melanogaster*. In *Drosophila*, glial-specific knockdown of *Snf5-related 1 (Snr1)*, the *Drosophila* orthologue of *SWI/SNF related matrix associated actin dependent regulator of chromatin subfamily b member 1 (SMARCB1)*, results in death at the pupal stage of development. Crossing *Snr1* knockdown flies with strains expressing specific RNA interference (RNAi) allows for a screen for a shift in the lethal phenotype to later stages of development in order to identify genes and associated pathways that are involved in the lethal phenotype of *Snr1* knockdown.

In order to investigate the importance of primary ciliogenesis in this *Drosophila* model, *Snr1* knockdown flies were crossed with strains expressing specific RNAi for 59 genes associated with ciliogenesis (the complete list of the 59 genes examined is shown in Supplementary table 1). Afterwards, a screen for a shift in the lethal phenotype was conducted.

As reported previously, glial-specific knockdown of *Snr1* caused a lethal phenotype in *Drosophila* with death at the pupal stage of development. Notably, additional knockdown of 14 out of the 59 examined cilia-associated genes (24%) resulted in a substantial shift of the lethal phenotype with >20% of flies reaching adulthood (Figure 29).

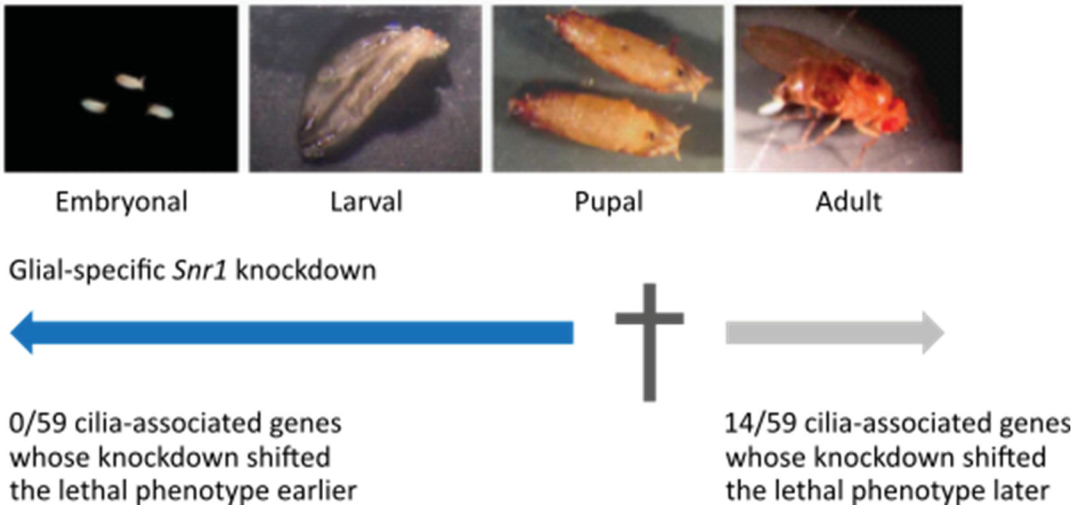

Figure 29: Modifier screen in *Drosophila melanogaster*. Crossing of *Snf5-related 1 (Snr1)* knockdown flies with strains expressing specific RNA interference (RNAi) shifted the pupal lethal phenotype associated with glial-specific *Snr1* knockdown to later stages of development in 14 out of 59 screened candidate genes. The complete list of the 59 genes examined is shown in Supplementary table 1. Adapted from Jeibmann et al.[140].

4.5 Knockdown of *kinesin family member 3A* prolongs median survival in an orthotopic xenograft mouse model of AT/RT

The second *in vivo* studies for this project were conducted in collaboration with the research group of Cláudia Faria (MD, PhD) from the Instituto de Medicina Molecular João Lobo Antunes at the Faculdade de Medicina da Universidade de Lisboa in Lisbon, Portugal, using an orthotopic xenograft mouse model of AT/RT.

For this, BT-12 shCTRL vs BT-12 shKIF3A cells were orthotopically injected in the right hemisphere of the frontal cortex of NSG mice. After tumor engraftment, control mice exhibited a median survival of 32 days (Figure 30). Knockdown of *KIF3A* resulted in a significantly prolonged median survival of 36 days (Figure 30).

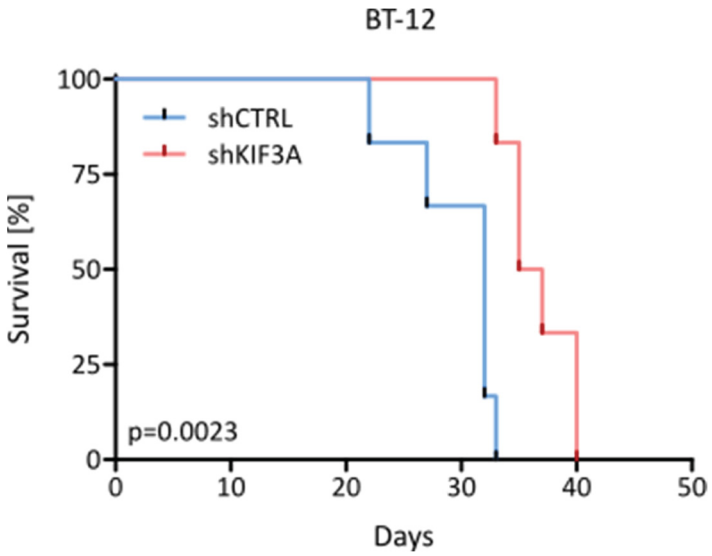

Figure 30: Knockdown of *kinesin family member 3A (KIF3A)* prolongs median survival in an orthotopic xenograft mouse model of AT/RT. Kaplan-Meier survival curve of NOD scid gamma (NSG) mice orthotopically injected with control BT-12 cells (shCTRL, blue) or *KIF3A* knockdown BT-12 cells (shKIF3A, red). Statistical analysis was performed using the Gehan-Breslow-Wilcoxon test. **p<0.01.

4.6 Drug screening reveals vulnerabilities following knockdown of *kinesin family member 3A* in the AT/RT cell lines BT-12 and CHLA-266

Given the anti-tumoral effect of *KIF3A* knockdown, the susceptible to the treatment with pharmacological compounds was investigated following *KIF3A* knockdown in the AT/RT cell lines BT-12 and CHLA-266.

Therefore, the sensitivity of BT-12 shCTRL vs BT-12 shKIF3A and CHLA-266 CRISPRiCTRL vs CHLA-266 CRISPRiKIF3A cells was tested towards an in-house established clinical compound library, consisting of 199 compounds that are either already used in the clinic for the treatment of different types of cancers or are at least part of clinical phase III or IV trials (the complete list of the 199 compounds examined is shown in Supplementary table 2).

Overall, a total of three inhibitors were identified that showed a lower IC_{50} following *KIF3A* knockdown in both BT-12 and CHLA-266 cells, including 3-Deazaneplanocin A (a potent histone methyltransferase EZH2 inhibitor, Figure 31 A, B), Dovitinib (a multi-targeted tyrosine kinase inhibitor, targeting FLT3, c-Kit, FGFR1/3, VEGFR1/2/3 and PDGFRα/β, Figure 31 C, D) and GSK525762A (a small molecule inhibitor of the BET family of bromodomain-containing proteins, Figure 31 E, F).

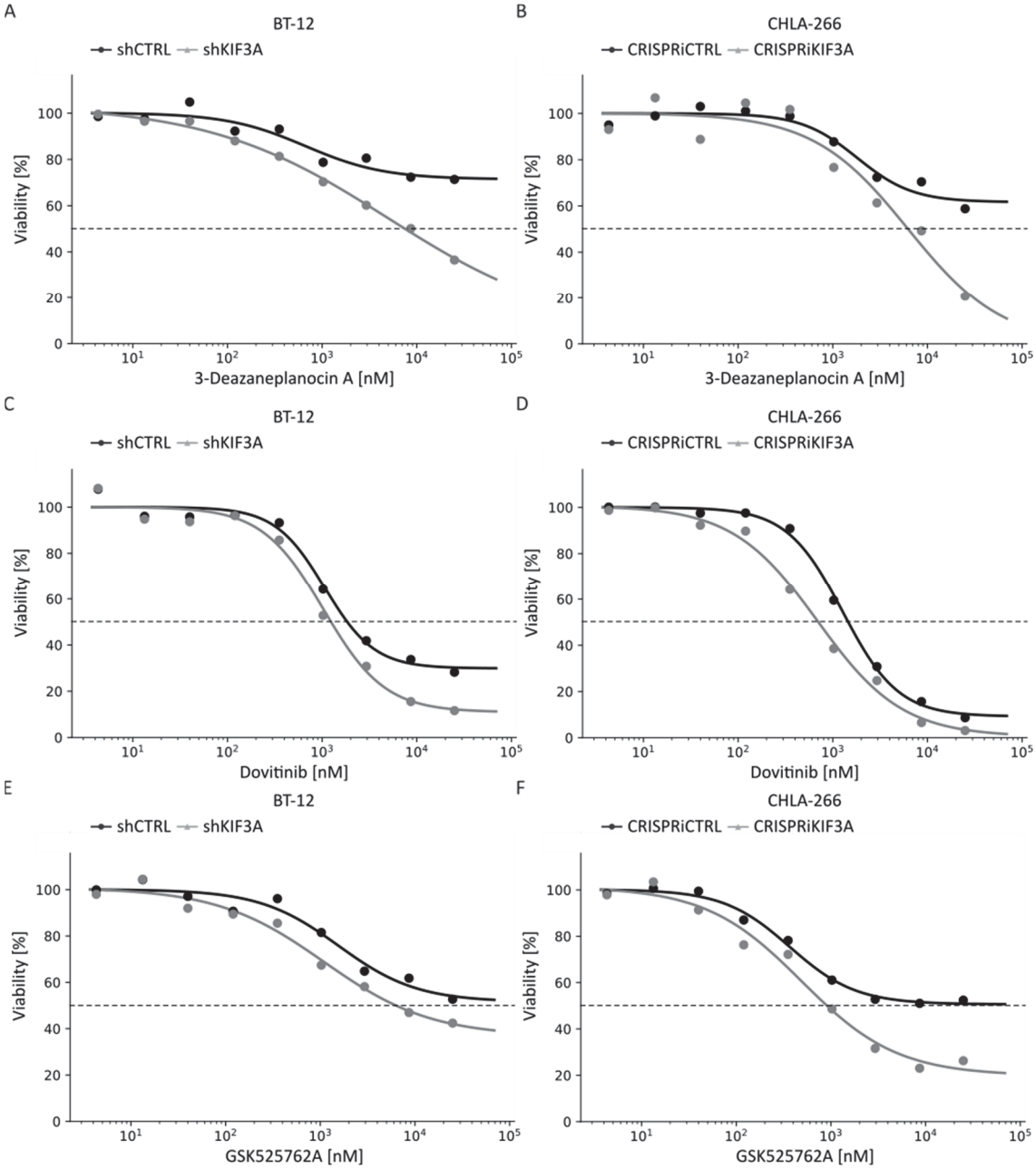

Figure 31: Drug screening reveals increased vulnerability towards 3-Deazaneplanocin A, Dovitinib and GSK525762A following *kinesin family member 3A (KIF3A)* knockdown in the AT/RT cell lines BT-12 and CHLA-266. Stable transfected BT-12 and CHLA-266 cells were exposed to an in-house established clinical compound library, consisting of 199 compounds. Shown are the dose-response curves for 3-Deazaneplanocin A (A, B), Dovitinib (C, D) and GSK525762A (E, F), showing a difference between shCTRL/CRISPRiCTRL and shKIF3A/CRISPRiKIF3A cells. The complete description of the clinical compound library is shown in Supplementary table 2.

5 Discussion

For decades, primary cilia have been regarded as rudimentary organelles. Since they are known to regulate established cancer signaling pathways, however, a crucial role for primary cilia in cancer initiation and progression is emerging. Given the increasing interest in the role of primary cilia in cancer, this thesis aimed to analyze the distribution of primary cilia across AT/RT subgroups and to target primary ciliogenesis in these highly malignant and prognostically dismal tumors.

In order to investigate whether AT/RT cells carry primary cilia, an immunofluorescence protocol was established to detect primary cilia in AT/RT patient samples and AT/RT cell lines. For this, primary antibodies directed against Pericentrin and Acetylated tubulin were employed, detecting the basal body and the axoneme of the primary cilium, respectively.

Using this immunofluorescence approach, primary cilia were detected in the tumor tissue sections of all 13 AT/RT patients and in the AT/RT cell lines BT-12 and CHLA-266. Hence, this is the first study reporting about the presence of this organelle in AT/RTs. Notably, also a subgroup-specific difference in the percentage of ciliated cells was observed, with AT/RT-TYR tumors demonstrating the highest percentage of ciliated cells and AT/RT-MYC and AT/RT-SHH tumors showing a variable degree and the lowest proportion of cells with a primary cilium, respectively. Since SHH signaling is the best-studied pathway linked to primary cilia[88–92], it is rather unexpected that AT/RT-SHH tumors showed the lowest proportion of cells with a primary cilium across subgroups. However, this might be explained by the hypothesis that AT/RT-SHH tumors rely on downstream activation of SHH signaling and, therefore, lack primary cilia, while AT/RT-TYR tumors, that demonstrate the highest percentage of ciliated cells across subgroups, rely on upstream activation of SHH signaling and, thus, retain primary cilia. A dual and opposing role for primary cilia has already been suggested for SHH-dependent medulloblastoma and BCC[105,106], supporting the proposed hypothesis. Specifically, ciliary ablation was needed to inhibit tumor growth when the tumor was driven by constitutively active SMO, an upstream activator of SHH signaling. On the contrary,

ablation of cilia was required for tumorigenesis when the tumor was driven by constitutively active GLI2, a downstream activator of SHH signaling[105,106]. The finding that the TYR subgroup of AT/RT presents the subgroup with the highest percentage of ciliated cells is also supported by recent large-scale multicenter studies, uncovering that many genes involved in ciliogenesis are highly expressed in the TYR subgroup of AT/RT[61].

In order to investigate the role of primary cilia in AT/RT, both transient and stable knockdown of the crucial ciliary marker *KIF3A* was conducted in both AT/RT cell lines investigated in this thesis. KIF3A is one subunit of the heterotrimeric motor protein kinesin-2, consisting of two kinesin-related subunits (KIF3A and KIF3B or KIF3C) and an associated protein (KAP3), that moves IFT particles and their protein cargos along the ciliary axoneme towards the ciliary tip and, thus, is involved in the assembly of primary cilia[67]. Previous studies have shown that disruption of primary ciliogenesis can be achieved by genetic ablation of *KIF3A*[105,106,136,137]. Indeed, disruption of primary ciliogenesis following *KIF3A* knockdown was confirmed in both AT/RT cell lines investigated in this thesis. In addition, *KIF3A* knockdown resulted in a significant reduction of tumor-associated properties. Specifically, a significant decrease in proliferation and clonogenicity was observed. Furthermore, cell cycle analysis revealed a significant decrease in the G2M fraction of cells, importantly, concomitant with a significant increase in the sub G1 fraction of cells, suggesting an increase in apoptotic cells following *KIF3A* knockdown. To confirm this hypothesis, an Annexin V and PI staining was performed, since this method presents an apoptosis-specific approach. Indeed, *KIF3A* knockdown in AT/RT cells resulted in a significant increase in apoptotic cells. This is in line with previous studies, reporting about tumor growth arrest upon KIF3A ablation in medulloblastoma and glioblastoma cells[136,137]. These findings were further validated by disrupting primary ciliogenesis exerting an alternative approach, that is pharmacological inhibition with Ciliobrevin D. Discovered by Firestone and colleagues[139], Ciliobrevins are the first specific small-molecule antagonists of cytoplasmic dynein. They have been shown to perturb protein trafficking within the primary cilium, thereby inhibiting primary cilia formation, and to block SHH signaling[139]. Overall, Ciliobrevin D treatment widely mimicked the results from the *KIF3A* knockdown

experiments, suggesting that primary cilia, indeed, contribute to the aggressive phenotype of AT/RT cells *in vitro*. Thus far, there is no study reporting about a trial to treat ciliated tumor cells with Ciliobrevin D. This is probably due to the fact that almost every cell in the human body comprises a primary cilium and Ciliobrevin D, therefore, would also target healthy cells. Thus, rather basic research on the effect of Ciliobrevin D on cellular processes that require cytoplasmic dynein has been published, including investigations on spindle pole assembly and kinetochore-microtubule attachment, melanosome aggregation and peroxisome motility as well as cytoplasmic dynein-dependent microtubule gliding and ATPase activity[139,141,142]. Firestone and colleagues, for instance, found that Ciliobrevin D induces spindle defects (abnormal spindles with disrupted gamma-tubulin localization)[139]. This is in line with the G2M arrest observed in this thesis, suggesting that Ciliobrevin D treatment results in disrupted mitosis. However, further studies are required to validate this hypothesis.

The relevance of primary ciliogenesis in AT/RT biology was also confirmed *in vivo* using a *Drosophila* model of *SMARCB1* deficiency and an orthotopic xenograft mouse model of AT/RT. Overall, *Drosophila* is used as a model organism to study a vast array of disciplines, ranging from basic genetics to the development of tissues and organs[143]. Interestingly, the *Drosophila* genome is 60% homologous to the human genome and, notably, about 75% of the genes responsible for human diseases have homologs in flies[144]. These features, together with a brief generation time, low maintenance costs, and the availability of powerful genetic tools, allow *Drosophila* to be eligible to study complex pathways relevant in biomedical research, including cancer. In the last decade, publications that use *Drosophila* to model cancer have exponentially increased, corroborating the relevance of this model to cancer research[143]. Since recurrent genetic alterations are mainly restricted to the *SMARCB1* gene, AT/RT represents a tumor entity ideally suited for modeling in *Drosophila*. Moreover, *Drosophila* is a preferred model organism to study centrosome and cilia biology, since sensory reception is mediated by a single cilium on each type-I sensory neuron of the peripheral nervous system. In general, there are two variants of type-I sensory neuron cilia present. First, there are cilia in external sensory neurons (without dynein arms) that are believed to be immotile,

and second, there are cilia in chordotonal neurons (with dynein arms) that are considered motile[145,146]. Notably, IFT is required for the assembly of all cilia on sensory neurons and SHH signaling is required for the function of olfactory cilia in external sensory neurons[147,148]. Therefore, a high throughput screen of genes functionally involved in the lethal phenotype of *Snr1* (*Drosophila* orthologue of *SMARCB1*) deficiency was conducted. Interestingly, additional knockdown of 14/59 examined cilia-associated genes resulted in a substantial shift of the lethal phenotype with >20% of flies reaching adulthood. Notably, the proportion of cilia-associated genes causing a positive shift of the phenotype in this thesis was significantly higher compared to the proportion previously reported for a large set of genes with known nervous system expression (14/59 vs 60/1015; Chi-square: 27,592; df:1, p<0,001; Figure 32), suggesting that cilia-associated genes, indeed, have an important role in the detrimental effects of *Snr1* knockdown in *Drosophila*.

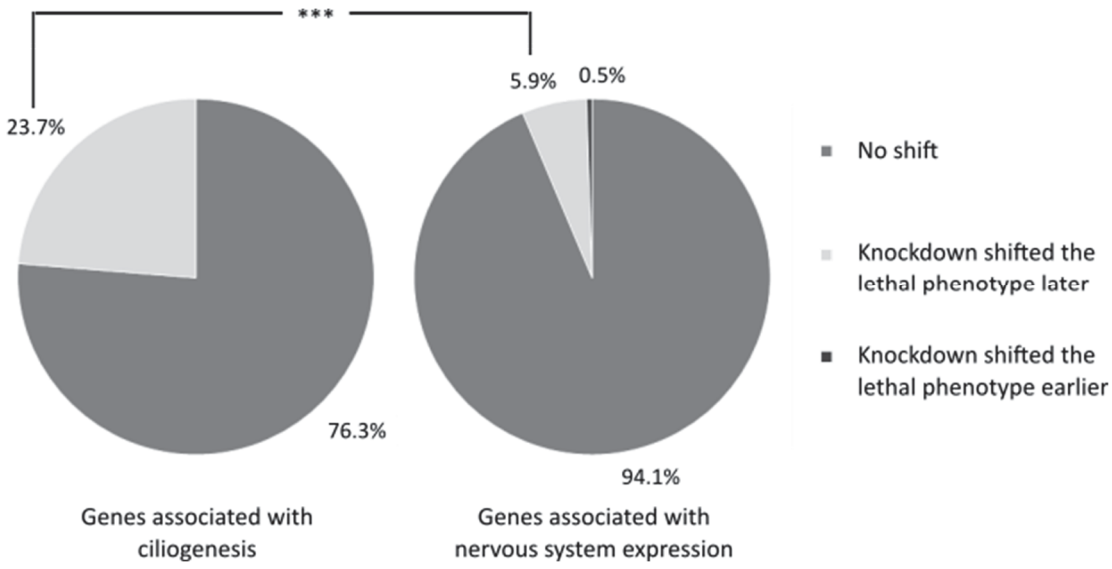

Figure 32: Comparison between two high throughput screens of genes functionally involved in the lethal phenotype of *Snf5-related 1 (Snr1)* deficiency. The proportion of cilia-associated genes causing a positive shift of the phenotype in this thesis (genes associated with ciliogenesis) was significantly higher compared to the proportion previously reported[140] for a large set of genes with known nervous system expression. (14/59 (23.7%) vs 60/1015 (5.9%); Chi-square: 27.592; df:1, ***p<0.001).

These findings were further validated in an orthotopic xenograft mouse model of AT/RT, in that mice that were intracranially injected with *KIF3A* knockdown BT-12 cells showed

a significantly prolonged median survival compared to mice that were intracranially injected with control BT-12 cells.

In order to elucidate the biological mechanism that could be responsible for the anti-tumoral effect following *KIF3A* knockdown, comprehensive analysis of the transcriptome and the proteome was conducted following *KIF3A* knockdown in the AT/RT cell lines BT-12 and CHLA-266. Notably, proteogenomic profiling revealed significant induction of only one canonical pathway, in fact of interferon signaling, as detected by GSEA.

Based on the type of receptor interferons are signaling through, they have been classified into three main types (interferon type I, interferon type II and interferon type III). To mediate signaling, interferon receptors are associated with a member of the janus-activated kinase/signal transducer and activator of transcription (JAK/STAT) family[149]. To date, a total of seven members of the STAT family of transcription factors have been identified (STAT1, STAT2, STAT3, STAT4, STAT5A, STAT5B and STAT6) that regulate the expression of a vast array of genes involved in immunity, proliferation, differentiation, survival and apoptosis[150,151]. Targeted deletion of specific members has revealed cell type-specific roles, with STAT1 being the major effector of interferon type II signaling[152,153]. STAT1 is activated through receptor-mediated tyrosine phosphorylation on residue 701, primarily by kinases of the JAK family, resulting in SH2-dependent STAT1 dimerization and nuclear translocation[154]. Nuclear STAT1 dimers activate gene transcription by recognizing specific sequence motifs, so-called gamma-activated sites (GAS), in their promoters[151,155]. Dephosphorylation of STAT1 dimers occurs in response to nuclear phosphatases, leading to inactivation and subsequent nuclear export of STAT1 dimers. In response to IFN-alpha/beta, STAT1 can also form STAT1/STAT2 heterodimers. Together with IRF9, STAT1/STAT2 dimers form a transcriptional complex (ISGF3) that enters the nucleus and binds to IFN-stimulated response elements[150].

Growing evidence suggests that STAT1 has tumor promoting functions, ranging from promotion of tumor cell growth and invasiveness to immune evasion and suppression

to induction of therapy resistance, but, in general, STAT1 is considered to act as a tumor suppressor[156]. In several types of cancers, including colorectal carcinoma[157], hepatocellular carcinoma[158], esophageal squamous cell carcinoma[159], pancreatic cancer[160], soft tissue sarcoma[161] and metastatic melanoma[162], STAT1 expression has been correlated with good prognosis. In fact, tumor suppression by STAT1 takes place at multiple levels, including tumor cell-intrinsic growth control and cross talk with other cells to modulate cancer immunoediting and suppress angiogenesis. Specifically, the effects of STAT1 range from cell cycle inhibition and sensitization to apoptotic stimuli to the induction of different forms of cell death by transcriptionally regulating the expression of cell cycle regulators[163–165], pro-apoptotic proteins[166–168] and death receptors and their ligands[169–171]. Besides, STAT1 regulates innate and adaptive immune responses against transformed cells[172–174]. Moreover, STAT1 regulates surface receptor expression on tumor cells that affect their recognition by immune cells[175–177], and also anti-angiogenic functions of STAT1 have been reported[178–180].

Since the *in vitro* experiments were conducted without any co-culture with immune cells and since the mouse *in vivo* experiments were performed in NSG mice, the induction of interferon signaling following *KIF3A* knockdown observed in the AT/RT cells needs to be mediated by tumor cell-intrinsic growth control mechanisms. In this thesis, *KIF3A* knockdown resulted in a marked increase not only in STAT1 expression but also in STAT1 phosphorylation at tyrosine residue 701, indicating an increase in STAT1 signaling. Moreover, several STAT1-induced genes were upregulated, with concomitant upregulation of a death receptor, in fact of DR5, confirming the previously observed induction of apoptosis following *KIF3A* knockdown using cell cycle analyses and Annexin V and PI stainings and suggesting that in AT/RT, primary cilia suppress apoptosis by suppressing STAT1 signaling.

Thus far, there is no study reporting about a direct link between primary cilia and STAT1 signaling in cancer. There are only few studies reporting about similar observations. Otsuka and colleagues, for instance, found that SHH pathway inhibitor-induced tumor regression in patients with BCC is accompanied not only by a significant decrease in the expression of tumor- or BCC-associated proteins, concomitant with a significant

decrease in cilia-positive BCC cells but also by promotion of adaptive immune cell infiltration, upregulation of MHC class I and alterations of the cytokine and chemokine milieu[181]. Another study by Wang and colleagues supports the idea that INTU, a ciliogenesis and planar polarity effector (CPLANE) protein, localizes at the centriole/basal body area in mouse and rat kidney proximal tubular cells and likely interacts with STAT1 to induce its proteasomal degradation, thereby protecting the cells from ischemic kidney injury[182]. Furthermore, Wee and colleagues report that interferon-γ receptor 1 (IFNGR1) is a target of EZH2 in MYC-driven advanced prostate cancer, since depletion of EZH2 restores defective IFN-IFNGR1-STAT1 signaling and since pharmacologic inhibition of EZH2 synergizes with IFN-γ *in vitro* and *in vivo*[183].

The latter study is especially interesting, since the evaluation of an in-house established clinical compound library, consisting of 199 either clinically established or currently evaluated (clinical phase 3/4) inhibitors, revealed marked activity of 3-Deazaneplanocin A, a potent EZH2 inhibitor, in *KIF3A* knockdown cells, while control cells showed just little response, suggesting that *KIF3A* knockdown synergizes with pharmacological inhibition of EZH2.

Indeed, several studies have shown that 3-Deazaneplanocin A is effective in a variety of tumor cells, including colon carcinoma cells[184], acute myeloid leukemia cells[185], non-small cell lung cancer cells[186], ovarian cancer cells[187], B-cell lymphoma cells[188] and gastric cancer cells[189]. Additionally, an anti-proliferative effect of 3-Deazaneoplanocin A in rhabdoid tumor cell lines has been observed, especially when combined with conventional cytostatic drugs or epigenetic active compounds[34].

On the contrary, another study reports that EZH2 promotes disassembly of the primary cilium by suppressing ciliary genes and that loss of this organelle initiates metastatic melanoma[116]. In AT/RT, however, it seems to be the other way around. Although downregulation of *EZH2* following *KIF3A* knockdown is not significant in this thesis (RNA sequencing data, data not shown), it might be sufficient to reactivate the expression of STAT1 that, in turn, leads to decreased tumorigenesis and increased apoptosis. Notably, this hypothesis is strengthened by the fact that *KIF3A* knockdown lead to a marked

increase in the response to 3-Deazaneplanocin A. Indeed, EZH2 expression is regulated by various oncogenic transcription factors, tumor suppressor miRNAs, and cancer-associated non-coding RNAs. Thus, further studies are required to fully understand the mechanism controlling primary cilia and STAT1 signaling, with a focus on EZH2 as a potential linker.

6 Conclusion and outlook

Our knowledge of the primary cilium is the result of more than fifty years of research that has dramatically changed our perspective on this once unattended organelle[190]. By now, it is well known that the primary cilium functions as a cellular antenna. Specifically, it acts as a key coordinator of signaling pathways, converting external stimuli into cellular responses[87]. Given its critical functions, it is not surprising that any defects in the formation or function of primary cilia lead to a vast array of diseases, collectively known as ciliopathies. Notably, also a role for primary cilia in cancer is emerging.

Overall, the reported number of primary cilia is lower in tumor tissues compared to their respective controls. Different, though, is the role they play, since primary cilia have been reported to have dual and opposing roles between tumor types and within tumor subtypes. Specifically, they can act as both tumor suppressors and tumor promoters.

Several studies support the idea of primary cilia being rather inhibitors of cancer growth. Restoration of primary cilia in tumor cells, for instance, has been proposed to present a therapeutic strategy. Specifically, several compounds have been found to restore the formation of primary cilia, including glucocorticoids, fibrates and other nuclear receptor modulators, neurotransmitter regulators, ion channel modulators, tyrosine kinase inhibitors, DNA gyrase/topoisomerase inhibitors, anti-bacterial compounds, protein inhibitors, microtubule modulators and COX inhibitors, thereby inhibiting tumor cell growth[191]. In addition, higher frequencies of primary cilia have been correlated with longer overall survival[127,128].

Other studies, on the contrary, report about primary cilia being rather promoters of cancer growth. For instance, their presence has been correlated with the expression of proteins linked to tumor initiation and progression[109]. Moreover, they have been found to be required for the maintenance of tumor-initiating cells[119]. Furthermore, their presence has been correlated with an increased number of lymph node metastasis and, thus, with poor overall survival[121,122].

In summary, this thesis reports on the presence of primary cilia in AT/RT. Importantly, the percentage of ciliated cells was found to vary across molecular subgroups of AT/RT, with AT/RT-TYR tumors showing the highest fraction of ciliate tumor cells. Overall, this thesis provides further evidence that primary cilia contribute to the malignant phenotype of cancer, since their presence is shown to be important for the tumorigenesis of AT/RT both *in vitro* and *in vivo*.

Even though the importance of primary cilia in AT/RT is obvious, further studies are required to fully understand the association between primary cilia and tumorigenesis. First results obtained in this thesis indicate a role for primary cilia in suppressing STAT1 signaling and, thus, suppressing apoptosis. However, the exact mechanisms behind these observations still need to be elucidated. Since pharmacologic inhibition of EZH2 resulted in a marked increase in the anti-tumor response of AT/RT cells following *KIF3A* knockdown, this might be a first lead. For instance, further studies need to investigate whether specific transcription factors, miRNAs or lncRNAs are released following disruption of primary ciliogenesis that, in turn, lead to the suppression of EZH2 and the induction of STAT1 and its signaling cascade.

7 References

1. Brody, H. Brain cancer. *Nature* (2018). doi:10.1038/d41586-018-06703-8
2. Louis, D. N. *et al.* The 2016 World Health Organization Classification of Tumors of the Central Nervous System: a summary. *Acta Neuropathologica* (2016). doi:10.1007/s00401-016-1545-1
3. Capper, D. *et al.* DNA methylation-based classification of central nervous system tumours. *Nature* (2018). doi:10.1038/nature26000
4. Gröbner, S. N. *et al.* The landscape of genomic alterations across childhood cancers. *Nature* (2018). doi:10.1038/nature25480
5. Kaatsch, P., Grabow, D. & Spix, C. Deutsches Kinderkrebsregister Jahresbericht / Annual Report 2018 German Childhood Cancer Registry. 1–176 (2019).
6. Ostrom, Q. T. *et al.* CBTRUS statistical report: Primary brain and other central nervous system tumors diagnosed in the United States in 2011-2015. *Neuro-Oncology* (2018). doi:10.1093/neuonc/noy131
7. Collins, V. P., Jones, D. T. W. & Giannini, C. Pilocytic astrocytoma: pathology, molecular mechanisms and markers. *Acta Neuropathologica* (2015). doi:10.1007/s00401-015-1410-7
8. Taylor, M. D. *et al.* Molecular subgroups of medulloblastoma: The current consensus. *Acta Neuropathol.* (2012). doi:10.1007/s00401-011-0922-z
9. Cavalli, F. M. G. *et al.* Intertumoral Heterogeneity within Medulloblastoma Subgroups. *Cancer Cell* (2017). doi:10.1016/j.ccell.2017.05.005
10. Ginn, K. F. & Gajjar, A. Atypical Teratoid Rhabdoid Tumor: Current Therapy and Future Directions. *Front. Oncol.* (2012). doi:10.3389/fonc.2012.00114
11. Rorke, L. B., Packer, R. J. & Biegel, J. A. Central nervous system atypical teratoid/rhabdoid tumors of infancy and childhood: definition of an entity. *J. Neurosurg.* (2009). doi:10.3171/jns.1996.85.1.0056
12. Frühwald, M. C., Biegel, J. A., Bourdeaut, F., Roberts, C. W. M. & Chi, S. N. Atypical teratoid/rhabdoid tumors - Current concepts, advances in biology, and potential future therapies. *Neuro-Oncology* (2016). doi:10.1093/neuonc/nov264
13. Zarovnaya, E. L. *et al.* Atypical teratoid/rhabdoid tumor of the spine in an adult: Case report and review of the literature. *J. Neurooncol.* (2007). doi:10.1007/s11060-007-9339-x
14. Makuria, A. T. *et al.* Atypical teratoid rhabdoid tumor (AT/RT) in adults: Review of four cases. *J. Neurooncol.* (2008). doi:10.1007/s11060-008-9571-z
15. Chacko, G. *et al.* Atypical teratoid/rhabdoid tumor arising in the setting of a pleomorphic xanthoastrocytoma. *J. Neurooncol.* (2007). doi:10.1007/s11060-007-9361-z
16. Kleinschmidt-Demasters, B. K., Birks, D. K., Aisner, D. L., Hankinson, T. C. &

Rosenblum, M. K. Atypical teratoid/rhabdoid tumor arising in a ganglioglioma: Genetic characterization. *Am. J. Surg. Pathol.* (2011). doi:10.1097/PAS.0b013e3182382a3f

17. Gorayski, P., Boros, S., Ong, B., Olson, S. & Foote, M. Radiation-induced primary cerebral atypical teratoid/rhabdoid tumour in an adult. *J. Clin. Neurosci.* (2013). doi:10.1016/j.jocn.2013.03.041
18. Oliveira, E., Lavrador, J. P., Roque, L., Pimentel, J. & Miguéns, J. Atypical teratoid/rhabdoid tumour following craniopharyngioma radiotherapy during childhood. *Child's Nervous System* (2016). doi:10.1007/s00381-016-3187-y
19. Lau, C. S. M., Mahendraraj, K. & Chamberlain, R. S. Atypical teratoid rhabdoid tumors: A population-based clinical outcomes study involving 174 patients from the Surveillance, Epidemiology, and End Results database (1973–2010). *Cancer Manag. Res.* (2015). doi:10.2147/CMAR.S88561
20. Burger, P. C. *et al.* Atypical teratoid/rhabdoid tumor of the central nervous system: A highly malignant tumor of infancy and childhood frequently mistaken for medulloblastoma: A Pediatric Oncology Group study. *Am. J. Surg. Pathol.* (1998). doi:10.1097/00000478-199809000-00007
21. Meyers, S. P. *et al.* Primary intracranial atypical teratoid/rhabdoid tumors of infancy and childhood: MRI features and patient outcomes. *Am. J. Neuroradiol.* (2006).
22. Warmuth-Metz, M. *et al.* CT and MR imaging in atypical teratoid/rhabdoid tumors of the central nervous system. *Neuroradiology* (2008). doi:10.1007/s00234-008-0369-7
23. Biegel, J. A. Molecular genetics of atypical teratoid/rhabdoid tumor. *Neurosurgical focus* (2006).
24. Haberler, C. *et al.* Immunohistochemical analysis of INI1 protein in malignant pediatric CNS tumors: Lack of INI1 in atypical teratoid/rhabdoid tumors and in a fraction of primitive neuroectodermal tumors without rhabdoid phenotype. *Am. J. Surg. Pathol.* (2006). doi:10.1097/01.pas.0000213329.71745.ef
25. Hasselblatt, M. *et al.* SMARCA4-mutated atypical teratoid/rhabdoid tumors are associated with inherited germline alterations and poor prognosis. *Acta Neuropathologica* (2014). doi:10.1007/s00401-014-1323-x
26. Hilden, J. M. *et al.* Central nervous system atypical teratoid/rhabdoid tumor: Results of therapy in children enrolled in a registry. *J. Clin. Oncol.* (2004). doi:10.1200/JCO.2004.07.073
27. Tekautz, T. M. *et al.* Atypical teratoid/rhabdoid tumors (ATRT): Improved survival in children 3 years of age and older with radiation therapy and high-dose alkylator-based chemotherapy. *Journal of Clinical Oncology* (2005). doi:10.1200/JCO.2005.05.187
28. Dufour, C. *et al.* Clinicopathologic prognostic factors in childhood atypical teratoid

and rhabdoid tumor of the central nervous system: A multicenter study. *Cancer* (2012). doi:10.1002/cncr.26684

29. Athale, U. H., Duckworth, J., Odame, I. & Barr, R. Childhood atypical teratoid rhabdoid tumor of the central nervous system: A meta-analysis of observational studies. *J. Pediatr. Hematol. Oncol.* (2009). doi:10.1097/MPH.0b013e3181b258a9
30. Buscariollo, D. L., Park, H. S., Roberts, K. B. & Yu, J. B. Survival outcomes in atypical teratoid rhabdoid tumor for patients undergoing radiotherapy in a Surveillance, Epidemiology, and End Results analysis. *Cancer* (2012). doi:10.1002/cncr.27373
31. Kralik, S. F. *et al.* Radiation necrosis in pediatric patients with brain tumors treated with proton radiotherapy. *Am. J. Neuroradiol.* (2015). doi:10.3174/ajnr.A4333
32. Richardson, E. A., Ho, B. & Huang, A. Atypical teratoid rhabdoid tumour: From tumours to therapies. *Journal of Korean Neurosurgical Society* (2018). doi:10.3340/jkns.2018.0061
33. Knutson, S. K. *et al.* Durable tumor regression in genetically altered malignant rhabdoid tumors by inhibition of methyltransferase EZH2. *Proc. Natl. Acad. Sci. U. S. A.* (2013). doi:10.1073/pnas.1303800110
34. Unland, R. *et al.* Analysis of the antiproliferative effects of 3-deazaneoplanocin A in combination with standard anticancer agents in rhabdoid tumor cell lines. *Anticancer. Drugs* (2015). doi:10.1097/CAD.0000000000000181
35. Kerl, K., Holsten, T. & Frühwald, M. C. Rhabdoid tumors: Clinical approaches and molecular targets for innovative therapy. *Pediatric Hematology and Oncology* (2013). doi:10.3109/08880018.2013.791737
36. Tang, Y. *et al.* Epigenetic targeting of Hedgehog pathway transcriptional output through BET bromodomain inhibition. *Nat. Med.* (2014). doi:10.1038/nm.3613
37. Knipstein, J. A. *et al.* Histone deacetylase inhibition decreases proliferation and potentiates the effect of ionizing radiation in atypical teratoid/rhabdoid tumor cells. *Neuro. Oncol.* (2012). doi:10.1093/neuonc/nor208
38. Torchia, J. *et al.* Integrated (epi)-Genomic Analyses Identify Subgroup-Specific Therapeutic Targets in CNS Rhabdoid Tumors. *Cancer Cell* (2016). doi:10.1016/j.ccell.2016.11.003
39. Tsikitis, M., Zhang, Z., Edelman, W., Zagzag, D. & Kalpana, G. V. Genetic ablation of Cyclin D1 abrogates genesis of rhabdoid tumors resulting from Ini1 loss. *Proc. Natl. Acad. Sci. U. S. A.* (2005). doi:10.1073/pnas.0505300102
40. Smith, M. E. *et al.* Therapeutically targeting cyclin D1 in primary tumors arising from loss of Ini1. *Proc. Natl. Acad. Sci. U. S. A.* (2011). doi:10.1073/pnas.0913297108
41. Venkataraman, S. *et al.* Targeting Aurora Kinase A enhances radiation sensitivity of atypical teratoid rhabdoid tumor cells. *J. Neurooncol.* (2012). doi:10.1007/s11060-011-0795-y
42. Wetmore, C. *et al.* Alisertib is active as single agent in recurrent atypical teratoid

rhabdoid tumors in 4 children. *Neuro. Oncol.* (2015). doi:10.1093/neuonc/nov017
43. Koos, B. *et al.* The tyrosine kinase c-Abl promotes proliferation and is expressed in atypical teratoid and malignant rhabdoid tumors. *Cancer* (2010). doi:10.1002/cncr.25420
44. Jayanthan, A., Bernoux, D., Bose, P., Riabowol, K. & Narendran, A. Multi-tyrosine kinase inhibitors in preclinical studies for pediatric CNS AT/RT: Evidence for synergy with Topoisomerase-I inhibition. *Cancer Cell Int.* (2011). doi:10.1186/1475-2867-11-44
45. D'cunja, J. *et al.* Antisense treatment of IGF-IR induces apoptosis and enhances chemosensitivity in central nervous system atypical teratoid/rhabdoid tumours cells. *Eur. J. Cancer* (2007). doi:10.1016/j.ejca.2007.03.003
46. Hanahan, D. & Weinberg, R. A. Hallmarks of cancer: The next generation. *Cell* (2011). doi:10.1016/j.cell.2011.02.013
47. McLendon, R. *et al.* Comprehensive genomic characterization defines human glioblastoma genes and core pathways. *Nature* (2008). doi:10.1038/nature07385
48. Bell, D. *et al.* Integrated genomic analyses of ovarian carcinoma. *Nature* (2011). doi:10.1038/nature10166
49. Lee, R. S. *et al.* A remarkably simple genome underlies highly malignant pediatric rhabdoid cancers. *J. Clin. Invest.* (2012). doi:10.1172/JCI64400
50. Versteege, I. *et al.* Truncating mutations of hSNF5/INI1 in aggressive paediatric cancer. *Nature* (1998). doi:10.1038/28212
51. Biegel, J. A. *et al.* Germ-line and acquired mutations of INI1 in atypical teratoid and rhabdoid tumors. *Cancer Res.* (1999).
52. Wilson, B. G. & Roberts, C. W. M. SWI/SNF nucleosome remodellers and cancer. *Nature Reviews Cancer* (2011). doi:10.1038/nrc3068
53. Wang, W. *et al.* Purification and biochemical heterogeneity of the mammalian SWI-SNF complex. *EMBO J.* (1996). doi:10.1002/j.1460-2075.1996.tb00921.x
54. Helming, K. C., Wang, X. & Roberts, C. W. M. Vulnerabilities of mutant SWI/SNF complexes in cancer. *Cancer Cell* (2014). doi:10.1016/j.ccr.2014.07.018
55. Hu, G. *et al.* Regulation of nucleosome landscape and transcription factor targeting at tissue-specific enhancers by BRG1. *Genome Res.* (2011). doi:10.1101/gr.121145.111
56. Tolstorukov, M. Y. *et al.* Swi/Snf chromatin remodeling/tumor suppressor complex establishes nucleosome occupancy at target promoters. *Proc. Natl. Acad. Sci. U. S. A.* (2013). doi:10.1073/pnas.1302209110
57. You, J. S. *et al.* SNF5 Is an Essential Executor of Epigenetic Regulation during Differentiation. *PLoS Genet.* (2013). doi:10.1371/journal.pgen.1003459
58. Wilson, B. G. *et al.* Epigenetic antagonism between polycomb and SWI/SNF complexes during oncogenic transformation. *Cancer Cell* (2010). doi:10.1016/j.ccr.2010.09.006

59. Sredni, S. T. & Tomita, T. Rhabdoid Tumor Predisposition Syndrome. *Pediatr. Dev. Pathol.* (2015). doi:10.2350/14-07-1531-misc.1
60. Kadoch, C. *et al.* Proteomic and bioinformatic analysis of mammalian SWI/SNF complexes identifies extensive roles in human malignancy. *Nat. Genet.* (2013). doi:10.1038/ng.2628
61. Johann, P. D. *et al.* Atypical Teratoid/Rhabdoid Tumors Are Comprised of Three Epigenetic Subgroups with Distinct Enhancer Landscapes. *Cancer Cell* (2016). doi:10.1016/j.ccell.2016.02.001
62. Dobell, C. & Leeuwenhoek, A. van. *Antony van Leeuwenhoek and his 'Little animals'; being some account of the father of protozoology and bacteriology and his multifarious discoveries in these disciplines; collected, translated, and edited from his printed works, unpublished manuscripts, an* (2011). doi:10.5962/bhl.title.13354
63. Fabricius, O., Müller, C. F. & Müller, O. F. *Animalcula infusoria fluviatilia et marina / quae detexit, systematice descripsit et ad vivum delineari curavit Otho Fridericus Müller ... ; sistit opus hoc posthumum quod cum tabulis aeneis L. in lucem tradit vidua ejus nobilissima cura Othonis* (2011). doi:10.5962/bhl.title.47041
64. Reiter, J. F. & Leroux, M. R. Genes and molecular pathways underpinning ciliopathies. *Nature Reviews Molecular Cell Biology* (2017). doi:10.1038/nrm.2017.60
65. Ishikawa, H. & Marshall, W. F. Ciliogenesis: Building the cell's antenna. *Nature Reviews Molecular Cell Biology* (2011). doi:10.1038/nrm3085
66. Malicki, J. J. & Johnson, C. A. The Cilium: Cellular Antenna and Central Processing Unit. *Trends in Cell Biology* (2017). doi:10.1016/j.tcb.2016.08.002
67. Mirvis, M., Stearns, T. & Nelson, W. J. Cilium structure, assembly, and disassembly regulated by the cytoskeleton. *Biochemical Journal* (2018). doi:10.1042/BCJ20170453
68. Plotnikova, O. V., Pugacheva, E. N. & Golemis, E. A. Primary cilia and the cell cycle. *Methods Cell Biol.* (2009). doi:10.1016/S0091-679X(08)94007-3
69. SOROKIN, S. Centrioles and the formation of rudimentary cilia by fibroblasts and smooth muscle cells. *J. Cell Biol.* (1962). doi:10.1083/jcb.15.2.363
70. Sorokin, S. P. Reconstructions of centriole formation and ciliogenesis in mammalian lungs. *J. Cell Sci.* (1968).
71. Pedersen, L. B. & Rosenbaum, J. L. Chapter Two Intraflagellar Transport (IFT). Role in Ciliary Assembly, Resorption and Signalling. *Current Topics in Developmental Biology* (2008). doi:10.1016/S0070-2153(08)00802-8
72. Hao, L. & Scholey, J. M. Intraflagellar transport at a glance. *J. Cell Sci.* (2009). doi:10.1242/jcs.023861
73. Rosenbaum, J. L. & Witman, G. B. Intraflagellar transport. *Nature Reviews Molecular Cell Biology* (2002). doi:10.1038/nrm952

74. Mourão, A., Christensen, S. T. & Lorentzen, E. The intraflagellar transport machinery in ciliary signaling. *Current Opinion in Structural Biology* (2016). doi:10.1016/j.sbi.2016.06.009
75. Ishikawa, H. & Marshall, W. F. Intraflagellar transport and ciliary dynamics. *Cold Spring Harb. Perspect. Biol.* (2017). doi:10.1101/cshperspect.a021998
76. Prevo, B., Scholey, J. M. & Peterman, E. J. G. Intraflagellar transport: mechanisms of motor action, cooperation, and cargo delivery. *FEBS Journal* (2017). doi:10.1111/febs.14068
77. Gerdes, J. M., Davis, E. E. & Katsanis, N. The Vertebrate Primary Cilium in Development, Homeostasis, and Disease. *Cell* (2009). doi:10.1016/j.cell.2009.03.023
78. Fry, A. M., Leaper, M. J. & Bayliss, R. The primary cilium: Guardian of organ development and homeostasis. *Organogenesis* (2014). doi:10.4161/org.28910
79. Youn, Y. H. & Han, Y. G. Primary Cilia in Brain Development and Diseases. *American Journal of Pathology* (2018). doi:10.1016/j.ajpath.2017.08.031
80. Hildebrandt, F., Benzing, T. & Katsanis, N. Ciliopathies. *New England Journal of Medicine* (2011). doi:10.1056/NEJMra1010172
81. Tan, A. Y., Blumenfeld, J. & Rennert, H. Polycystic kidney disease. in *Molecular Pathology in Clinical Practice:Second Edition* (2016). doi:10.1007/978-3-319-19674-9_19
82. Suspitsin, E. N. & Imyanitov, E. N. Bardet-Biedl Syndrome. *Molecular Syndromology* (2016). doi:10.1159/000445491
83. Louis-Jacques, A. F. & Odibo, A. O. Meckel-Gruber Syndrome. in *Obstetric Imaging: Fetal Diagnosis and Care: Second Edition* (2017). doi:10.1016/B978-0-323-44548-1.00133-9
84. Crawford, D. & Dearmun, A. Joubert syndrome. *Nurs. Child. Young People* (2017). doi:10.7748/ncyp.29.5.15.s19
85. Anvarian, Z., Mykytyn, K., Mukhopadhyay, S., Pedersen, L. B. & Christensen, S. T. Cellular signalling by primary cilia in development, organ function and disease. *Nature Reviews Nephrology* (2019). doi:10.1038/s41581-019-0116-9
86. Eguether, T. & Hahne, M. Mixed signals from the cell's antennae: primary cilia in cancer. *EMBO Rep.* (2018). doi:10.15252/embr.201846589
87. Wheway, G., Nazlamova, L. & Hancock, J. T. Signaling through the primary cilium. *Frontiers in Cell and Developmental Biology* (2018). doi:10.3389/fcell.2018.00008
88. Huangfu, D. *et al.* Hedgehog signalling in the mouse requires intraflagellar transport proteins. *Nature* (2003). doi:10.1038/nature02061
89. Corbit, K. C. *et al.* Vertebrate Smoothened functions at the primary cilium. *Nature* (2005). doi:10.1038/nature04117
90. Haycraft, C. J. *et al.* Gli2 and Gli3 localize to cilia and require the intraflagellar transport protein polaris for processing and function. *PLoS Genet.* (2005).

91. Rohatgi, R. & Scott, M. P. Patching the gaps in Hedgehog signalling. *Nat. Cell Biol.* (2007). doi:10.1038/ncb435
92. Ocbina, P. J. R., Tuson, M. & Anderson, K. V. Primary cilia are not required for normal canonical Wnt signaling in the mouse embryo. *PLoS One* (2009). doi:10.1371/journal.pone.0006839
93. Pak, E. & Segal, R. A. Hedgehog Signal Transduction: Key Players, Oncogenic Drivers, and Cancer Therapy. *Developmental Cell* (2016). doi:10.1016/j.devcel.2016.07.026
94. Corbit, K. C. *et al.* Kif3a constrains β-catenin-dependent Wnt signalling through dual ciliary and non-ciliary mechanisms. *Nat. Cell Biol.* (2008). doi:10.1038/ncb1670
95. Wallingford, J. B. & Mitchell, B. Strange as it may seem: The many links between Wnt signaling, planar cell polarity, and cilia. *Genes and Development* (2011). doi:10.1101/gad.2008011
96. Elliott, K. H. & Brugmann, S. A. Sending mixed signals: Cilia-dependent signaling during development and disease. *Developmental Biology* (2019). doi:10.1016/j.ydbio.2018.03.007
97. Daulat, A. M. & Borg, J. P. Wnt/Planar Cell Polarity Signaling: New Opportunities for Cancer Treatment. *Trends in Cancer* (2017). doi:10.1016/j.trecan.2017.01.001
98. Ezratty, E. J. *et al.* A role for the primary cilium in notch signaling and epidermal differentiation during skin development. *Cell* (2011). doi:10.1016/j.cell.2011.05.030
99. Grisanti, L., Revenkova, E., Gordon, R. E. & Iomini, C. Primary cilia maintain corneal epithelial homeostasis by regulation of the Notch signaling pathway. *Dev.* (2016). doi:10.1242/dev.132704
100. Liu, Z. *et al.* Primary cilia regulate hematopoietic stem and progenitor cell specification through Notch signaling in zebrafish. *Nat. Commun.* (2019). doi:10.1038/s41467-019-09403-7
101. Stasiulewicz, M. *et al.* A conserved role for Notch signaling in priming the cellular response to Shh through ciliary localisation of the key Shh transducer Smo. *Development* (2015). doi:10.1242/dev.125237
102. Christensen, S. T., Clement, C. A., Satir, P. & Pedersen, L. B. Primary cilia and coordination of receptor tyrosine kinase (RTK) signalling. *Journal of Pathology* (2012). doi:10.1002/path.3004
103. Schneider, L., Clement, C. & Teilmann, S. PDGFRaa signalling is regulated through the primary cilium in fibroblasts. *Submitt. Publ.* (2006). doi:10.1016/j.cub.2005.09.012
104. Clement, C. A. *et al.* TGF-β Signaling Is Associated with Endocytosis at the Pocket Region of the Primary Cilium. *Cell Rep.* (2013). doi:10.1016/j.celrep.2013.05.020
105. Han, Y. G. *et al.* Dual and opposing roles of primary cilia in medulloblastoma

development. *Nat. Med.* (2009). doi:10.1038/nm.2020
106. Wong, S. Y. *et al.* Primary cilia can both mediate and suppress Hedgehog pathway-dependent tumorigenesis. *Nat. Med.* (2009). doi:10.1038/nm.2011
107. Conduit, S. E. *et al.* A compartmentalized phosphoinositide signaling axis at cilia is regulated by INPP5E to maintain cilia and promote Sonic Hedgehog medulloblastoma. *Oncogene* (2017). doi:10.1038/onc.2017.208
108. N., Y. *et al.* INTU is essential for oncogenic Hh signaling through regulating primary cilia formation in basal cell carcinoma. *Oncogene* (2017). doi:10.1038/onc.2017.117
109. Sarkisian, M. R. *et al.* Detection of primary cilia in human glioblastoma. *J. Neurooncol.* (2014). doi:10.1007/s11060-013-1340-y
110. Moser, J. J., Fritzler, M. J. & Rattner, J. B. Primary ciliogenesis defects are associated with human astrocytoma/glioblastoma cells. *BMC Cancer* (2009). doi:10.1186/1471-2407-9-448
111. Moser, J. J., Fritzler, M. J. & Rattner, J. B. Ultrastructural characterization of primary cilia in pathologically characterized human glioblastoma multiforme (GBM) tumors. *BMC Clin. Pathol.* (2014). doi:10.1186/1472-6890-14-40
112. Yang, Y., Roine, N. & Mäkelä, T. P. CCRK depletion inhibits glioblastoma cell proliferation in a cilium-dependent manner. *EMBO Rep.* (2013). doi:10.1038/embor.2013.80
113. Loskutov, Y. V. *et al.* LPA signaling is regulated through the primary cilium: A novel target in glioblastoma. *Oncogene* (2018). doi:10.1038/s41388-017-0049-3
114. Li, L. *et al.* Sonic Hedgehog promotes proliferation of Notch-dependent monociliated choroid plexus tumour cells. *Nat. Cell Biol.* (2016). doi:10.1038/ncb3327
115. Kim, J., Dabiri, S. & Seeley, E. S. Primary cilium depletion typifies cutaneous melanoma in situ and malignant melanoma. *PLoS One* (2011). doi:10.1371/journal.pone.0027410
116. Zingg, D. *et al.* EZH2-Mediated Primary Cilium Deconstruction Drives Metastatic Melanoma Formation. *Cancer Cell* (2018). doi:10.1016/j.ccell.2018.06.001
117. Yuan, K. *et al.* Primary cilia are decreased in breast cancer: Analysis of a collection of human breast cancer cell lines and tissues. *J. Histochem. Cytochem.* (2010). doi:10.1369/jhc.2010.955856
118. Menzl, I. *et al.* Loss of primary cilia occurs early in breast cancer development. *Cilia* (2014). doi:10.1186/2046-2530-3-7
119. Guen, V. J. *et al.* EMT programs promote basal mammary stem cell and tumor-initiating cell stemness by inducing primary ciliogenesis and Hedgehog signaling. *Proc. Natl. Acad. Sci.* (2017). doi:10.1073/pnas.1711534114
120. Bailey, J. M., Mohr, A. M. & Hollingsworth, M. A. Sonic hedgehog paracrine signaling regulates metastasis and lymphangiogenesis in pancreatic cancer.

Oncogene (2009). doi:10.1038/onc.2009.220

121. Seeley, E. S., Carrière, C., Goetze, T., Longnecker, D. S. & Korc, M. Pancreatic cancer and precursor pancreatic intraepithelial neoplasia lesions are devoid of primary cilia. *Cancer Res.* (2009). doi:10.1158/0008-5472.CAN-08-1290
122. Emoto, K. *et al.* Presence of primary cilia in cancer cells correlates with prognosis of pancreatic ductal adenocarcinoma. *Hum. Pathol.* (2014). doi:10.1016/j.humpath.2013.11.017
123. Kobayashi, T. *et al.* HDAC2 promotes loss of primary cilia in pancreatic ductal adenocarcinoma. *EMBO Rep.* (2017). doi:10.15252/embr.201541922
124. Schraml, P. *et al.* Sporadic clear cell renal cell carcinoma but not the papillary type is characterized by severely reduced frequency of primary cilia. *Mod. Pathol.* (2009). doi:10.1038/modpathol.2008.132
125. Dere, R., Perkins, A. L., Bawa-Khalfe, T., Jonasch, D. & Walker, C. L. β -Catenin Links von Hippel-Lindau to Aurora Kinase A and Loss of Primary Cilia in Renal Cell Carcinoma . *J. Am. Soc. Nephrol.* (2015). doi:10.1681/asn.2013090984
126. Egeberg, D. L. *et al.* Primary cilia and aberrant cell signaling in epithelial ovarian cancer. *Cilia* (2012). doi:10.1186/2046-2530-1-15
127. Dvorak, J. *et al.* Prognostic significance of the frequency of primary cilia in cells of small bowel and colorectal adenocarcinoma. *J. B.U.ON.* (2016).
128. Dvorak, J. *et al.* Association of the combined parameters including the frequency of primary cilia, CD8+ tumor infiltrating lymphocytes and PD-1 expression with the outcome in intestinal cancer. *Journal of B.U.ON.* (2017).
129. Hassounah, N. B. *et al.* Primary Cilia Are Lost in Preinvasive and Invasive Prostate Cancer. *PLoS One* (2013). doi:10.1371/journal.pone.0068521
130. Fu, W., Asp, P., Canter, B. & Dynlacht, B. D. Primary cilia control hedgehog signaling during muscle differentiation and are deregulated in rhabdomyosarcoma. *Proc. Natl. Acad. Sci.* (2014). doi:10.1073/pnas.1323265111
131. Ho, L. *et al.* Primary cilia attenuate hedgehog signalling in neoplastic chondrocytes. *Oncogene* (2013). doi:10.1038/onc.2012.588
132. Hannus, M. *et al.* SiPools: Highly complex but accurately defined siRNA pools eliminate off-target effects. *Nucleic Acids Res.* (2014). doi:10.1093/nar/gku480
133. Qi, L. S. *et al.* Repurposing CRISPR as an RNA-γuided platform for sequence-specific control of gene expression. *Cell* (2013). doi:10.1016/j.cell.2013.02.022
134. Bradford, M. M. A rapid and sensitive method for the quantitation of microgram quantities of protein utilizing the principle of protein-dye binding. *Anal. Biochem.* (1976). doi:10.1016/0003-2697(76)90527-3
135. Poschmann, G. *et al.* High-fat diet induced isoform changes of the Parkinson's disease protein DJ-1. *J. Proteome Res.* (2014). doi:10.1021/pr401157k
136. Barakat, M. T., Humke, E. W. & Scott, M. P. Kif3a is necessary for initiation and maintenance of medulloblastoma. *Carcinogenesis* (2013).

doi:10.1093/carcin/bgt041
137. Hoang-Minh, L. B. *et al.* Disruption of KIF3A in patient-derived glioblastoma cells: Effects on ciliogenesis, hedgehog sensitivity, and tumorigenesis. *Oncotarget* (2016). doi:10.18632/oncotarget.6854
138. Mirvis, M., Siemers, K. A., Nelson, W. J. & Stearns, T. P. Primary cilium loss in mammalian cells occurs predominantly by whole-cilium shedding. *PLoS Biol.* (2019). doi:10.1371/journal.pbio.3000381
139. Firestone, A. J. *et al.* Small-molecule inhibitors of the AAA+ ATPase motor cytoplasmic dynein. *Nature* (2012). doi:10.1038/nature10936
140. Jeibmann, A. *et al.* Identification of genes involved in the biology of atypical teratoid/rhabdoid tumours using Drosophila melanogaster. *Nat. Commun.* (2014). doi:10.1038/ncomms5005
141. Sainath, R. & Gallo, G. The dynein inhibitor Ciliobrevin D inhibits the bidirectional transport of organelles along sensory axons and impairs NGF-mediated regulation of growth cones and axon branches. *Dev. Neurobiol.* (2015). doi:10.1002/dneu.22246
142. Pinazza, M. *et al.* Histone deacetylase 6 controls Notch3 trafficking and degradation in T-cell acute lymphoblastic leukemia cells. *Oncogene* (2018). doi:10.1038/s41388-018-0234-z
143. Mirzoyan, Z. *et al.* Drosophila melanogaster: A model organism to study cancer. *Frontiers in Genetics* (2019). doi:10.3389/fgene.2019.00051
144. Ugur, B., Chen, K. & Bellen, H. J. Drosophila tools and assays for the study of human diseases. *DMM Disease Models and Mechanisms* (2016). doi:10.1242/dmm.023762
145. Jana, S. C., Girotra, M. & Ray, K. Heterotrimeric kinesin-II is necessary and sufficient to promote different stepwise assembly of morphologically distinct bipartite cilia in Drosophila antenna. *Mol. Biol. Cell* (2011). doi:10.1091/mbc.E10-08-0712
146. Jana, S. C., Bettencourt-Dias, M., Durand, B. & Megraw, T. L. Drosophila melanogaster as a model for basal body research. *Cilia* (2016). doi:10.1186/s13630-016-0041-5
147. Han, Y. G., Kwok, B. H. & Kernan, M. J. Intraflagellar Transport Is Required in Drosophila to Differentiate Sensory Cilia but Not Sperm. *Curr. Biol.* (2003). doi:10.1016/j.cub.2003.08.034
148. Kuzhandaivel, A., Schultz, S. W., Alkhori, L. & Alenius, M. Cilia-Mediated Hedgehog Signaling in Drosophila. *Cell Rep.* (2014). doi:10.1016/j.celrep.2014.03.052
149. De Andrea, M., Ravera, R., Gioia, D., Gariglio, M. & Landolfo, S. The interferon system: An overview. *European Journal of Paediatric Neurology* (2002). doi:10.1053/ejpn.2002.0573
150. Levy, D. E. & Darnell, J. E. STATs: Transcriptional control and biological impact.

Nature Reviews Molecular Cell Biology (2002). doi:10.1038/nrm909

151. Bromberg, J. F. Activation of STAT proteins and growth control. *BioEssays* (2001). doi:10.1002/1521-1878(200102)23:2<161::AID-BIES1023>3.0.CO;2-0
152. Battle, T. & Frank, D. The Role of STATs in Apoptosis. *Curr. Mol. Med.* (2005). doi:10.2174/1566524023362456
153. Ihle, J. N. The Stat family in cytokine signaling. *Current Opinion in Cell Biology* (2001). doi:10.1016/S0955-0674(00)00199-X
154. Kovarik, P. *et al.* Specificity of signaling by STAT1 depends on SH2 and C-terminal domains that regulate Ser727 phosphorylation, differentially affecting specific target gene expression. *EMBO J.* (2001). doi:10.1093/emboj/20.1.91
155. Ramana, C. V., Gil, M. P., Schreiber, R. D. & Stark, G. R. Stat1-dependent and -independent pathways in IFN-γ-dependent signaling. *Trends in Immunology* (2002). doi:10.1016/S1471-4906(01)02118-4
156. Meissl, K., Macho-Maschler, S., Müller, M. & Strobl, B. The good and the bad faces of STAT1 in solid tumours. *Cytokine* (2017). doi:10.1016/j.cyto.2015.11.011
157. Gordziel, C., Bratsch, J., Moriggl, R., Knösel, T. & Friedrich, K. Both STAT1 and STAT3 are favourable prognostic determinants in colorectal carcinoma. *Br. J. Cancer* (2013). doi:10.1038/bjc.2013.274
158. Chen, G., Wang, H., Xie, S., Ma, J. & Wang, G. STAT1 negatively regulates hepatocellular carcinoma cell proliferation. *Oncol. Rep.* (2013). doi:10.3892/or.2013.2398
159. Zhang, Y., Molavi, O., Su, M. & Lai, R. The clinical and biological significance of STAT1 in esophageal squamous cell carcinoma. *BMC Cancer* (2014). doi:10.1186/1471-2407-14-791
160. Sun, Y., Yang, S., Sun, N. & Chen, J. Differential expression of STAT1 and p21 proteins predicts pancreatic cancer progression and prognosis. *Pancreas* (2014). doi:10.1097/MPA.0000000000000074
161. Takahashi, A. *et al.* Analysis of gene expression profiles of soft tissue sarcoma using a combination of knowledge-based filtering with integration of multiple statistics. *PLoS One* (2014). doi:10.1371/journal.pone.0106801
162. Osborn, J. L. & Greer, S. F. Metastatic melanoma cells evade immune detection by silencing STAT1. *Int. J. Mol. Sci.* (2015). doi:10.3390/ijms16024343
163. Hobeika, A. C., Etienne, W., Torres, B. A., Johnson, H. M. & Subramaniam, P. S. IFN-γ induction of p21(WAF1) is required for cell cycle inhibition and suppression of apoptosis. *J. Interf. Cytokine Res.* (1999). doi:10.1089/107999099312812
164. Dimco, G., Knight, R. A., Latchman, D. S. & Stephanou, A. STAT1 interacts directly with cyclin D1/Cdk4 and mediates cell cycle arrest. *Cell Cycle* (2010). doi:10.4161/cc.9.23.13955
165. Mandal, M., Bandyopadhyay, D., Goepfert, T. M. & Kumar, R. Interferon-induces expression of cyclin-dependent kinase-inhibitors p21(WAF1) and p27(Kip1) that

prevent activation of cyclin-dependent kinase by CDK-activating kinase (CAK). *Oncogene* (1998). doi:10.1038/sj.onc.1201529

166. Ossina, N. K. *et al.* Interferon-γ modulates a p53-independent apoptotic pathway and apoptosis-related gene expression. *J. Biol. Chem.* (1997). doi:10.1074/jbc.272.26.16351
167. Chin, Y. E., Kitagawa, M., Kuida, K., Flavell, R. A. & Fu, X. Y. Activation of the STAT signaling pathway can cause expression of caspase 1 and apoptosis. *Mol. Cell. Biol.* (1997). doi:10.1128/mcb.17.9.5328
168. Kumar, A., Commane, M., Flickinger, T. W., Horvath, C. M. & Stark, G. R. Defective TNF-α-induced apoptosis in STAT1-null cells due to low constitutive levels of caspases. *Science (80-.).* (1997). doi:10.1126/science.278.5343.1630
169. Shin, E. C. *et al.* IFN-γ induces cell death in human hepatoma cells through a trail/death receptor-mediated apoptotic pathway. *Int. J. Cancer* (2001). doi:10.1002/ijc.1310
170. Miura, Y. *et al.* TRAIL expression up-regulated by interferon-γ via phosphorylation of STAT1 induces myeloma cell death. *Anticancer Res.* (2006).
171. Meng, R. D. & El-Deiry, W. S. P53-independent upregulation of KILLER/DR5 TRAIL receptor expression by glucocorticoids and interferon-γ. *Exp. Cell Res.* (2001). doi:10.1006/excr.2000.5073
172. Fallarino, F. & Gajewski, T. F. Cutting edge: differentiation of antitumor CTL in vivo requires host expression of Stat1. *J. Immunol.* (1999).
173. Lee, C.-K. *et al.* Distinct Requirements for IFNs and STAT1 in NK Cell Function. *J. Immunol.* (2000). doi:10.4049/jimmunol.165.7.3571
174. Putz, E. M. *et al.* CDK8-mediated STAT1-S727 phosphorylation restrains NK cell cytotoxicity and tumor surveillance. *Cell Rep.* (2013). doi:10.1016/j.celrep.2013.07.012
175. Leibowitz, M. S., Andrade Filho, P. A., Ferrone, S. & Ferris, R. L. Deficiency of activated STAT1 in head and neck cancer cells mediates TAP1-dependent escape from cytotoxic T lymphocytes. *Cancer Immunol. Immunother.* (2011). doi:10.1007/s00262-010-0961-7
176. Lee, C. K., Gimeno, R. & Levy, D. E. Differential regulation of constitutive major histocompatibility complex class I expression in T and B lymphocytes. *J. Exp. Med.* (1999). doi:10.1084/jem.190.10.1451
177. Vijay Shankaran *et al.* IFN gamma and lymphocytes prevent primary tumour development and shape tumour immunogenicity. *Nature* (2001).
178. Battle, T. E., Lynch, R. A. & Frank, D. A. Signal transducer and activator of transcription 1 activation in endothelial cells is a negative regulator of angiogenesis. *Cancer Res.* (2006). doi:10.1158/0008-5472.CAN-05-3612
179. Nielsen, S. R. *et al.* IL-27 Inhibits lymphatic endothelial cell proliferation by STAT1-regulated gene expression. *Microcirculation* (2013). doi:10.1111/micc.12055

180. Huang, S., Bucana, C. D., Van Arsdall, M. & Fidler, I. J. Stat1 negatively regulates angiogenesis, tumorigenicity and metastasis of tumor cells. *Oncogene* (2002). doi:10.1038/sj.onc.1205341
181. Otsuka, A. *et al.* Hedgehog pathway inhibitors promote adaptive immune responses in basal cell carcinoma. *Clin. Cancer Res.* (2015). doi:10.1158/1078-0432.CCR-14-2110
182. Wang, S. *et al.* The CPLANE protein Intu protects kidneys from ischemia-reperfusion injury by targeting STAT1 for degradation. *Nat. Commun.* (2018). doi:10.1038/s41467-018-03628-8
183. Wee, Z. N. *et al.* EZH2-mediated inactivation of IFN-γ-JAK-STAT1 signaling is an effective therapeutic target in MYC-driven prostate cancer. *Cell Rep.* (2014). doi:10.1016/j.celrep.2014.05.045
184. Glazer, R. I., Knode, M. C., Tseng, C. K. H., Haines, D. R. & Marquez, V. E. 3-deazaneplanocin A: A new inhibitor of S-adenosylhomocysteine synthesis and its effects in human colon carcinoma cells. *Biochem. Pharmacol.* (1986). doi:10.1016/0006-2952(86)90774-4
185. Fiskus, W. *et al.* Combined epigenetic therapy with the histone methyltransferase EZH2 inhibitor 3-deazaneplanocin A and the histone deacetylase inhibitor panobinostat against human AML cells. *Blood* (2009). doi:10.1182/blood-2009-03-213496
186. Kikuchi, J. *et al.* Epigenetic therapy with 3-deazaneplanocin A, an inhibitor of the histone methyltransferase EZH2, inhibits growth of non-small cell lung cancer cells. *Lung Cancer* (2012). doi:10.1016/j.lungcan.2012.08.003
187. Shen, L., Cui, J., Pang, Y. X., Ma, Y. H. & Liu, P. S. 3-deazaneplanocin A is a promising therapeutic agent for ovarian cancer cells. *Asian Pacific J. Cancer Prev.* (2013). doi:10.7314/APJCP.2013.14.5.2915
188. Akpa, C. A. *et al.* DZNep-mediated apoptosis in B-cell lymphoma is independent of the lymphoma type, EZH2 mutation status and MYC, BCL2 or BCL6 translocations. *PLoS One* (2019). doi:10.1371/journal.pone.0220681
189. Huang, R. *et al.* DZNep inhibits Hif-1α and Wnt signalling molecules to attenuate the proliferation and invasion of BGC-823 gastric cancer cells. *Oncol. Lett.* (2019). doi:10.3892/ol.2019.10769
190. Fabbri, L., Bost, F. & Mazure, N. M. Primary cilium in cancer hallmarks. *International Journal of Molecular Sciences* (2019). doi:10.3390/ijms20061336
191. Khan, N. A. *et al.* Identification of drugs that restore primary cilium expression in cancer cells. *Oncotarget* (2016). doi:10.18632/oncotarget.7198

8 Appendix

8.1 Abbreviations

µ	Micro
AT/RT	Atypical teratoid/rhabdoid tumor
AURKA	Aurora kinase A
BET	Bromo- and extra-terminal
BSA	Bovine serum albumin
CCND1	Cyclin D1
CDK	Cyclin-dependent kinase
cDNA	Complementary DNA
CNS	Central nervous system
CP	Choroid plexus
CTRL	Control
DMEM	Dulbecco´s Modified Eagle Medium
DMSO	Dimethylsulfoxide
DNA	Deoxyribonucleic acid
dNTP	Deoxyribonucleotide triphosphate
DR5	Death receptor 5
EtOH	Ethanol
EZH2	Enhancer of zeste homolog 2
FBS	Fetal bovine serum
FITC	Fluorescein isothiocyanate
g	Gramm
GAPDH	Glyceraldehyde 3-phosphate dehydrogenase

GLI	Glioma-associated oncogene
h	Hour
HDAC	Histone deacetylase
IC_{50}	Half maximal inhibitory concentration
IFI35	Interferon-induced protein 35
IFIT	Interferon-induced protein with tetratricopeptide repeats
IFT	Intraflagellar transport
IMDM	Iscove´s Modified Dulbecco Medium
ISG15	ISG15 ubiquitin like modifier
ITS	Insulin-Transferrin-Seleneous Acid
KIF3A	Kinesin family member 3 A
l	Liter
m	Milli
M	Mole
min	Minute
MITF	Melanocyte inducing transcription factor
mRNA	Messenger ribonucleic acid
MX1	MX dynamin like GTPase 1
OAS	2´-5´-Oligoadenylate synthetase
OSE	Ovarian surface epithelium
OTX2	Orthodenticle homeobox 2
PCR	Polymerase chain reaction
PDGFR	Platelet-derived growth factor receptor
PEI	Polyethylenimine
PGK1	Phosphoglycerate kinase 1
PI	Propidium iodide

PMD	Partially methylated domain
PRC2	Polycomb repressive complex 2
PTCH1	Patched 1
RNA	Ribonucleic acid
RT	Room temperature
RTK	Receptor tyrosine kinase
SDS-PAGE	Sodium dodecylsulfate polyacrylamide gel electrophoresis
SEM	Standard error of mean
sgRNA	Single guide RNA
SHH	Sonic hedgehog
shRNA	Short hairpin RNA
siRNA	Small interfering RNA
SMARCA4	SWI/SNF related matrix associated actin dependent regulator of chromatin subfamily a member 4
SMARCB1	SWI/SNF related matrix associated actin dependent regulator of chromatin subfamily b member 1
SMO	Smoothened
STAT1	Signal transducer and activator of transcription 1
TGF-beta	Transforming growth factor-beta
TYR	Tyrosinase
WGBS	Whole genome bisulfite sequencing
WGS	Whole genome sequencing
WHO	World Health Organization
WNT	Wingless
xg	Times gravity

8.2 Supplementary figures and tables

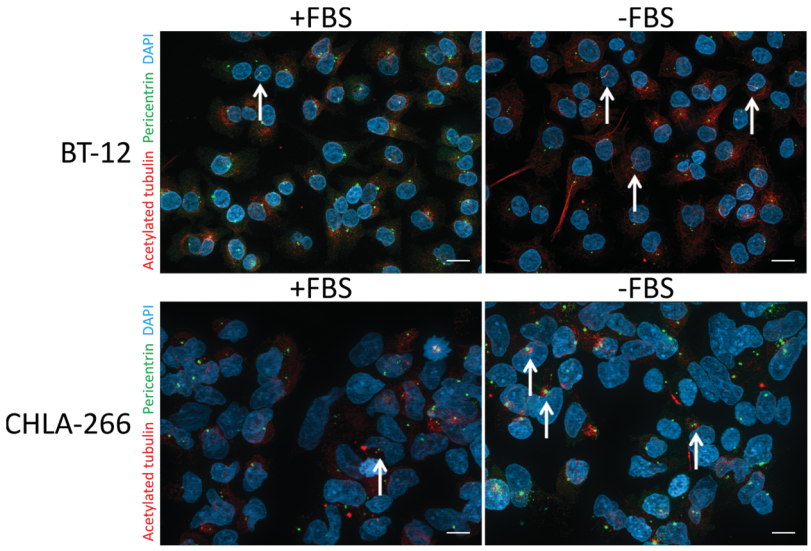

Supplementary figure 1: Serum starvation promotes primary ciliogenesis in the AT/RT cell lines BT-12 and CHLA-266. For serum starvation experiments, BT-12 and CHLA-266 cells were seeded in complete medium. The next day, complete medium was replaced either with complete medium again (+fetal bovine serum (FBS)) or with medium lacking serum (-FBS) for 72 h. Representative immunofluorescence images showing stainings for Pericentrin (green) and Acetylated tubulin (red), detecting the basal body and the axoneme of the primary cilium, respectively. Nuclei were counterstained with 4´,6-diamidin-2-phenylindol (DAPI, blue). Arrows indicate primary cilia. The scale bar corresponds to 20 µm.

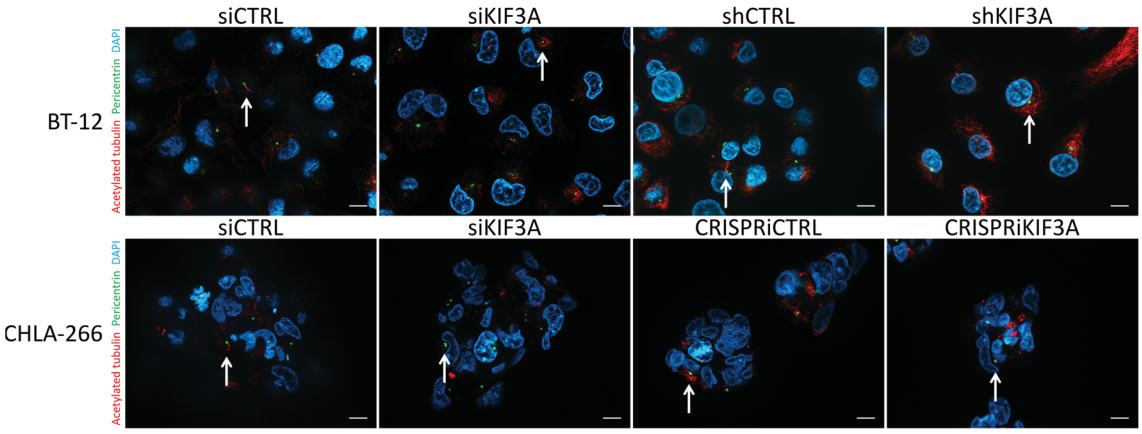

Supplementary figure 2: Knockdown of *kinesin family member 3A (KIF3A)* disrupts primary ciliogenesis in the AT/RT cell lines BT-12 and CHLA-266. Transient knockdown of *KIF3A* was achieved using siPOOLs. Stable knockdown of *KIF3A* was achieved using shRNA-based (BT-12) or CRISPRi-based (CHLA-266) technology. Representative immunofluorescence images showing stainings for Pericentrin (green) and Acetylated tubulin (red), detecting the basal body and the axoneme of the primary cilium, respectively. Nuclei were counterstained with 4´,6-diamidin-2-phenylindol (DAPI, blue). Arrows indicate either primary cilia in the control cells or disrupted primary ciliogenesis in the *KIF3A* knockdown cells. The scale bar corresponds to 10 µm.

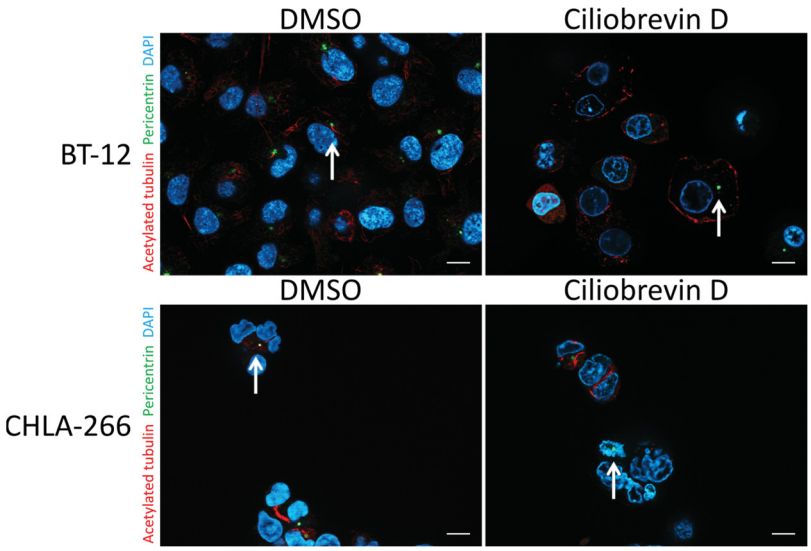

Supplementary figure 3: Ciliobrevin D treatment disrupts primary ciliogenesis in the AT/RT cell lines BT-12 and CHLA-266. BT-12 and CHLA-266 cells were seeded in complete medium. The next day, complete medium was replaced with medium lacking serum and the cells were treated with 30 µM of Ciliobrevin D or dimethylsulfoxide (DMSO) as a negative control. Representative immunofluorescence images showing stainings for Pericentrin (green) and Acetylated tubulin (red), detecting the basal body and the axoneme of the primary cilium, respectively. Nuclei were counterstained with 4´,6-diamidin-2-phenylindol (DAPI, blue). Arrows indicate either primary cilia in the control cells or disrupted primary ciliogenesis in the Ciliobrevin D treated cells. The scale bar corresponds to 10 µm.

Supplementary table 1: Results of the modifier screen in *Drosophila melanogaster*. The results for the 59 cilia-associated genes evaluated in the modifier screen in *Drosophila* are listed in the following table.

***Drosophila* gene**	**CG number**	**RNAi ID**	**Human orthologue**	**Percentage hatched flies (Mean±SD)**
CG5458	CG5458	109403	*RSPH1*	37±3%
CG14367	CG14367	100571	*CFAP36*	37±11%
SAK	CG7186	105102	*PLK4*	35±18%
Oseg1	CG7161	103598	*IFT122*	35±29%
cep290	CG13889	17732	*CEP290*	33±21%
BBS1	CG14825	109623	*BBS1*	29±16%
Dila	CG1625	103788	*CEP131*	29±10%
CG15666	CG15666	110798	*BBS9*	24±23%
CG5780	CG5780	106366	*IFT43*	24±9%
Oseg2	CG13809	107157	*IFT172*	22±9%
orb2	CG43782	107153	*CPEB3*	21±17%
Efhc1.2	CG11048	106676	*EFHC2*	21±9%
Cep89	CG8214	100799	*CEP89*	21±17%
CG30441	CG30441	106811	*IFT20*	21±5%
btv	CG15148	105152	*DYNC2H1*	19%
CG15923	CG15923	37373	*TMEM67*	19%
CG11760	CG11760	11925	*TMEM216*	18%
IFT57	CG8853	51323	*IFT57*	15%

Cby	CG13415	49138	*CBY1*	13%
LRR	CG1399	24826	*CARMIL1*	11%
Dnai2	CG6053	108601	*DNAI2*	10%
OSCP1	CG13178	44816	*OSCP1*	10%
porin	CG6647	101132	*VDAC1*	9%
Kap3	CG11759	45400	*KIFAP3*	8%
rempA	CG11838	103424	*IFT140*	8%
cos	CG1708	108914	*KIF7*	6%
Klp64D	CG10642	45373	*KIF3A*	6%
Oseg4	CG2069	109805	*WDR35*	6%
Oseg6	CG11237	38462	*WDR19*	6%
Oseg5	CG9333	52551	*IFT80*	5%
hmw	CG7669	29201	*CFAP97*	5%
CG3259	CG3259	46163	*TRAF3IP1*	3%
CG10874	CG10874	109456	*CCDC28A*	3%
Zmynd10	CG11253	31473	*ZMYND10*	0%
fu	CG6551	27662	*STK36*	0%
Sas-4	CG10061	106051	*CENPJ*	0%
dnd	CG6560	104311	*ARL3*	0%
CG6971	CG6971	48986	*DNALI1*	0%
CG13999	CG13999	7889	*TMEM138*	0%
CG1126	CG1126	18200	*BBS5*	0%
Arl6	CG7735	43508	*ARL6*	0%
BBS8	CG13691	32058	*TTC8*	0%
CCDC151	CG14127	32914	*CCDC151*	0%
BBS4	CG13232	14195	*BBS4*	0%
CG5964	CG5964	33617	*FBF1*	0%
CG8116	CG8116	104624	*TMEM216*	0%
CG14905	CG14905	39848	*CCDC63*	0%
CG17083	CG17083	39937	*CCDC63*	0%
CG17387	CG17387	32901	*CCDC39*	0%
CG43370	CG43370	25336	*CC2D2B*	0%
Fmr1	CG6203	8933	*FXR1*	0%
HEATR2	CG31320	25742	*DNAAF5*	0%
tilB	CG14620	24883	*LRRC6*	0%
CG4525	CG4525	107708	*TTC26*	0%
CG5142	CG5142	22017	*TTC30A*	0%
CG15161	CG15161	25198	*IFT46*	0%
Cep135	CG17081	14683	*CEP135*	0%
IFT52	CG9595	24068	*IFT52*	0%
nompB	CG12548	31965	*IFT88*	0%

Supplementary table 2: The investigated clinical drug library. The clinical inhibitor library, consisting of 199 compounds, is listed in the following table. All compounds were purchased from MedChemExpress, New Jersey, USA, as a customized library and were provided as 10 mM dimethylsulfoxide (DMSO) stock solutions.

Number	Name	Target/Mechanism
1	3-Deazaneplanocin A (hydrochloride)	EZH2; HMTase
2	5-Azacytidine	Nucleoside antimetabolite/analog
3	5-Fluorouracil	Nucleoside antimetabolite/analog
4	6-Mercaptopurine	Nucleoside antimetabolite/analog
5	6-Thioguanine	Nucleoside antimetabolite/analog
6	ABT-199	Bcl-2 Family
7	Actinomycin D	Antibacterial
8	Afatinib (dimaleate)	EGFR
9	AICAR	AMPK
10	Alisertib	Aurora Kinase
11	Altretamine	DNA alkylator/crosslinker
12	Amonafide	Topoisomerase
13	Anacetrapib	CETP
14	Axitinib	VEGFR
15	AZD-9291	EGFR
16	AZD-9291 (mesylate)	EGFR
17	Bardoxolone (methyl)	Keap1-Nrf2
18	Baricitinib (phosphate)	JAK
19	BAY 80-6946	PI3K
20	Belinostat	HDAC
21	Bendamustine (hydrochloride)	Others
22	Betahistine (dihydrochloride)	Histamine Receptor
23	Bexarotene	RAR/RXR
24	BIBF 1120	FGFR; PDGFR; VEGFR
25	Bleomycin (sulfate)	Others
26	BML-286	PDZ domain of dishevelled
27	BMN-673 (8R,9S)	PARP
28	Bortezomib	Proteasome
29	Bosutinib	Bcr-Abl; Src
30	Brivanib	VEGFR
31	BSI-201	PARP
32	Busulfan	DNA alkylator/crosslinker
33	Cabazitaxel	Microtubule/Tubulin
34	Cabozantinib (S-malate)	VEGFR
35	CAL-101	PI3K
36	Canertinib	EGFR
37	Capecitabine	Nucleoside antimetabolite/analog
38	Carboplatin	DNA alkylator/crosslinker
39	Carfilzomib	Proteasome
40	Carmustine	DNA alkylator/crosslinker
41	Cediranib	VEGFR
42	CEP-32496	Raf

43	Chlorambucil	Others
44	Chlormethine (hydrochloride)	Others
45	CI-994	HDAC
46	Cisplatin	DNA alkylator/crosslinker
47	Cladribine	Adenosine Deaminase
48	Clofarabine	Nucleoside antimetabolite/analog
49	Cobimetinib	MEK
50	Crizotinib	ALK; c-Met/HGFR
51	Cyclophosphamide	DNA alkylator/crosslinker
52	CYT387	JAK
53	Cytarabine	Nucleoside antimetabolite/analog
54	Dabrafenib (Mesylate)	Raf
55	Dacarbazine	Nucleoside antimetabolite/analog
56	Dapagliflozin	SGLT
57	Dasatinib	Bcr-Abl; Src
58	Daunorubicin (Hydrochloride)	ADCs cytotoxin; Topoisomerase
59	Decitabine	DNMT
60	Deforolimus	mTOR
61	Dinaciclib	CDK
62	Docetaxel	Microtubule/Tubulin
63	Dovitinib	c-Kit
64	Doxorubicin (hydrochloride)	ADCs cytotoxin; Topoisomerase
65	Elesclomol	Apoptosis inducer
66	Empagliflozin	SGLT
67	Entinostat	HDAC
68	Enzastaurin	PKC
69	Epirubicin (hydrochloride)	Topoisomerase
70	EPZ-6438	EZH2; HMTase
71	Erlotinib	EGFR
72	Estramustine (phosphate sodium)	Microtubule/Tubulin
73	Etoposide	Topoisomerase
74	Everolimus	mTOR
75	FG-4592	HIF
76	Floxuridine	Nucleoside antimetabolite/analog
77	Fludarabine (phosphate)	Nucleoside antimetabolite/analog
78	Fosbretabulin (disodium)	Microtubule/Tubulin
79	Ganetespib	HSP
80	GANT 61	GLI1
81	GDC-0994	ERK
82	Gefitinib	EGFR
83	Gemcitabine	Nucleoside antimetabolite/analog
84	GSK 525762A	BET bromodomain
85	GSK126	EZH2; HMTase
86	GSK343	EZH2; HMTase
87	Homoharringtonine	Others
88	Honokiol	Apoptosis inducer
89	Hydroxyurea	DNA/RNA Synthesis

90	Idarubicin (hydrochloride)	Topoisomerase
91	Ifosfamide	DNA alkylator/crosslinker
92	Imatinib (Mesylate)	c-Kit; PDGFR
93	INK 128 (MLN0128)	mTORC1/2
94	IPI-145	PI3K
95	Irinotecan	Topoisomerase
96	Isotretinoin	RAR/RXR
97	Itraconazole	Antifungal
98	Ixabepilone	Microtubule/Tubulin
99	Lapatinib	EGFR
100	LDE225	Smo
101	LDK378	ALK
102	LEE011	CDK
103	Lenvatinib	VEGFR
104	LGK974	PORCN
105	LGX818	Raf
106	Linifanib	PDGFR; VEGFR
107	Linsitinib	IGF-1R; Insulin Receptor
108	Lomustine	DNA alkylator/crosslinker
109	Lonafarnib	Farnesyl Transferase
110	Losmapimod	p38 MAPK
111	LY2835219	CDK
112	LY3009120	Raf
113	Marimastat	MMP
114	Masitinib	c-Kit; PDGFR
115	MEK162	MEK
116	Melphalan	DNA alkylator/crosslinker
117	Methotrexate	ADCs cytotoxin; Antifolate
118	Mitomycin C	ADCs cytotoxin; DNA alkylator/crosslinker
119	Mitoxantrone (dihydrochloride)	Topoisomerase
120	MLN9708	Proteasome
121	Motesanib (Diphosphate)	c-Kit; VEGFR
122	MRK003	γ-secretase
123	Nelarabine	Nucleoside antimetabolite/analog
124	Neratinib	EGFR
125	Nilotinib	Bcr-Abl
126	Obatoclax	Bcl-2 Family
127	Olaparib	PARP
128	OTX-015	BET bromodomain
129	Oxaliplatin	DNA alkylator/crosslinker
130	Paclitaxel	ADCs cytotoxin; Microtubule/Tubulin
131	Pacritinib	FLT3; JAK
132	Palbociclib	CDK
133	Panobinostat	HDAC
134	Pazopanib (Hydrochloride)	PDGFR; VEGFR
135	PCI-32765	Btk

136	Pemetrexed (disodium hemipenta hydrate) (1:2:2.5)	Antifolate
137	Pentostatin	Adenosine Deaminase
138	Perifosine	Akt
139	Pexidartinib	c-Fms; c-Kit
140	PF-04691502	mTOR; PI3K
141	Pipobroman	Others
142	Ponatinib	Bcr-Abl; FGFR; FLT3; VEGFR
143	Pralatrexate	Antifolate
144	Procarbazine (Hydrochloride)	DNA alkylator/crosslinker
145	Quizartinib	FLT3
146	R788 (disodium hexahydrate)	Syk
147	Rapamycin	mTOR
148	Regorafenib	VEGFR
149	Retinoic acid	Others
150	Rigosertib (sodium)	Polo-like Kinase (PLK)
151	Romidepsin	HDAC
152	Rucaparib (phosphate)	PARP
153	Ruxolitinib (phosphate)	JAK
154	Ruxolitinib (S enantiomer)	JAK
155	Selumetinib	MEK
156	Semagacestat	γ-secretase
157	Sorafenib (Tosylate)	Raf
158	Staurosporine	PKC
159	Streptozocin	DNA alkylator/crosslinker
160	SU5416	VEGFR
161	Sunitinib (malate)	PDGFR; VEGFR
162	TAK-632	Raf
163	TAK-715	p38 MAPK
164	Tariquidar	P-glycoprotein
165	Tasquinimod	HDAC
166	Temozolomide	DNA alkylator/crosslinker
167	Temsirolimus	mTOR
168	Teniposide	Topoisomerase
169	Thioridazine (hydrochloride)	5-HT Receptor; Dopamine Receptor
170	Thio-TEPA	DNA alkylator/crosslinker
171	Tipifarnib	Farnesyl Transferase
172	Tipiracil (hydrochloride)	Nucleoside antimetabolite/analog
173	Tivantinib	c-Met/HGFR
174	Tivozanib	VEGFR
175	Tofacitinib (citrate)	JAK
176	Topotecan (Hydrochloride)	Topoisomerase
177	Trametinib	MEK
178	Trifluorothymidine	Nucleoside antimetabolite/analog
179	TSU-68	PDGFR
180	Tubastatin A (Hydrochloride)	HDAC
181	Uramustine	DNA alkylator/crosslinker

182	Valproic acid (sodium salt)	HDAC
183	Valrubicin	Others
184	Vandetanib	VEGFR
185	Vatalanib	VEGFR
186	Veliparib (dihydrochloride)	PARP
187	Vemurafenib	Raf
188	Verteporfin	YAP
189	Vinblastine (sulfate)	Microtubule/Tubulin
190	Vincristine (sulfate)	Microtubule/Tubulin
191	Vinflunine (Tartrate)	Microtubule/Tubulin
192	Vismodegib	Hedgehog
193	Volasertib	Polo-like Kinase (PLK)
194	Vorinostat	HDAC
195	VRT752271	ERK
196	WP1066	JAK; STAT
197	Zibotentan	Endothelin Receptor
198	Zoledronic acid (monohydrate)	PKC
199	Zosuquidar (trihydrochloride)	P-glycoprotein

8.3 Figure directory

8.4 Table directory

9 Acknowledgement

First of all, I would like to thank my supervisor Prof. Dr. Guido Reifenberger for giving me the opportunity to work on this interesting PhD project and for proofreading this thesis. I greatly appreciate your continuous support throughout the years. I also would like to thank Prof. Dr. Thomas Kurz for evaluating my thesis as a second supervisor.

I would like to thank Prof. Dr. Arndt Borkhardt and Dr. Ute Fischer for their constant scientific support and for fruitful discussions.

I would like to thank Dr. Marc Remke for his mentorship. Thank you, Marc, for your unlimited support throughout the years and for giving me the opportunity to attend conferences and meet scientists all over the world. I really appreciate your passion and dedication to science, and I am looking forward to further work with you together in the future.

I would like to thank the Düsseldorf School of Oncology for financial support.

I would like to thank Prof. Dr. Martin Hasselblatt and Cláudia Faria (MD, PhD) for successful collaborations. Especially, I would like to thank Cláudia, Rita, Eunice and Carlos for the three great months I spend with you in Lisbon. Thank you so much for teaching me all important skills on mouse experiments and on Portuguese traditions and habits.

I would like to thank all current and former members of the KMT lab for the friendly working environment.

I would like to thank all current and former members of the Remke lab for the amazing time spend together inside and outside the lab, and for being not only colleagues but friends. Anna, thank you so much for setting up such a great working place and for being an invaluable companion from day one. A special thanks goes to Nan and Daniel for their continuous support in planning experiments and analyzing data. Big thanks to Vicky, David and Ulvi for the countless laughs in our shared office and for the strong company throughout the years. Frauke, special thanks to you as well for your invaluable support in the lab and for always having an open ear - at any time and for any situation in life. Especially, I would like to express my deepest gratitude to Jasmin. Thank you so much,

Jasmin, for always taking care, for supporting me in every situation, for being a mentor for me as well, and for proofreading this thesis.

Finally, I would like to thank the most important people in my life - my dear family and friends. Thank you from the bottom of my heart for always being there, for always believing in me and supporting me, and for your unconditional love.

In memory of my beloved mother - you are the reason why!

Curriculum vitae

Personal data

Name:	Lena Blümel
Date and place of birth:	June 21, 1989 in Greven

Work experience

Since 05/2015	Research associate University Hospital, Düsseldorf; Department of Pediatric Oncology, Hematology and Clinical Immunology; DKTK Junior Research Group Pediatric Neuro-Oncogenomics
11/2019 - 01/2020	Visiting research associate Faculdade de Medicina da Universidade de Lisboa (Portugal); Instituto de Medicina Molecular João Lobo Antunes
11/2014 - 03/2015	Student assistant University Hospital, Münster; Department of Gynecology and Obstetrics; Breast Center

Studies

Since 05/2015	PhD student University Hospital, Düsseldorf; Department of Pediatric Oncology, Hematology and Clinical Immunology; DKTK Junior Research Group Pediatric Neuro-Oncogenomics Research project: Targeting primary ciliogenesis in atypical teratoid/rhabdoid tumors.
09/2014	Master of Science
08/2013 - 08/2014	Master´s research University Hospital, Münster; Department of Gynecology and Obstetrics; Translational Tumor Biology Group

	Master thesis: Molecular reprogramming of triple negative mammary carcinoma cells as basis for new, target-directed therapeutic strategies.
04/2012 - 09/2014	Master studies - Biosciences/Life Sciences - at the Westfälische Wilhelms-University Münster
09/2011	Bachelor of Science
04/2011 - 08/2011	Bachelor´s research
	University Osnabrück; Biological/Chemical Faculty; Animal Physiology Group
	Bachelor thesis: Analysis of ABC transporters in the baker's yeast *Saccharomyces cerevisiae*.
10/2008 - 09/2011	Bachelor studies - Cell Biology - at the University Osnabrück

Education

06/2008	Abitur
1999 - 2008	Gymnasium, Borghorst

Internships

03/2013 - 05/2013	Max Planck Institute for Molecular Biomedicine, Münster; Department of Cell and Developmental Biology; Planarian Stem Cell Laboratory
06/2012 - 08/2012	Center for Molecular Biology of Inflammation, Münster; Institute of Medical Biochemistry; Cell Biology of Signal Regulation Group
10/2011 - 03/2012	University Hospital, Münster; Department of Gynecology and Obstetrics; Translational Tumor Biology Group

Oral presentations

3rd Essen Translational Oncology Symposium (ETOS), 2020 Feb 6, Essen, GER

5th Pediatric Neuro-Oncology Basic & Translational Research Conference (SNOPEDS), 2019 May 3-4, San Francisco, USA

5th Retreat of the Düsseldorf School of Oncology, 2017 Apr 6, Düsseldorf, GER

52nd Workshop for Pediatric Research, 2016 Oct 27-28, Frankfurt, GER

Poster presentations

18th International Symposium on Pediatric Neuro-Oncology (ISPNO), 2018 Jun 30 - Jul 3, Denver, USA

48th Congress of the International Society of Paediatric Oncology (SIOP), 2016 Oct 19-22, Dublin, IRL

6th Conference on Molecular Basics and Therapeutic Implications in Breast Cancer (COMBATing Breast Cancer), 2013 Nov 15-16, Lübeck, GER

Awards, Scholarships and Travel Grants

02/2020	Award for the best talk at the 3rd Essen Translational Oncology Symposium (ETOS)
11/2019 - 01/2020	Travel Grant for a research stay abroad, Heine Research Academies
05/2019	Travel Grant, Heine Research Academies
07/2018	Travel Grant, Kind-Philipp-Stiftung
04/2017	Award for the best talk at the 5th Retreat of the Düsseldorf School of Oncology
05/2015 - 07/2018	PhD Scholarship, Düsseldorf School of Oncology
11/2013	Travel Grant, COMBATing Breast Cancer

Publications

Multiple DNA damage-dependent and DNA damage-independent stress responses define the outcome of ATR/Chk1 targeting in medulloblastoma cells.
Krüger K, Geist K, Stuhldreier F, Schumacher L, **Blümel L**, Remke M, Wesselborg S, Stork B, Klöcker N, Bormann S, Roos WP, Honnen S, Fritz G.
Cancer Lett. 2018 Aug 28;430:34-46. doi: 10.1016/j.canlet.2018.05.011.
PMID: 29753759

Reverse engineering of triple-negative breast cancer cells for targeted treatment.
Bluemel L, von Wahlde MK, Tio J, Kiesel L, Bernemann C.
Maturitas. 2018 Feb;108:24-30. doi: 10.1016/j.maturitas.2017.11.010.
PMID: 29290211

Influence of secreted frizzled receptor protein 1 (SFRP1) on neoadjuvant chemotherapy in triple negative breast cancer does not rely on WNT signaling.
Bernemann C, Hülsewig C, Ruckert C, Schäfer S, **Blümel L**, Hempel G, Götte M, Greve B, Barth PJ, Kiesel L, Liedtke C.
Mol Cancer. 2014 Jul 17;13:174. doi: 10.1186/1476-4598-13-174.
PMID: 25033833

Düsseldorf, May 2020

Affirmation

Hereby, I declare on oath that I composed this dissertation independently by myself. I used only the references and resources indicated in this thesis. With the exception of such quotations, the work presented in this thesis is my own. I have accredited all the sources of help. This PhD thesis was never submitted or presented in a similar form to any other institution or examination board. I have not undertaken a doctoral examination without success so far.

Düsseldorf, May 2020

_____

Lena Blümel